MAGNETIC RECONNECTION AS A CHONDRULE HEATING MECHANISM
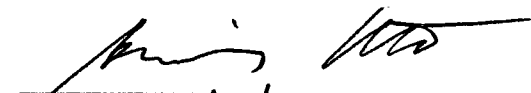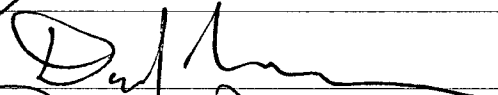
By

Samuel Lazerson

RECOMMENDED:
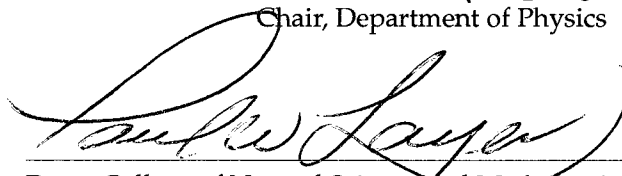
HEINZ WIECHEN

Advisory Committee Chair (deceased)

Chair, Department of Physics
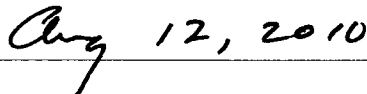
APPROVED:

Dean, College of Natural Science and Mathematics

Dean of the Graduate School

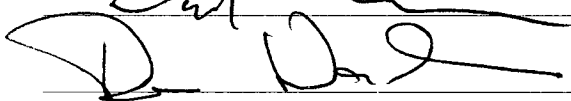Aug 12, 2010

Date

MAGNETIC RECONNECTION AS A CHONDRULE HEATING MECHANISM

A

THESIS

Presented to the Faculty

of the University of Alaska Fairbanks

in Partial Fulfillment of the Requirements

for the Degree of

DOCTOR OF PHILOSOPHY

By

Samuel A. Lazerson, B.S.

Fairbanks, Alaska

August 2010

UMI Number: 3436656

UMI®

Dissertation Publishing

ProQuest®

Abstract

The origin of chondrules (sub-millimeter inclusions found in stony meteorites) remains today an open question despite over century of examination. The age of these proto-solar relics shows a well defined cutoff of around 4.5 billion years ago. This places them as the oldest solids in the solar system. Chemical examination indicates that they experienced heating events on the order of 5000 K/hr for periods of around 30 minutes, followed by extending periods of cooling. Additional examination indicates the presence of large magnetic fields during their formation. Most attempts to explain chondrule formation in the proto-solar nebula neglect the existence of a plasma environment, with even less mention of dust being a charge carrier (dusty plasma). Simulations of magnetic reconnection in a dusty plasma are forwarded as a mechanism for chondrule formation in the proto-solar nebula. Here large dust-neutral relative velocities are found in the reconnection region. These flows are associated with the dynamics of reconnection. The high Knudsen number of the dust particles allows for a direct calculation of frictional heating due to collisions with neutrals (allowing for the neglect of boundary layer formation around the particle). Test particle simulations produce heating equivalent to that recorded in the chondrule mineral record. It is shown that magnetic reconnection in a dusty plasma is of fundamental importance to the formation of the most primitive solids in the solar system.

Table of Contents

List of Figures

List of Tables

List of Appendices

Acknowledgements

I'd like to thank the following people: Dr. Jack Lazerson for introducing me to science at an early age, Dr. Roger Smith for funding me throughout this endeavour, and Dr. Heinz Wiechen for introducing me to dusty plasmas and guiding this work. This work is dedicated to the memory of Dr. Heinz M. Wiechen (June 5, 1958 – November 23, 2008).

"To trace the origin of the solar system is archaeology, not physics."
—Hannes Alfven

"Denny Crane!"
—William Shatner

Chapter 1

Introduction

The story of how chondrites (a special group of meteorites) came to be is recorded in the rocks themselves (Sears, 2004). Each chondrite contains information regarding age (Fireman et al., 1970), thermal processing (H. C. Connolly and Love, 1998), and the environment in which they formed (Taylor et al., 1983). To date many theories attempt to reconcile these facts into a description of how the rocks came to posses their properties (Boss, 1996). There does not exist a single theory which clearly explains all the properties of chondrites. It is clear that they formed in the environment of the protosolar nebula (Taylor et al., 1983). This environment opens up the possibility of plasma processes being responsible for properties we measure today in chondrites. Promising work has already been conducted into the possibility of current sheets and disk instabilities resulting in an explanation of chondrite formation where the presence of a plasma state is necessary (Levy and Araki, 1989; Cameron, 1995; Joung et al., 2004). These works have to date neglected the charged dust that must have been present in the protosolar nebula (Mendis and Rosenberg, 1994). I seek to conduct the first simulations of magnetic reconnection in a dusty plasma. These simulations will allow the assessment of effects of magnetic reconnection on the dust, in terms of dust particle heating. Emphasis will be placed on magnetic reconnection as a heating mechanism for dust particles in the protosolar nebula.

1.1 Motivation

The conditions under which chondrites formed has been extrapolated from their chemical composition, age, magnetic history, and mineral structure (Sears, 2004). The heating and cooling rates of chondrites can be inferred from the presence of specific minerals and volatile elements (Sears and Dodd, 1988; Hewins and Radomsky, 1990). Varied chemical composition allows classification of chondrites among minerals of similar thermal parameters (Sears, 2004). Radioactive dating shows a defined cutoff in age, around the time of planetary formation (Fireman et al., 1970; Sears, 2004). This places their formation occurring before that of the planets. Magnetic histories indicates that chondrites formed in fields larger than those of Earth (Butler, 1972; Levy and Sonnet, 1978; Suguira et al., 1979). The mineral structure (Figure 1.1) of chondrites shows many important features. The presence
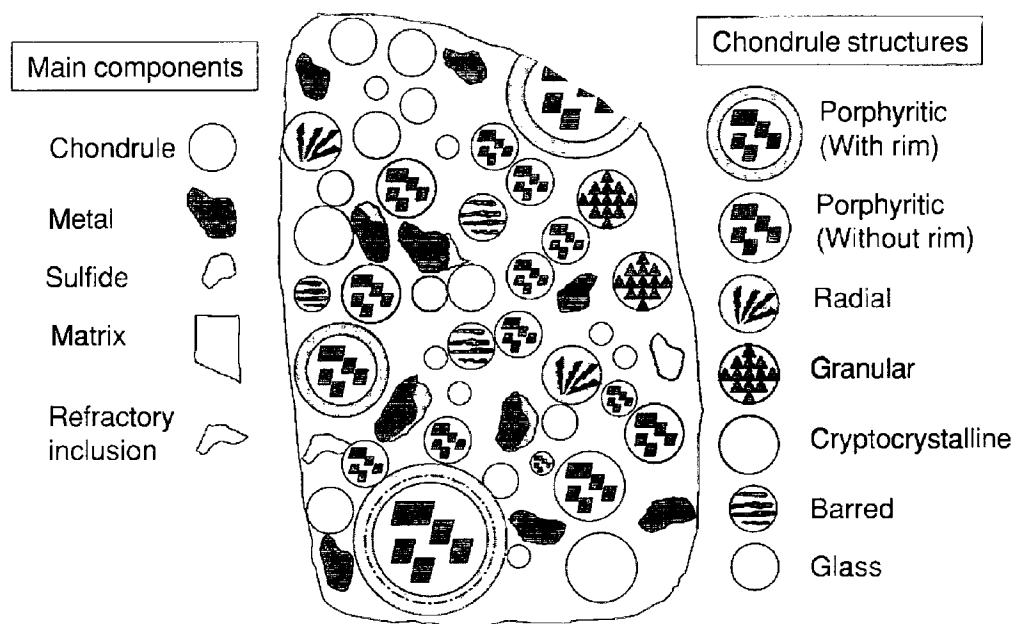
Figure 1.1. Cartoon showing the variety of components in a typical primitive (low-petrographic type) ordinary chondrite. The components are chondrules, metal, sulfide, matrix, and refractory inclusions. The dimensions of this hypothetical section would be about 1cm x 2cm. (Sears, 2004)

of ringed chondrules (smaller precursor grains found in chondrites) reveals that they went through multiple heating and cooling events (Rubin, 1984; Wasson, 1993). These features present us with information about the environment in which chondrites formed and the processes by which they came to be.

Chondrites are categorized by their composition, chondrule size, and metal content (Sears, 2004). A multitude of classification systems have been developed to this end (Merrill, 1920; Wood, 1962; von Tschermak, 1964; Kieffer, 1975; Dodd, 1981; Gooding and Keil, 1981; King, 1983; Scott and Taylor, 1983; Jones and Scott, 1989; Sears et al., 1992). A sample from Sears (Sears, 2004) shows the current classifications of chondrites (Table 1.1). The presence of volatile elements, such as S and Na, place constraints on the temperature regimes to which chondrites were exposed (Hewins and Radomsky, 1990; Wasson, 1993). The presence of such volatiles indicates that chondrites experience average temperatures

below 650 [K] (Desch and H. C. Connolly, 2002). This fact excludes chondrule formation close to the protostar or far from the accretion disk (Boss, 1996). Information regarding the heating of chondrules can be inferred from composition. Presence of porphyritic olivine and barred olivine structures indicates heating to temperatures 80-400 [K] above the liquidus temperature (Hewins and Radomsky, 1990; Hewins et al., 1996). This places peak temperatures to be around 1770-2120 [K] (Desch and H. C. Connolly, 2002). Chondrules require rapid cooling rates ($5000[K/hr]$) above liquidus temperatures, and slower rates (5—3000 [K/hr]) between liquidus and solidus (Desch and H. C. Connolly, 2002). This is an important constraint regarding possible cooling mechanisms (radiative heat transfer to deep space would provide too quick a cooling to be considered). Chondrite composition reveals much regarding the environment in which they formed.

The presence of a remnant magnetization is characteristic of the electromagnetic environment in which chondrites formed (Levy and Sonnet, 1978). Paleomagnetic evidence indicates that two heating processes occurred (Suguira et al., 1979). The first was a high temperature melt in which chondrules were formed. The second was a lower temperature accretion process by which the chondrite was formed. The average magnetic induction of the Allende meteorite shows magnetic fields ranging from 10^{-7}–10^{-4} [T] (Butler, 1972). This provides a picture of the magnetic environment in which they formed.

Radionuclide dating by Ar-Ar (Turner, 1981), Rb-Sr (Minster and Allegre, 1979), and U-Pb (Unruh and Tatsumoto, 1980) indicates that chondrites formed during planetary formation (at times earlier than 4.5 billions years ago). Chondrites are composed of primarily of chondrules, thus the chondrules must have formed earlier than the chondrite cutoff age (Taylor et al., 1983). Chondrules are considered to be the first solids in the solar system and the intermediary between submicron dust and meter sized objects (Joung et al., 2004). The St. Severin meteorite yielded an age of around 4.552 [Ga] (1 [Ga] = $1x10^9$ [years]). Dating of the Allende meteorite shows chondrule ages around 4.44 [Ga] (Fireman et al., 1970). This is in agreement with the estimated age of the Earth (Sears, 2004). Additional work seems to indicate that chondrules formed before the Earth had finished the majority of planetary accretion (Allegre et al., 1995). From this data it is reasonable to conclude that the chondrules were processed in the protosolar nebula (Taylor et al., 1983). Radionuclide dating provides solid evidence that chondrules and chondrites were formed before the planets

Table 1.1. The chondrite classes, particle sizes, metal abundances, and certain compositional properties. Small classes like the primitive achondrites and many anomalous chondrites are not considered here (Sears, 2004).

	EH	EL	H	L	LL	R	CK	CV	CO	CH	CR
Physical properties											
Chondrule diam.	0.2–0.6	0.8	0.3	0.7	0.9	0.4	0.7	1	0.2–0.3	∼0.1	0.8
Metal grain size	–	–	0.2	0.18	0.14	–	–	–	–	6	–
Chondrule abund.	20–40	20–40	65–75	65–75	65–75	≥ 40	15	35–45	35–40	∼70	52
Metal abund.	22	18	16	6	2	0.1	0.01	0-7	0-5	20	6.3
Matrix abund.	5	5	10–15	10–15	10–15	35	75	40–50	30–40	5	44
Composition properties											
Carbon	0.42	0.32	0.11	0.12	0.22	–	0.1	0.43	0.38	–	1.97
Water	1.9	1.6	0.22	0.46	0.71	–	1.6	0.25	3.3	–	7.11
Fe_m/Fe_t	0.76	0.83	0.58	0.29	0.11	∼0	∼0	0–0.3	0–0.2	0.95	0.22
Fe/Si	0.95	0.62	0.81	0.57	0.52	–	0.83	0.76	0.77	2.2	0.81
Mg/Si	0.77	0.83	0.96	0.93	0.94	–	1.13	1.07	1.05	1.02	1.06
Ca/Si	0.035	0.038	0.05	0.046	0.049	–	0.068	0.084	0.067	0.017	0.06
$\delta^{17}O$	3	2.7	2.9	3.5	3.9	5.27	-5	∼-4.0	∼-5.1	∼-1.3	∼-0.7
$\delta^{18}O$	5.6	5.3	4.1	4.6	4.9	4.74	-1	∼0	∼-1.1	∼0	∼2

Units: chondrule diameter and metal grain size, mm; chondrule and matrix abundance, vol. %; metal, carbon, and water abundance, wt %; Fe_m/Fe_t, Fe/Si, Mg/Si, and Ca/Si, atom ratio; $\delta^{17}O$ and $\delta^{18}O$, per mil.

had finished forming.

The structure of the chondrites display a variety of features (Sears, 2004). The general structure of a chondrite is often termed "matrix" as it contains a multitude of chondrules, metals, sulfides, and refractory inclusions (Sears, 2004). Sears provides a cartoon to illustrate the multitude of characteristics seen in a typical chondrite.(Figure 1.1) The Allende meteorite presents a cross-section through a chondrite. (Figure 1.2) The multiply rimmed structures provide an important record of the heating events. These structures can only be formed if a chondrule was to experience similar thermal processing events multiple times (Rubin, 1984). A single thermal event could not produce these rimmed structures, nor account for the array of mineral compositions found in chondrites. These features record the life of a chondrite.

Chondrules provide us with a mineral record of our solar system. Their chemical composition (and the composition of the chondrite in which they are found) places constraints on the temperatures they experience (650 [K] ambient; 1770-2120 [K] peak) (Hewins and Radomsky, 1990). This gives us insight into the processes responsible for their existence (Boss, 1996). Radioactive dating of chondrites indicates they had formed before the planets had finished forming (some 4.5 billion years ago) (Taylor et al., 1983). They have recorded the protosolar nebula in their structure. Remnant magnetization found in chondrites is an indicator of a magnetically active nebula (Levy and Sonnet, 1978). The presence of varied compositions and rimmed structures in chondrites is evidence of this activity (Rubin, 1984). These rocks provide us with a detailed history of their evolution and what processes were at play in the protosolar nebula. Simulations of the dusty plasma processes in the protosolar nebula are needed in order to asses their role in chondrule formation.
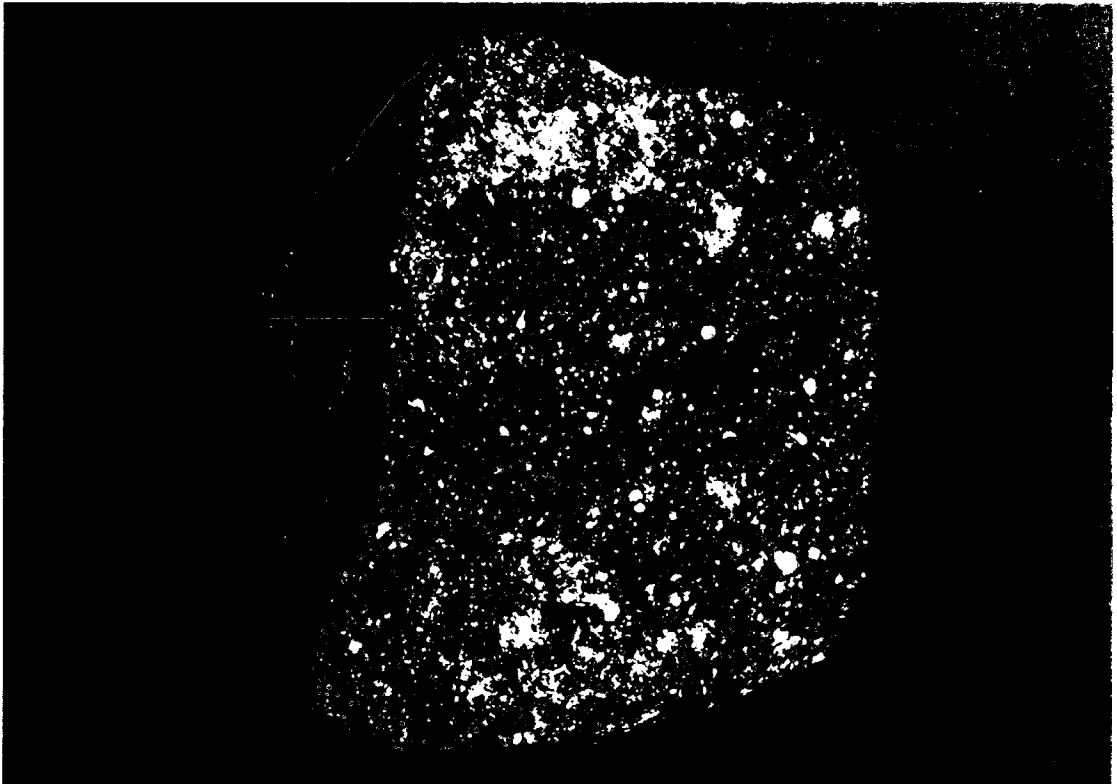
Figure 1.2. Photograph of a cross-section of the allende meteorite. This meteorite was found in Allende, Mexico. Image courtesy of D. Ball, ASU.

1.2 Previous Theories of Chondrule Formation

Many theories have been forwarded in the 20th century to explain the properties of chondrites (Wasson, 1993; Boss, 1996; Sears, 2004). These theories can be grouped by their requirement of a plasma treatment. Of those not requiring plasma dynamics include meteor ablation (Brownlee et al., 1983), hot inner nebula (Cameron and Fegley, 1982; Morfill, 1983; Boss, 1988), FU Orionis outbursts (Hartman and Kenyon, 1985) and accretion shocks (Wood, 1984). Those requiring a plasma treatment include bipolar outflows (Skinner, 1990; Liffman, 1992), nebular lightening (Horányi et al., 1995; Eisenhour, 1994; Eisenhour and Buseck, 1995), magnetic flares (Cameron, 1995), and nebular plasma shocks (Hood and Horányi, 1991, 1993; Desch and H. C. Connolly, 2002; Joung et al., 2004). Additional attempts have been made to explain the thermal properties of chondrites via a collision mechanism (Urey, 1956; Kieffer, 1975). These theories often fail to explain the magnetic properties of the chondrites (Boss, 1996). Additionally, it is unlikely that any large bodies existed in the protosolar nebula (Boss, 1996). Reviews of the theories have been conducted by Levy and Sonett (Levy and Sonnet, 1978); and Boss (Boss, 1996). I shall outline a few of the many theories and discuss their applicability and limitations.

It has been theorized that a meteor in the protosolar nebula could break appart and through aerodynamic heating form chondrules (Brownlee et al., 1983). The basic idea involves a large object moving through the nebula with smaller particles breaking off. These smaller particles would then aerodynamically heat as they came into equilibrium with the surrounding neutral gas. This is in analogy to asteroids breaking up in a planets atmosphere. The main difficulty arises with the high velocity the parent body must have with respect to the nebula. Liffman found the velocity to be around 25 [km/s] (Liffman, 1992). This would only be possible if the parent object had a highly eccentric orbit (Boss, 1996). Meteor ablation as a source for chondrules has been all but ruled out as a possible mechanism.

The nebula itself may have been hot enough to explain heating of the chondrules (Boss, 1988; Cassen, 1994; Boss, 1998). The protosolar nebula must contain the precursor to a star at its core. The outer regions of the disk are cold due to radiative heat transfer and very little compression of the original nebular material. It has been shown through modeling that a hot inner nebula region does not alone account for the peak temperatures required

for chondrule formation (Boss, 1988). Turbulence in the nebula has been shown to cause heating in small inner regions ($1500[K]$) (Morfill, 1983). So it may be possible for dust particles to enter and leave these regions allowing for proper heating and cooling rates. More damning is the presence of volatiles which require ambient temperatures below 650 [K] (Wasson, 1993). A globally hot nebular region would prevent these inclusions (Cameron and Fegley, 1982). While the inner region of the nebula was clearly hot, it's unlikely that chondrite and chondrule formation occurred there as temperatures were too hot, thus ruling it out as a chondrule formation mechanism.

FU Orionis outburst have been detected in many young stars. These outbusts are seen as decade to century long elevations in luminosity of a star (Hartman and Kenyon, 1985). Objects are classified as FU Orionis objects if such increases in luminosity occur. It has been shown that mass accretion from the protostellar disk onto the protostar is responsible for these elevations in luminosity (Hartman and Kenyon, 1985; Herbig, 1977; Larson, 1983; Bell and Lin, 1994). Accretion rates onto the central star are on the order of that required to heat the inner nebula. Difficulties arise when considering the timescales. The timescales for these events pose a significant restriction (Boss, 1996). Also, spectral evidence indicates these objects have disk surface temperatures up to 10,000 [K] which would not fit the maximum temperature constraint imposed by the chondrites (Bell and Lin, 1995). Hartmann argued that these outbursts result in strong bipolar outflows (Hartman and Kenyon, 1985). These outflows have been suggested as a means of chondrule formation.

Young stars often posses bipolar flows (Lada, 1985). These flows manifest themselves as narrow jets or outflowing lobes directed perpendicular to the accretionary disk (Figure 1.3). It is possible that in these jets stellar matter will be ejected. Skinner argues that this matter may return to the disk as chondrules (Skinner, 1990). This is one of the few physical mechanisms we can directly observe occurring in the protostellar environment (Moriarty-Schieven et al., 1987; Pety et al., 2006). However, the process requires all matter found in the midplane to enter a jet (multiple times even) and return to the midplane. This is an unlikely situation (Safier, 1993). While the temperatures of the jets are high enough to melt chondrites and chondrules, the requirement of cooling is unlikely to be fullfilled (Safier, 1993; Boss, 1996). Bipolar flows prove too violent a mechanism to be responsible for the formation of chondrules and chondrites.
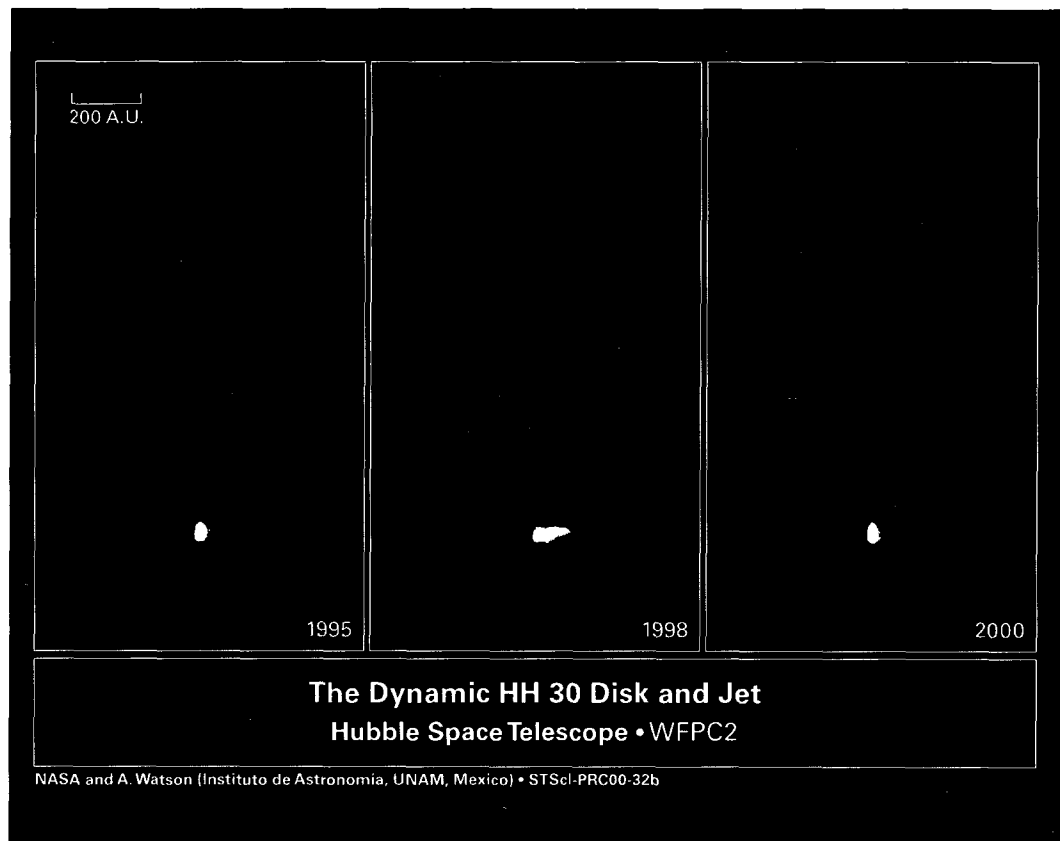
Figure 1.3. This image shows Herbig-Haro 30 (HH 30) and its dynamic Jet. HH30 is considered a prototype of a young star surrounded by a thin, dark disk and powerful gaseous jets. The disk extends 40 billion miles (430 Au) from left to right in the image, dividing the nebula in two. The central star is hidden from direct view by a dense disk. These images were captured by the Hubble Space Telescope's Wide Field Planetary Camera 2 (WFPC2).(NASA and Watson, 1995)

As matter is accreted onto a central object, an accretion shock will form (Calvet and Gullbring, 1998). This shock will heat the neutral gas (and ionize it leading to a plasma state) (Alfvén, 1954). The dust particles in the gas will be slowed by aerodynamic drag leading to heating of dust. Wood shows that in-falling matter had large kinetic energies (20 times that needed to melt a chondrule) (Wood, 1984). However, the overall theory requires dust gas fragmentation. This fragmentation would need to be strong enough to produce a 1000 fold increase dust/gas ratios (above cosmic abundances). Additionally, the multiply rimmed structures seen in chondrites indicate that chondrules experience multiple heating processes. Finally, his model only indicated that the shocks could maintain a 1500 K temperature in the presence of radiative cooling to deep space, not explain the rapid heating and slower cooling. Accretion shock would be a single upset event (Boss, 1996).

It is worthwhile to note at this point that none of these processes requires a plasma (let alone a dusty plasma) description of the nebula to explain chondrite/chondrule formation. Additionally, none of the theories discussed thus far yield a self-consistent explanation of chondrule and chondrite formation. The models are qualitative studies and quantitative estimates. Each mechanism shows improper temperature regimes with the additional complication of requiring all chondrules to form near (or pass by) the protostar. It is argued here that production of chondrules should occur in the accretion disk between 0.1 and 50 [Au], being the domain of the current planets. This would seem a good additional constraint on any theory. Theories that result in heating in the disk region are then required.

Charge separation in the nebula can result in nebular lightening (Whipple, 1966; Morfill et al., 1993). It is well known that micron sized dust particles (and larger) can act as charge reservoirs in space (even at room temperature densities we can inductively charge a sphere and it will maintain charge for a few minutes) (Morfill et al., 1993). Love et al. find that discharges in the nebula would be unlike terrestrial discharges and were an unlikely source of heating (Love et al., 1994). Research into terrestrial lightening is changing our view of the mechanisms for breakdown (Roussel-Dupré et al., 2008). At present, it's unlikely that this mechanism played a large role in chondrite formation.

Magnetic reconnection events at the nebular bow shock have been suggested as a possible heating mechanism. Cameron (Cameron, 1995) proposes this picture where chondrites

are thermally processed by reconnection occurring at the nebular bow shock. This results in fast heating of the chondrules. Unfortunately, the chondrules must be transported to the bow shock where the reconnection is thought to occur. It is unlikely that the magnetic fields were strong enough there to provide the necessary remnant magnetization found in chondrules (Boss, 1996). Levy and Araki (Levy and Araki, 1989), suggest that reconnective flares in the nebular corona would provide the necessary heating. Sonett (Sonnet, 1979) also forwarded a similar idea. Neither treat the problem from the perspective of a dusty plasma or address the large radiative cooling (to deep space) present in the nebular corona.

Nebular shocks have received more recent attention (Hood and Horányi, 1991, 1993; Desch and H. C. Connolly, 2002). Here it is possible that localized shocks in the nebula would be able to produce the array of chondrule properties. Desch and Connolly (Desch and H. C. Connolly, 2002) present a shock model that accurately predicts heating and cooling rates of chondrules in the solar nebula. However, it's difficult to find a source for these shocks.

Each of these mechanisms has been forwarded as a possible theory to explain what is observed in chondrites. Each however, lacks the necessity of processing the bulk of matter in the nebula. Recent developments in plasma theory have resulted in plasma processes being forwarded as a means to heat chondrites through instabilities (formation of current sheets) (Joung et al., 2004; Birk and Wiechen, 2001, 2002). Much work has already been done to explain the turbulence of nebular disks through the magnetorotational instability (MRI, Balbus-Hawley) (Balbus and Hawley, 1991; Hawley and Balbus, 1991). This has opened up the idea that current sheets may have formed in the midplane of the nebula and that reconnection could be occurring there. This would provide an formation environment where the strong effects of radiative cooling could be suppressed. Simulation work to include the dust component in the plasma dynamics of the nebula has only begun to be developed (Schröer et al., 1998; Birk and Wiechen, 2001; Birk et al., 2001; Birk and Wiechen, 2002; Wiechen et al., 2002; Birk et al., 2003; Lazerson and Wiechen, 2008). Simulation of these processes requires a dusty plasma approach.

1.3 Dusty Plasmas

Dusty plasmas are of great importance in Astrophysical and Laboratory plasma environments (Chen, 1995; Shukla et al., 1997; Verheest, 2001; Shukla and Mamun, 2002). They are plasmas in which massive, multiply charged particles are included as a plasma component (Shukla and Mamun, 2002). Dust is clearly present in many astrophysical environments (Zodical light, accretion disks, molecular clouds, etc) (de Angelis, 1992; Verheest, 2001; Shukla and Mamun, 2002). Dust charging processes are of great importance with respect to dusty plasma processes. It is the way in which the dust charges that determines the charge to mass ratio and in essence the departure from a normal plasma (Shukla and Mamun, 2002). A distinction must be made between a dust particle in a plasma and a dusty plasma. Particularly we seek to determine if the dust particles behave collectively. It is through the collective interactions that the charged dust particles behave as a dusty plasma (rather than as isolated particles in a plasma). We find that many low frequency properties may express themselves in a dusty plasma. This includes waves, interactions and nonlinear structures. The framework of dusty plasmas provides us a means to understand the dynamics of dust particles in the protosolar nebula.

Dust particles charge by collection of plasma particles, secondary electron emission, photoemission, and other less relevant processes (Shukla and Mamun, 2002). For an isolated dust grain these processes compete until an equilibrium charge is obtained. The physics of the entire process is similar to that of a Langmuir probe (Chen, 1965). For non-isolated dust grains (Debye length larger than the intergrain spacing) we have the analytic result (Barnes et al., 1992)

$$1 - \frac{e\phi_d}{k_BT} - \left(\frac{m_i}{m_e}\right)^{1/2}\left(1+P\frac{e\phi_d}{k_BT}\right)\exp\left(\frac{e\phi_d}{k_BT}\right) = 0 \tag{1.1}$$

where $P = 4\pi n_d r_d \lambda_{do}^2$ and $\lambda_{do}^2 = k_BT_i/4\pi n_i e^2$. This equation gives us the dust grain surface potential ϕ_d, which in turn gives us the equilibrium charge number for the dust. This result has been confirmed by experiments done in a Q-Machine (Barkan et al., 1994). In the absence of photoionization, the dust particles act as giant electron acceptors. This is due to the lower mass of the electrons when compared to that of the ions. The electrons are the more mobile species. It can then be said that dust grains will charge negatively in the absence of photoionization.

We may only treat charged particles as a plasma if they obey certain constraints; dusty plasmas must also meet these constraints. The first constraint is Debye shielding. In order to treat a collection of charged dust particles as a plasma we must have a significant number of particles within the shielding distance of the plasma (Debye length). The Debye length in a dusty plasma, derives from the same considerations as that in a ion-electron plasma. The departure comes from the modification to Poisson's equation that 3 charged species provide. Thus we find that (Shukla and Mamun, 2002)

$$\lambda_D = \frac{\lambda_{De}\lambda_{Di}}{\sqrt{\lambda_{De}^2 + \lambda_{Di}^2}} \tag{1.2}$$

where $\lambda_{Dk} = \sqrt{k_B T_k / n_k Q_k^2}$ is the Debye length for species k. Here k_B, T_k, n_k, and Q_k are Boltzmann's constant, species temperature, species number density, and species charge number respectively. For negatively charged dust, the ion temperature and number density play the largest role in Debye shielding. Next we wish to verify that our quasineutral system is stable to perturbations. This is achieved if the plasma frequency is the largest frequency, or at least larger than our neutral collision frequency. Again, our modified Poisson's equation results in our new definition of plasma frequency (ω_p) for a dusty plasma (Shukla and Mamun, 2002)

$$\omega_p^2 = \sum_s \frac{4\pi n_{s0} q_s^2}{m_s} = \sum_s \omega_{ps}^2 \tag{1.3}$$

These quantities being defined we now have the tools to determine if a given dust-plasma system can be considered a 'dusty plasma.'

The large mass of the dust particles implies that the frequency regime of the dust borne waves will be lower than that of the ions and electrons. A large amount of analytic work has gone into understanding both nonlinear and linear waves that result from the inclusion of charged dust (Verheest, 2001). This work is further complicated by the dust charge itself. For most work the dust is treated as having an equilibrium charge, but truly the charge number of the dust is due to equilibrium currents. When dust charging effects are taken into account the situation can become much more complicated. The interested reader is invited to examine the books "Introduction to Dusty Plasma Physics" by Shukla and Mamun, and "Waves in Dusty Plasmas" by Verheest.

The dynamics of dust are governed by their massive nature and large charge number.

The charging processes determine the electromagnetic nature of the dust. Additionally, the charge number of the dust can dictate the relevant number densities of the singly charged species. Negatively charged dust particles are an indicator of a depleted electron field. Positively charged dust is an indicator of photoionization and the possibility of a depleted ion field. It is important to note that in order to speak of a dust-plasma system in the framework of plasma physics one must verify that the dust particles behave collectively. It is also required that the fundamental oscillations of the plasma (plasma frequency) are not damped by collisions. If these criterion are met, we may then begin to examine the low frequency dynamics that the dust particle play a role in. A discussion of these requirements in the protosolar nebula are deferred to Section 1.5. In this work, focus will be placed on the massive dust and its dynamics. The massive and multiply charged nature of a dusty plasma provides a new framework by which to understand processes in the space environment.

1.4 Magnetic Reconnection

Magnetic Reconnection is a process by which regions of oppositely directed magnetic field are reconfigured so as to break the magnetic isolation of regions, accelerate particles, and heat the plasma. Various initial states of the magnetic field exist, from which magnetic reconnection may emerge (Biskamp, 2000). This work focuses on a Harris-like current sheet (Harris, 1962). Linear theories involving magnetic reconnection attempt to understand the process in a general sense. The two canonical models are the Sweet-Parker (Parker, 1957; Sweet, 1958a,b; Parker, 1963) and Petscheck model (Petschek, 1964). Much work has been conducted on numerical simulation to understand the nonlinear evolution of magnetic reconnection (Birn and Hesse, 2001; Otto, 2001; Birn et al., 2005). Still few of these simulations examine magnetic reconnection in a dusty plasma (Jovanović et al., 2005; Lazerson and Wiechen, 2008). It is through a dusty plasma treatment that a greater understanding of the role of magnetic reconnection in the protosolar disk will be gained.

The Harris sheet (Harris, 1962) presents a magnetic configuration in which magnetic reconnection may occur. The configuration is achieved through a collisionless kinetic treatment of a plasma (collisional effects are discussed in 2.3.1). The derivation involves assumption of a one dimensional system ($\hat{y}$ being the direction perpendicular to the current sheet and $\hat{z}$ being in the direction of the current) which then solves Vlasov's equation

$$\vec{v}_k \cdot \frac{\partial f_k}{\partial \vec{r}} + \frac{q_k}{m_k} \left(\vec{E} + \frac{1}{c} \vec{v} \times \vec{B} \right) \cdot \frac{\partial f_k}{\partial \vec{v}_k} = 0 \tag{1.4}$$

with a shifted Maxwellian distribution

$$f_k = \left(\frac{m_k}{2\pi k_B T_k} \right)^{3/2} n_k \exp \left[-m_k \frac{\alpha_1^2 + (\alpha_2 - v_k)^2 + \alpha_3^2}{2k_B T_k} \right] \tag{1.5}$$

where $\alpha_1^2 = v_x^2 - \frac{2q_k}{m_k} v_y A_y - \frac{q_k^2}{m_k} A_y^2 + \frac{2q_k}{m_k} \Phi$, $\alpha_2 = v_y + \frac{q_k}{m_k} A_y$, and $\alpha_3 = v_z$. This results in a magnetic field that follows a hyperbolic tangent profile similar to $\vec{B} = B_0 \tanh y/\delta \hat{x}$. This analysis predicts a vanishing number density for the plasma as $y \to \infty$. A constant density is added to the profile predicted by Harris yielding

$$\rho_k (y) = \rho_{0k} + \frac{\rho_{0k}}{\cosh^2 (y/\delta)}, \tag{1.6}$$

where ρ_{0k}, y, and δ are the asymptotic species mass density, coordinate across the current sheet, and scaling factor of the current sheet. The same can be done with the pressure to
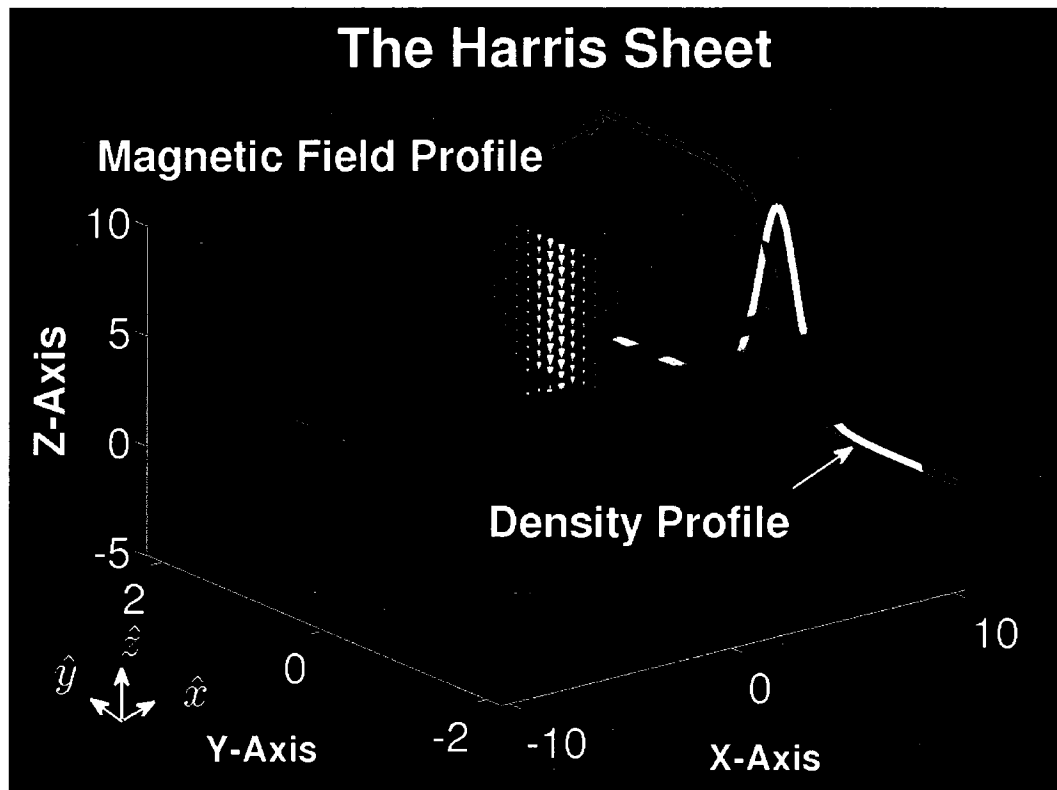
Figure 1.4. A schematic representation of a Harris-like current sheet. The yellow cones depict the direction of the current in the sheet while the profiles of the magnetic field and density are plotted on the side panel. The pressure profile is shown as a semitransparent slice (blue indicates low pressure regions while red indicates high pressures).

yield a constant total pressure ($p_{total} = p_{gas} + p_{mag}$) across the current sheet. Figure 1.4 shows a schematic representation of how this profile looks in three dimensions. There exists a symmetry in B_x along a cut in $\hat{y}$. Magnetic reconnection seeks to break that symmetry through the formation of B_y across the current sheet.

The earliest theory of reconnection, known as the Sweet-Parker model (Parker, 1957; Sweet, 1958a,b; Parker, 1963), calculates a rate at which magnetic energy is extracted through reconnection (known as the reconnection rate). This is achieved by assuming there exist two mirrored regions. The first is an inflow region where plasma advects the oppositely directed magnetic fields towards each other (in a pinching motion). The second is an outflow

region where the reconnected fields are advected away from the region where reconnection is occurring. The inflow region is assumed to support flows equivalent to the diffusive velocity of the system ($v_{inflow} = \eta/l$). Here l is the scale thickness of the reconnection region and η is the global diffusivity of the plasma. The flow is then assumed incompressible so that $Lv_{inflow} = lv_{outflow}$, where L is the scale length of the reconnection region. These equations are coupled with the solenoidal constraint on the magnetic field ($\nabla \cdot \vec{B} = 0$) give the outflow velocity

$$v_{outflow} = \frac{B_{inflow}}{\sqrt{\mu_0 \rho}} = v_{Alfven-inflow}. \tag{1.7}$$

The inflow Mach number provides the reconnection rate

$$M_{inflow} = \frac{v_{inflow}}{v_{Alfven-inflow}}. \tag{1.8}$$

In practice, this provides a reconnection rate much to low of explain the observed rates in many plasmas (Kulsrud, 2001).

Petschek (Petschek, 1964) forwarded a mechanism whereby the anisotropic nature of slow-mode shocks could generate four standing switch-off shocks which would accelerate and heat the plasma. These shocks provide a magnetic field component perpendicular to the current sheet, thus modifying the inflow magnetic field (as compared to the asymptotic magnetic field far from the reconnection region). This field can be written

$$B_{inflow} = B_0 \left(1 - \frac{4M_0}{\pi} \log \frac{L_0}{L} \right). \tag{1.9}$$

Here B_0, M_0, L_0, and L are the asymptotic magnetic field, asymptotic Mach number, asymptotic length scale, and reconnection region length scale. Here it is important to note that the lengthscale over which reconnection takes place (L) is now a smaller subset of the region over which plasma is being advected toward the current sheet (L_0). A maximum reconnection rate (M_0^*) can be estimated through the assumption that the mechanism fails when the inflow magnetic field becomes too small ($B_{inflow} = \frac{1}{2} B_0$), giving

$$M_0^* = \frac{\pi}{8 \log R_{m0}}. \tag{1.10}$$

Where R_{m0} is the asymptotic magnetic Reynolds number. This results in a much larger reconnection rate as compared to the Sweet-Parker theory (Priest and Forbes, 2000).

Much work has gone into simulations of magnetic reconnection in plasmas. Many simulations have been conducted in attempts to understand magnetic reconnection in the space environment. This includes simulations of the dayside magnetopause (Otto, 1991), magnetotail (Scholer and Otto, 1991), and solar atmosphere (Forbes and Priest, 1984). Large campaigns have been conducted to better understand reconnection from a theoretical standpoint. The GEM reconnection challenge (Birn and Hesse, 2001) and Newton ("Taylor") challenge (Birn et al., 2005) to name a few. Despite the large body of work that has been assembled, much debate still exists regarding the particulars of reconnection. The Sweet-Parker and Petschek models are both idealizations with limited applicability to the nonlinear development of magnetic reconnection. This work will examine both these idealized models and more dynamic models of reconnection through a self-consistent nonlinear treatment. The simulations conducted here will be the first self-consistent simulations of three-dimensional magentic reconnection in a dusty plasma.

Magnetic reconnection works to convert magnetic energy into thermal and kinetic energy. This is accomplished through flows toward a current sheet which are then accelerated out of the region where magnetic field energy conversion is occurring. Such features could very well have heated the precursor material in the protosolar nebula. Magnetic reconnection may also be looked on as a process which can destroy current sheets formed by other instabilities. Many instabilities exist in the protosolar nebula which can create current sheets (Rayleigh-Taylor, Kelvin-Helmholtz Balbus-Hawley, etc). Despite the decades of work on magnetic reconnection, a complete understanding of the process does not exist. A self-consistent dusty plasma treatment of non-ideal magnetic reconnection in the protosolar nebula is clearly warranted.

1.5 The Protosolar Nebula

In order to quantize the effects of a dusty plasma model of the protosolar nebula I must parametrize my model nebula. To this end it will be fruitful to examine the general model of solar system formation. I will consider the events from molecular cloud collapse to protoplanetary formation. This will allow a discussion of possible parameter regimes in the protoplanetary nebula. The meteoric record will be referenced. This will be done under the assumption that any anomalous events in the history of the nebula do not have longterm effects on nebular evolution. It will then be useful to examine the implications of a dusty plasma model of the protosolar nebula. This will provide a useful parametrization from which simulations of dusty plasma processes may be evaluated.

The generally accepted description of how the solar system evolved begins with the collapse of a nebular cloud. A cloud of sufficient mass will undergo gravitational collapse, known as the Jean's mass limit (Carroll and Ostlie, 1996). It has been further shown that as a cloud collapses it will not converge to a point as Jean's predicted, but will form regions of enhanced density and pressure (Hunter, 1962). As the cloud collapses it will begin to heat, build up density, and build up pressure in its central region. It was argued that this will result in ionization of gasses (Alfvén, 1954). Any initial angular momentum of the cloud will result in collapse of the cloud into a disk-like structure. At the center of this disk will be a protostar. Matter continues to accrete onto the center star till a point at which the star begins nuclear fusion. At this point the star sends out a solar wind and clears away the gas and smaller particles from the nebula. Only the planets and large objects (asteroids, comets, etc.) will be left around the star. This process is depicted in Figure 1.5. I concern myself the period before planetary formation and during star formation.

The neutral component of the nebula is thought to be mostly composed of monatomic hydrogen ($\sim$ 70%), Helium ($\sim$ 29%), and trace gases (Carroll and Ostlie, 1996). We can assume that in the chondrule forming regions the temperature of the neutral gas is below 500 [K] (Hewins and Radomsky, 1990). This is evident by the presence of refractory inclusions and volatiles in the chondrite. We are fairly free to assume the dust size within the limits of the smallest chondrules (submicron dust is assumed). Our dust charge number is a function of the available charges and the maximum stress that the dust particle can sustain before being ripped appart (Shukla and Mamun, 2002). An equilibrium charge
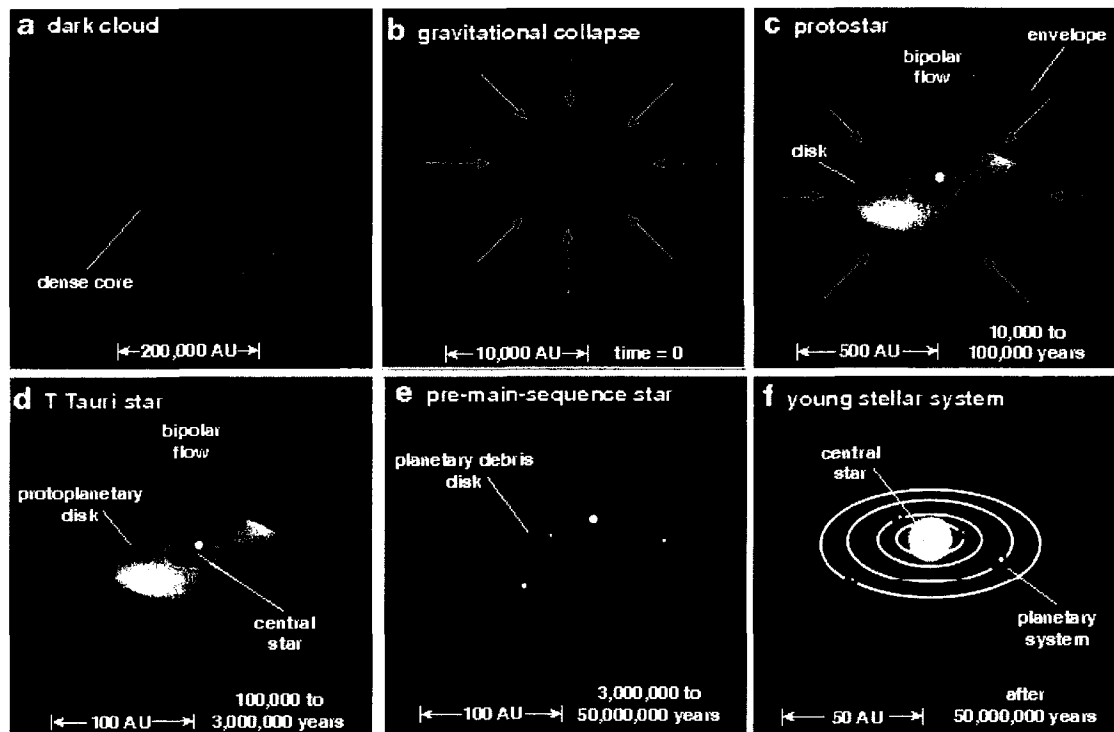
Figure 1.5. Cartoon showing different stages of stellar evolution. Image courtesy of the American Scientist. (Greene, 2001)

number is assumed for the dust. We may safely assume a dust mass of $m_d = 1.69x10^{-16}[kg]$. This assumes that the dust particles are mostly composed of carbon (Sears, 2004). It is also relatively easy to assume that the electron field is heavily depleated. This is a consequence of the high charge number of the dust and the high neutral density (Shukla and Mamun, 2002). These charges are mostly due to ionization of the neutrals (Hydrogen/Helium). This parameterization of the protosolar nebula (Table 1.2) allows a discussion of the plasma properties of such a nebula.

At this point it is worthwhile to discuss the relevant collision frequencies for the proto-solar nebula (values can be found in Table 1.2). The charged-neutral collision frequencies were derived from $\nu_{kn} = n_n\sigma_k^n c_s$ where n_n is the neutral density, σ_k^n is the scattering cross-section for the neutral species, and the speed of sound in the gas species is defined as $c_s = \sqrt{k_B T_k/m_k}$. The ion-electron, ion-dust, and dust-electron collision frequencies are calculated from (Benkadda et al., 1996)

$$\nu_{ie} = \frac{\pi n_e e^4}{m_e^2 \left(\frac{k_B T_e}{m_e}\right)^{3/2}}, \tag{1.11}$$

$$\nu_{id} = \nu_{ch}\left[\frac{2P}{3z(1+\tau+z)\tau(1+P)}\log\frac{\lambda_d}{a}\right], \tag{1.12}$$

and

$$\nu_{de} = \nu_{ch}\frac{\rho_e}{\rho_d}\left[\frac{2P\exp(z)}{3z(1+\tau+z)}(\tau+z)\ln\left(\frac{\lambda_D}{a}\right)\right] \tag{1.13}$$

where

$$\nu_{ch} = \frac{\omega_{pi}^2 a}{v_{Ti}\sqrt{2\pi}}(1+\tau+z) \tag{1.14}$$

$$z = \frac{Z_d e^2}{aT_e} \tag{1.15}$$

$$\tau = \frac{T_i}{T_e} \tag{1.16}$$

$$P = \frac{n_d Z_d}{n_e} \tag{1.17}$$

$$\omega_{pi} = \sqrt{\frac{4\pi n_i e^2}{m_i}}. \tag{1.18}$$

Here v_{ch}, λ_d, ω_{pi}, T_i, T_e, n_d, Z_d, n_i, m_i, n_e, a and v_{Ti} are the charging frequency, Debye length, ion plasma frequency, ion temperature, electron temperature, dust number density, dust charge number, ion number density, electron number density, dust particle radius, and ion thermal velocity respectively. The parameters P, z, and τ are dimensionless parameters.

Examining the dust parameters we see that there are approximately 50,000 dust particles in a Debye sphere. Additionally, we see that even the electron Debye length is much smaller than any scale of interest in the protosolar nebula ($1 \times 10^5 [km]$). One must be careful with the collision frequencies. The dust plasma frequency is on the order of the dust-neutral collision frequency. At first glance the large ion-neutral collision frequency (as compared to the ion plasma frequency) seems to pose a problem. This is overcome through an inertialess treatment of the ions and self-consistent treatment of the neutrals. The two fluids (ion and neutral) couple through the collision frequency. The inertialess treatment of the ions and electrons (found in the DENISIS code) is reasonable, as the ion and electron inertial length scales (skin depth) are much smaller than the dust inertial length scale. Additionally, the electron current (and velocity) may be neglected entirely. This is attributed to the depleted electron field. An explicit calculation is shown in Appendix A. In analogy to MHD, here the ions are the inertialess charge carriers and the dust is the inertial charge carrier.

Table 1.2. Plasma parameters for the dusty protosolar nebula. The neutral collisional cross-section, neutral thermal velocity, magnetic field, and dust particle radius are assumed to be (respectively): $\sigma_n = 5x10^{-15}$ cm^2, $B = 10^{-4}$ T, and $r_d = 10^{-6}$ m. (Note all temperatures correspond to 500 K)

		Dust	Ions	Electrons	Neutrals	Units
Number Density	n_k	0.1	1001	1	$1x10^{10}$	m^{-3}
Charge Number	Z_k	10,000	1	1		
Mass	m_k	$1x10^{-16}$	$1.67x10^{-27}$	$9.11x10^{-31}$	$1.67x10^{-27}$	kg
Temperature	$k_B T_k$	$6.90x10^{-21}$	$6.90x10^{-21}$	$6.90x10^{-21}$	$6.90x10^{-21}$	J
Mass Density	ρ_k	$1x10^{-17}$	$1.67x10^{-24}$	$9.11x10^{-31}$	$1.67x10^{-17}$	kg/m^3
Pressure	p_k	$6.90x10^{-22}$	$6.90x10^{-18}$	$6.90x10^{-21}$	$6.90x10^{-11}$	Pa
Plasma Frequency	ω_{pk}	0.0170	41.7	56.4		rad/s
Cyclotron Frequency	ω_{ck}	0.00160	9590	$17.6x10^6$		rad/s
Neutral Collision Frequency	ν_{kn}	0.00415	1020	43,500		Hz
Debye Length	λ_{Dk}	49	49	1540		m
Skin Depth	c/ω_{pk}	$111x10^9$	$45.2x10^6$	$33.4x10^6$		m
Magnetization	c/ω_{ck}	$1.18x10^{12}$	196,000	107		m
Plasma Parameter	Λ	49300	$493x10^6$	$15.3x10^9$		Particles
Plasma Beta	β_k	$1.74x10^{-19}$	$1.74x10^{-15}$	$1.73x10^{-18}$		
Effective Diffusivity	η	$5.28x10^{16}$				$\Omega \cdot m$
Magnetic Reynolds Number	R_m	2.71				
Dust-Electron Collision Frequency	ν_{de}	$7.59x10^{-17}$				Hz
Ion-Dust Collision Frequency	ν_{id}	$1.20x10^{-8}$				Hz
Electron-Ion Collision Frequency	ν_{ei}	$3.78x10^{-30}$				Hz

1.6 Hypothesis

Hannes Alfvén originally proposed that the formation of the solar system was the result of an interplay between gravity, gas dynamics, and dusty plasma interactions (Alfvén, 1954). Following this line of reasoning it makes sense to model the protoplanetary nebula with a dusty plasma code. In doing so one can quantify the dusty plasma processes that impacted the evolution of chondrules during their formation. It has already been shown that dusty plasma dynamo processes can form magnetic fields of the order recorded in the meteorite record. (Wiechen et al., 2002). Shear flow simulations have shown that dusty plasmas can form turbulent structures (Birk and Wiechen, 2002). Additionally, work has been conducted indicating a unique type of shear flow instability capable of forming current sheets(Hawley and Stone, 1998). Each work indicates the formation of current sheets. These current sheets are capable of producing the thermal history recorded in chondrites (Joung et al., 2004). What is unknown is the role magnetic reconnection has in these current sheets on the dust particles.

It is the initial goal of this work to conduct the first self-consistent simulations of magnetic reconnection in a dusty plasma. The second goal is to evaluate magnetic reconnection in a dusty plasma as a chondrule formation mechanism. This will be achieved by conducting simulations of magnetic reconnection in a Harris-like magnetic field configuration with a dusty plasma code. These simulations will probe current sheet configurations, dust dynamics during reconnection, and heating of dust particles due to reconnection. Heating will be evaluated through a testparticle subcode which will track the thermal history of the dust particles. Attention will be be paid to aerodynamic heating of dust particles due to collisions with neutral particles and radiative cooling. I seek to answer the following questions: Under what conditions will magnetic reconnection take place in a dusty plasma? What are the relevant timescales on which magnetic reconnection takes place in a dusty plasma? And does reconnection result in heating of the dust particles? These will be first non-linear self-consistent simulations of magnetic reconnection in a dusty plasma, and the first self-consistent dusty plasma treatment of the chondrule formation problem.

Chapter 2

Methods

The DENISIS (Dust Electron Neutral Ion Self-consistent Integration Scheme) 4-fluid dusty magnetoplasma code allows the investigation of magnetic reconnection in the protosolar nebular environment. The code is based upon a 4-fluid model of a dusty plasma where dust dynamics dominate and neutral interactions are present, allowing one to explore the dynamics of magnetic reconnection across a dusty current sheet. The effects of magnetic reconnection on the dust particles may then be explored through the inclusion of test particles and a model of their thermal evolution.

2.1 The DENISIS Code

The DENISIS code (Schröer et al., 1998) is a three dimensional dusty magnetoplasma code. The code seeks to solve a set of fluid balance equations for 4 species (taking collisions into account). These four species are the electron, singly charged ion, neutral and multiply charged massive dust components. Integration of these equations is accomplished through a modified leap-frog scheme and leap-frog Dufort-Frankel methods (Roache, 1985). The solution is of second order in time and space. The modification to the leap-frog method is done to suppress the odd-even instability. The DENISIS code is a unique tool through which one can investigate the non-linear dynamics of a magnetized partially ionized dusty plasma.

2.1.1 Continuity Equations

The DENISIS code is based upon a set of dusty MHD equations with the inclusion of a neutral background species. The code solves the continuity equation for the dust, ion and neutral species, as follows:

$$\frac{\partial \rho_d}{\partial t} = -\nabla \cdot (\rho_d \vec{v}_d) \tag{2.1}$$

$$\frac{\partial \rho_i}{\partial t} = -\nabla \cdot (\rho_i \vec{v}_i) \tag{2.2}$$

$$\frac{\partial \rho_n}{\partial t} = -\nabla \cdot (\rho_n \vec{v}_n) \tag{2.3}$$

where ρ_k and $\vec{v}_k$ are the species mass density and species fluid velocity respectively (here k is used to index the species: dust, ion, electron, and neutral). The electron mass density is determined from the quasi-neutrality condition:

$$\rho_e = m_e \left(\frac{\rho_i}{m_i} - \frac{Z_d \rho_d}{m_d} \right) \tag{2.4}$$

here Z_d and m_k are the dust charge number and species mass respectively. For the purposes of the simulations, the electron number density was considered to be heavily depleted. The electron depletion is attributed to the massive negative charge found on the dust, which is assumed in the astrophysical environment of the protosolar nebula. The negative charge is attributed to the absence of significant photoionization of the dust particles (Morfill et al., 1993).

2.1.2 Momentum Equations

The DENISIS code integrates the dust and neutral equations of motion. The ion and electron fluids are treated as inertialess. The ion and electron equations of motion may then be substituted into the dust equation of motion through the electric field and dust-electron collisional term. The conservative forms of the dust momentum and neutral momentum equations are:

$$\frac{\partial (\rho_d \vec{v}_d)}{\partial t} = -\nabla \cdot (\rho_d \vec{v}_d \vec{v}_d) - \nabla \left(p_e + p_i + p_d \right) + \frac{1}{4\pi} \left(\nabla \times \vec{B} \right) \times \vec{B} \tag{2.5}$$

$$-\nu_{dn}\rho_d \left(\vec{v}_d - \vec{v}_n \right) - \nu_{in}\rho_i \left(\vec{v}_i - \vec{v}_n \right) - \nu_{en}\rho_e \left(\vec{v}_e - \vec{v}_n \right)$$

$$\frac{\partial (\rho_n \vec{v}_n)}{\partial t} = -\nabla \cdot (\rho_n \vec{v}_n \vec{v}_n) - \nabla p_n + \nu_{dn}\rho_d \left(\vec{v}_d - \vec{v}_n \right) + \nu_{in}\rho_i \left(\vec{v}_i - \vec{v}_n \right) + \nu_{en}\rho_e \left(\vec{v}_e - \vec{v}_n \right) \tag{2.6}$$

where $p, \vec{B}$, and ν_{ab} are the species pressure, magnetic field, and collision frequency between species a and b respectively (here the convention is to refer to $\vec{B}$ as the magnetic field, as opposed to its more accurate name of magnetic induction). Here we have the spatial part of the total fluid derivative ($\nabla \cdot (\rho \vec{v} \vec{v})$), the pressure term ($\nabla p$), the magnetic pressure term ($\vec{j} \times \vec{B}$), and the collisional terms ($\nu_{\alpha\beta}\rho_\alpha \left(\vec{v}_\alpha - \vec{v}_\beta \right)$). The collision frequencies satisfy the following relation $\rho_\alpha \nu_{\alpha\beta} = \rho_\beta \nu_{\beta\alpha}$. The inertialess treatment of the ion and electron fluids restricts the code to examination of processes occurring on length scales longer the the

ion skin depth (and subsequently the electron skin depth). This also places a temporal restriction on the timescales, in that the code is restricted to process occurring on timescales larger than the ion gyro-period.

The ion and electron velocities are calculated from the current density, mobilities, and dust velocity. The current density $\vec{j}$ is calculated from the magnetic field in a familiar fashion

$$\vec{j} = \frac{c}{4\pi} \nabla \times \vec{B}, \tag{2.7}$$

where c is the speed of light. The contribution to the current density via the ions and electrons may be written

$$\vec{w} = \vec{j} + n_d e Z_d \vec{v}_d = e n_i \vec{v}_i - e n_e \vec{v}_e, \tag{2.8}$$

where e, n_k, Z_d, and $\vec{v}_k$ are the electron charge, species k number density, dust charge number, and species k velocity respectively. The term $\vec{w}$ is the sum of the ion and electron contributions to the total current density ($\vec{j}$). The ion velocity is expressed in terms of the electron velocity through mobilities. These mobilities are defined in terms of components of velocity parallel to $\vec{B}$, in the Hall direction ($\vec{E} \times \vec{B}$), and perpendicular to the magnetic field. The interested reader is invited to examine the paper describing the DENISIS code for further details (Schröer et al., 1998) (explicit calculations for the parameters of nebular environment, found in Table 1.2, can be found in Appendix A). In this case, a depleted electron field allows the simplification

$$\vec{w} = e n_i \vec{v}_i. \tag{2.9}$$

Thus the ion velocity becomes an explicit function of the dust velocity ($\vec{v}_d$) and current density ($\vec{j}$). The electron velocity then becomes zero. The implications of the choice of electron collision frequencies is discussed later in this chapter.

2.1.3 Energy Equations

The energy equations are derived from the following general equation

$$\frac{\partial}{\partial t} (\rho_\alpha \varepsilon_\alpha) = -\nabla \cdot (\rho_\alpha \varepsilon_\alpha \vec{v}_\alpha) - \nabla \cdot (p_\alpha \vec{v}_\alpha) + Q_\alpha^E \tag{2.10}$$

where p_α, $\rho_\alpha \varepsilon_\alpha$, and Q_α^E are the species pressure, species internal energy density, and energy source term respectively. The internal energy density relates to the pressure via

$p_\alpha = (\Gamma_\alpha - 1)\rho_\alpha \varepsilon_\alpha$, where Γ_α is the ratio of specific heats for a given species α. The temperature of each fluid is then defined by $T = (m/\rho k_B)p$, where k_B is Boltzmann's constant. The energy equations may then be written:

$$\frac{1}{\Gamma_e - 1}\frac{\partial p_e}{\partial t} = -\frac{1}{\Gamma_e - 1}\nabla \cdot (p_e \vec{v}_e) - p_e \nabla \cdot \vec{v}_e \tag{2.11}$$

$$+\frac{m_n}{m_e + m_n}\rho_n \nu_{ne}(\vec{v}_e - \vec{v}_n)^2 + \frac{m_d}{m_e + m_d}\rho_d \nu_{de}(\vec{v}_d - \vec{v}_e)^2 + \frac{m_i}{m_e + m_i}\rho_i \nu_{ie}(\vec{v}_e - \vec{v}_i)^2$$

$$-2\frac{\rho_d \nu_{de}}{m_d + m_e}\left(\frac{k_B T_e}{\Gamma_e - 1} - \frac{k_B T_d}{\Gamma_d - 1}\right) - 2\frac{\rho_i \nu_{ie}}{m_i + m_e}\left(\frac{k_B T_e}{\Gamma_e - 1} - \frac{k_B T_i}{\Gamma_i - 1}\right)$$

$$-2\frac{\rho_n \nu_{ne}}{m_n + m_e}\left(\frac{k_B T_e}{\Gamma_e - 1} - \frac{k_B T_n}{\Gamma_n - 1}\right)$$

$$\frac{1}{\Gamma_i - 1}\frac{\partial p_i}{\partial t} = -\frac{1}{\Gamma_i - 1}\nabla \cdot (p_i \vec{v}_i) - p_i \nabla \cdot \vec{v}_i \tag{2.12}$$

$$+\frac{m_n}{m_i + m_n}\rho_i \nu_{in}(\vec{v}_i - \vec{v}_n)^2 + \frac{m_d}{m_d + m_i}\rho_i \nu_{id}(\vec{v}_i - \vec{v}_d)^2 + \frac{m_e}{m_e + m_i}\rho_i \nu_{ie}(\vec{v}_i - \vec{v}_e)^2$$

$$-2\frac{\rho_i \nu_{in}}{m_i + m_n}\left(\frac{k_B T_i}{\Gamma_i - 1} - \frac{k_B T_n}{\Gamma_n - 1}\right) - 2\frac{\rho_i \nu_{id}}{m_i + m_d}\left(\frac{k_B T_i}{\Gamma_i} - \frac{k_B T_d}{\Gamma_d - 1}\right)$$

$$-2\frac{\rho_i \nu_{ie}}{m_i + m_e}\left(\frac{k_B T_i}{\Gamma_i} - \frac{k_B T_e}{\Gamma_e - 1}\right)$$

$$\frac{1}{\Gamma_d - 1}\frac{\partial p_d}{\partial t} = -\frac{1}{\Gamma_d - 1}\nabla \cdot (p_d \vec{v}_d) - p_d \nabla \cdot \vec{v}_d \tag{2.13}$$

$$+\frac{m_i}{m_i + m_d}\rho_d \nu_{di}(\vec{v}_d - \vec{v}_i)^2 + \frac{m_n}{m_n + m_d}\rho_d \nu_{dn}(\vec{v}_d - \vec{v}_n)^2 + \frac{m_e}{m_e + m_d}\rho_d \nu_{de}(\vec{v}_d - \vec{v}_e)^2$$

$$-2\frac{\rho_d \nu_{di}}{m_i + m_d}\left(\frac{k_B T_d}{\Gamma_d - 1} - \frac{k_B T_i}{\Gamma_i - 1}\right) - 2\frac{\rho_d \nu_{dn}}{m_n + m_d}\left(\frac{k_B T_d}{\Gamma_d - 1} - \frac{k_B T_n}{\Gamma_n - 1}\right)$$

$$-2\frac{\rho_d \nu_{de}}{m_e + m_d}\left(\frac{k_B T_d}{\Gamma_d - 1} - \frac{k_B T_e}{\Gamma_e - 1}\right)$$

$$\frac{1}{\Gamma_n - 1}\frac{\partial p_n}{\partial t} = -\frac{1}{\Gamma_n - 1}\nabla \cdot (p_n \vec{v}_n) - p_n \nabla \cdot \vec{v}_n \tag{2.14}$$

$$+\frac{m_i}{m_i + m_n}\rho_n \nu_{ni}(\vec{v}_i - \vec{v}_n)^2 + \frac{m_d}{m_n + m_d}\rho_n \nu_{nd}(\vec{v}_n - \vec{v}_d)^2 + \frac{m_e}{m_n + m_e}\rho_n \nu_{ne}(\vec{v}_e - \vec{v}_n)^2$$

$$-2\frac{\rho_n \nu_{ni}}{m_i + m_n}\left(\frac{k_B T_n}{\Gamma_n - 1} - \frac{k_B T_i}{\Gamma_i - 1}\right) - 2\frac{\rho_n \nu_{nd}}{m_n + m_d}\left(\frac{k_B T_n}{\Gamma_n - 1} - \frac{k_B T_d}{\Gamma_d - 1}\right)$$

$$-2\frac{\rho_n \nu_{ne}}{m_n + m_e}\left(\frac{k_B T_n}{\Gamma_n - 1} - \frac{k_B T_e}{\Gamma_e - 1}\right)$$

In these equations one finds collisional heating terms $(\rho_\alpha \nu_{\alpha\beta}(\vec{v}_\alpha - \vec{v}_\beta)^2)$ and thermalization terms $(\rho_\alpha \nu_{\alpha\beta}(\frac{k_B T_\alpha}{\Gamma_\alpha - 1} - \frac{k_B T_\beta}{\Gamma_\beta - 1}))$. The collisional terms act as frictional heating where rel-

ative velocities between species result in heating of the species. The thermalization terms seek to equalize species temperatures through collisions. Note that as the adiabatic index (Γ) for a species approaches unity, the dynamic of that species becomes isothermal. The adiabatic index cannot explicitly be set to unity as the thermalization terms contain reciprocals of $\Gamma - 1$, which is not numerically tractable. In order to treat such a case, the relevant equation for a given species is replaced with the equation $u_k = \left(\frac{1}{2}\rho_k\right)^{1/\Gamma_k}$, where pressure may be defined in terms of $p_k = 2u_k^\Gamma$.

2.1.4 Induction Equation

This set of equations is closed by Faraday's law

$$c\nabla \times \vec{E} = -\frac{\partial \vec{B}}{\partial t}. \tag{2.15}$$

The intertialess ion equation of motion may be written in terms of the electric field giving

$$\vec{E}' = \vec{E} + \frac{1}{c}\vec{v}_i \times \vec{B} = \frac{m_i}{e}\frac{\nabla p_i}{\rho_i} - \frac{m_i}{e}\nu_{id}(\vec{v}_d - \vec{v}_i) - \frac{m_i}{e}\nu_{in}(\vec{v}_n - \vec{v}_i) - \frac{m_i}{e}\nu_{ie}(\vec{v}_e - \vec{v}_i) \tag{2.16}$$

where the gravitational term has been neglected. This is substituted into Faraday's law to give

$$\begin{aligned}\frac{\partial \vec{B}}{\partial t} = & -\frac{m_i c}{e}\nabla \times \left(\frac{\nabla p_i}{\rho_i}\right) + \nabla \times \left(\vec{v}_i \times \vec{B}\right) - \eta\nabla^2\vec{B} \\ & -\frac{m_i c}{e}\nabla \times \left[\nu_{id}(\vec{v}_i - \vec{v}_d) + \nu_{in}(\vec{v}_i - \vec{v}_n) + \nu_{ie}(\vec{v}_i - \vec{v}_e)\right].\end{aligned} \tag{2.17}$$

Here a resistive term (η) has been included giving added utility to the code. The depleted electron field allows this equation to be written as

$$\begin{aligned}\frac{\partial B}{\partial t} = & -\frac{m_i c}{e}\nabla \times \left(\frac{\nabla p_i}{\rho_i}\right) + \frac{m_i}{m_d}Z_d\nabla \times \left(\frac{\rho_d}{\rho_i}\vec{v}_d \times \vec{B}\right) + \frac{m_i c}{4\pi e}\nabla \times \left(\frac{\nabla \times \vec{B}}{\rho_i} \times \vec{B}\right) - \tilde{\eta}\nabla^2\vec{B} \\ & -\frac{m_i}{e}\nabla \times \{\frac{n_d}{n_i}\left[\left(Z_d - \frac{n_i}{n_d}\right)\nu_{id} + Z_d\nu_{in}\right]\vec{v}_d - \nu_{in}\vec{v}_n\},\end{aligned} \tag{2.18}$$

In this form the resistivity may be written in terms of the collision frequencies and the appended resistive term

$$\tilde{\eta} = \eta + \frac{m_i c^2}{4\pi n_i e^2}(\nu_{id} + \nu_{in}). \tag{2.19}$$

In Appendix B, a more general form of Ohm's law is presented to indicate the scaling of various terms (including ion inertial terms). The ion inertial term scales as the ion skin depth which is $7,200$ km. It can also be shown that a temporal constraint exists regarding the neglect of ion inertia. A posteriori we find that ion acceleration was ~ 0.1 in normalized units while the ion-neutral collisional forces were $\sim 20,000$ in normalized units. The inertialess ion assumption present here is only valid for length scales greater than the ion skin depth. The Hall term and ion-stress term scale as the dust skin-depth ($c/\omega_{pd}=2.19$). Finally, the collisional resistivity term (due predominately to ion neutral collisions) is proportional to the effective resistivity ($\bar{\eta}$) and inversely proportional to the flow velocity. The effective resistivity for the protosolar nebula (5.28×10^{16} $\Omega \cdot m$) indicates that even for Alfvénic flows ($V_{alfven} \sim 10^6$ m/s) the collisional resistivity is important over large length scales. The choice of grid scale must be larger than the length scales on which ion inertia plays a role ($7,200$ km) so that the inertialess ion fluid assumption made in DENISIS is accurate.

This closes our set of equations for the DENISIS code. It should be noted that equation 2.17, is the equation integrated by the code. This diffusivity (η) is independent of the collision frequencies and was included in order to compare collision frequencies against an explicit resistivity (representative of the collision frequencies). It should also be noted that the collisional terms in equation 2.17 can be switched off in the code without affecting the collisional terms in the other equations. This is achieved through multiplication of the terms by integer coefficients in the DENISIS code itself.

2.1.5 Numerical Method

DENISIS uses two numerical methods to integrate these equations. The hyperbolic balance equations (continuity, momentum, energy) are solved using a modified leap-frog scheme while the parabolic induction equation is solved using a leap-frog Dufort-Frankel scheme. The modification to the leap-frog scheme is accomplished by splitting the scheme into three steps. In the first step a spatial average is performed over a half time step, the second step substitutes this averaged source term by a newly computed one, and in the third step a second half time step is performed with the new source term. Here spatial average refers to an averaging process that takes into account distances between neighboring grid points (as opposed to a statistical average). An artificial viscosity is added in step two so

as to suppress the odd-even instability. To illustrate, examine a simple one-dimensional transport equation,

$$\frac{\partial u(x,t)}{\partial t} = -\frac{\partial u(x,t)}{\partial x} + \alpha u(x,t).$$ (2.20)

The scheme splits the leap-frog method into 3 auxiliary steps: 1. As a first approximation the unknown quantity u_i^t is replaced by its spatial average, then one performs a half time step to obtain

$$u_i^t = u_i^{t-1/2} - \frac{\Delta t}{2\Delta x}\left(u_{i+1}^t - u_{i-1}^t\right) + \frac{\alpha\Delta t}{2}\left(u_{i+1}^t + u_{i-1}^t\right).$$ (2.21)

2. Substitute the average source term by the newly computed one,

$$\tilde{u}_i^t = u_i^t - \frac{\alpha\Delta t}{2}\left(u_{i+1}^t + u_{i-1}^t\right) + \alpha\Delta t u_i^t.$$ (2.22)

3. Perform the second half time step with the new source term,

$$u_i^{t+1/2} = \tilde{u}_i^t - \frac{\Delta t}{2\Delta x}\left(u_{i+1}^t - u_{i-1}^t\right) + \alpha\Delta t u_i^t.$$ (2.23)

Note that an artificial viscosity is added after step 2 in order to suppress the odd-even instability. This viscosity takes the form of a spatial average and is only applied to points on the grid where the code has detected grid scale oscillations to be present. Summing up these steps the canonical form of the leap-frog scheme is recovered

$$u_i^{t+1} = u_i^{t-1} - \frac{\Delta t}{\Delta x}\left(u_{i+1}^t - u_{i-1}^t\right) + 2\alpha\Delta t u_i^t.$$ (2.24)

To illustrate the leap-frog Dufort-Frankel scheme (Roache, 1985), examine the advection diffusion equation

$$\frac{\partial u(x,t)}{\partial t} = -\frac{\partial u(x,t)}{\partial x} + \alpha\frac{\partial^2 u(x,t)}{\partial t^2}.$$ (2.25)

The scheme uses the three-point centered difference of the Richardson scheme (for the diffusion term) but replaces the center term T_j^n with an average of the neighboring time steps to give

$$\frac{u_i^{t+1} - u_i^{t-1}}{2\Delta t} = -\frac{u_{i+1}^t - u_{i-1}^t}{2\Delta x} + \alpha\frac{u_{i-1}^t - \left(u_i^{t-1} + u_i^{t+1}\right) + u_{i+1}^t}{\Delta x^2}.$$ (2.26)

The familiar explicit form is

$$u_i^{t+1} = \left[(1 - 2s)u_j^{t-1} - 2c\left(u_{i+1}^t - u_{i-1}^t\right) + 2s\left(u_{i+1}^t + u_{i-1}^t\right)\right] / (1 + 2s)$$ (2.27)

where $s = \alpha\Delta t/\Delta x^2$ and $c = \Delta t/\Delta x$. The solution will then be second order in space and time (Press et al., 2002). Should the diffusive term (in this case resistivity) become zero then the method reduces to the hyperbolic leap-frog method.

The stability of these methods is determined by the Courant number. The choice of time step and grid scale are discussed in Section 2.2.1, as is their impact on stability of the code. There is an additional constraint which exists for the time step alone. It is imposed by the source terms and the nature of numerical integration. Take the following simple equation:

$$\frac{\partial f}{\partial t} = \alpha g \tag{2.28}$$

where f is the function we wish to integrate and g is some source function (which may be a function of f). This equation then becomes

$$f^{t+1} = f^{t-1} + \Delta t \alpha g^t \tag{2.29}$$

where the spatial subscript i has been dropped for clarity and g represents some function which may be a function of f (in our case the relative velocities between species in the momentum equation). It becomes clear that the product of Δt and α scale the value of g. In order for this algebraic equation to be numerically tractable it is important that such a product scale the source term to a value that is of the order of f. A more detail discussion of the source terms is conducted in the next section (Section 2.2) with explicit calculations shown in Appendix C. Numerical tractability is achieved through careful choice of the time step.

2.2 Parametrization

All parameters are normalized to typical values for the protosolar nebula. The typical magnetic field, fluid mass density, and timescale are chosen as $\hat{B} = 10^{-4}$ [T], $\hat{\rho} = 10^{-17}$ [kg/m^3], and $\hat{t} = 1800$ [s]. The magnetic field corresponds to the magnitude of magnetic fields recorded in the chondrules. The mass density is appropriate for assumed number densities and masses of the dust particles in the protosolar nebula. The timescale corresponds to 30 minutes. The time step is chosen to be $\Delta t = 0.0001$ giving a temporal resolution of 0.36 [s]. These parameters then determine the normalizations found in Table 2.1. Note that the stereotypical length scale presented here (50,700,000 [km]) is four orders of

Table 2.1. Normalizations for the protosolar nebula. Implicit in these calcualtions is the assumption $\hat{n} = 0.1$.

$\hat{B} = 10^{-4}$ [T]		$\hat{\rho} = 10^{-17}$ [kg/m^3]		$\hat{t} = 1800$ [s]	
$\hat{v}$	=	$\hat{B}/\sqrt{\mu_0\hat{\rho}}$	=	28.2×10^6	[m/s]
$\hat{L}$	=	$\hat{t}\hat{v}$	=	5.07×10^{10}	[m]
$\hat{f}$	=	$1/\hat{t}$	=	5.56×10^{-4}	[Hz]
$\hat{\omega}$	=	$2\pi/\hat{t}$	=	0.00350	[rad/s]
$\hat{j}$	=	$\hat{B}/\mu_0\hat{L}$	=	1.57×10^{-9}	[A/m^2]
$\hat{p}$	=	$\hat{B}^2/2\mu_0$	=	0.00398	[N/m^2]
$\hat{E}$	=	$\hat{B}\hat{v}$	=	$2,820$	[N/C]
$k_B\hat{T}$	=	$\hat{p}/\hat{n}$	=	0.0398	[J]
$\hat{\eta}$	=	$\hat{L}^2/\hat{t}$	=	1.43×10^{18}	[$\Omega \cdot m$]
$\hat{e}_c$	=	$\frac{1}{L}\sqrt{\frac{\hat{m}}{\mu_0\hat{n}}}$	=	5.56×10^{-16}	[C]

magnitude larger than the ion skin depth (the aforementioned lower limit of consideration without inclusion of ion inertial dynamics). This is distance is equivalent to approximately 8000 [Re] or 1/3 [Au] for reference. The nebula is assumed to be around 100 [Au] in size.

Table 2.2 shows these normalizations applied directly to the values associated with the protosolar nebula (found in Table 1.2). The majority of parameters scale to numerically tractable values. The mass densities for the dust and neutral fluids are of the order unity. The low ion mass density is still numerically tractable through the implementation of 64 bit floating point values which provide approximately 15 significant figures of storage. The vector quantities (velocity and magnetic field) are expected to also be of the order unity or less. The normalized pressures (and subsequently temperatures) present difficulties which are discussed and resolved below.

The pressures present a difficulty due to their low values. Specifically, the code integrates a modified form of the pressure equations where the substitution $p = 2u^\Gamma$ is made. Thus the pressure equations transform as follows:

$$\frac{\partial p}{\partial t} = -\nabla \cdot (p\vec{v}) - (\Gamma - 1)p\nabla \cdot \vec{v} \Rightarrow \frac{\partial u}{\partial t} = -\nabla \cdot (u\vec{v}). \tag{2.30}$$

The values of u for the various species become: $u_{d0} = 3.65x10^{-12}$, $u_{i0} = 9.20x10^{-10}$, $u_{e0} = 1.45x10^{-11}$, and $u_{n0} = 1.45x10^{-5}$ (assume $\Gamma = 5/3$). The difficulty arrises from the Harris sheet configuration that is utilized for an initial condition. These difficulties are addressed in the description of the initial condition (Section 2.3.1). At this point it should suffice to say that the low plasma beta $\beta = \frac{p}{B^2/2\mu_0}$ these parameters represent is numerically difficult to treat. Specifically, if we examine the neutral beta (neutral pressure to magnetic pressure ratio) we find $\beta_n = 1.73 \times 10^{-8}$. This low neutral beta, coupled with the large neutral collision frequencies, suggests that neutral pressure forces are small. The suppression of neutral pressure forces in the neutral equation of motion may then be considered. As a result, the neutral sound waves will also be suppressed. The large ion-neutral collision frequency suggests that these waves may be highly damped if the neutral mass density is much smaller than the dust mass density.

The collision frequencies play important roles in defining the coefficients for many of the source terms present. The time step for the code must be chosen such that the product of the time step and source term coefficients is smaller than the quantity in question (the change in any quantity should be less than the value of the quantity). Appendix C contains calculations of the coefficients in the various equations. The largest coefficient is due to the ion-neutral thermalization term. It has been found that for numerical stability this term must be suppressed. This limitation can be overcome through the assumption that the ion and neutral temperatures are same owing to their large collision frequency. Taking into account the normalized ion pressure (being smaller than that of the neutrals), the time step is chosen to be $\Delta t = 0.0001$. The small time step provides excellent analytic stability parameters, while still allowing the simulation to progress in a timely manner. A simulation of $90,000$ time steps takes ~ 76 hours on an AMD Opteron chip.

A quick note should be made on the electron collisional terms in light of the neglect of electron dynamics. In the equations of motion the electron-neutral collision frequency acts as a viscosity in both the dust and neutral equations of motion. The zero electron velocity assumption is the source of this term. In order to avoid complications, as a result of an unbalanced term in the momentum equations, its value is chosen to be zero. Thus in all equations the electron neutral collision terms disappear. The same is done for the ion-electron collision frequency. For technical reasons, involving the calculation of the

(neglected) electron velocity, the dust-electron collision frequency cannot be set explicitly to zero. A value of 1.37×10^{-13} is chosen so as to minimize the effects of its non-zero value. The effect being only seen as a small temperature reservoir for the dust.

In this parametrization, it is assumed that the electron velocity does not contribute to the currents. There are two important facts upon which this assumption is based. First, the electron density is highly depleted. The dust particles are the predominate negative charge carrier. The second, is that the electron mobility is small compared to that of the ions in all but the parallel direction. Calculations show that the ion contribution to the total current is approximately two orders of magnitude larger than the electron contribution. Thus for the dynamics under consideration, the approximation of negligible electron velocities is appropriate. Appendix A shows the details of this calculation. The neglect of ion inertial dynamics is also justified as the problem is concerned with length scales much larger than the dust Debye length. The length scales (and time scales) which are considered in this problem which are much larger than the ion inertial length scale (ion skin depth, Table 2.2). Therefore, the neglect of the electron velocity and non-inertial ions is completely justified in this parameter regime.

2.2.1 The Numerical Domain

The simulation domain chosen for the code is a three dimensional cartesian box. The simulation domain is defined in Table 2.3. The grid itself is composed of 255 nodes in the $\hat{x}$ direction, 127 nodes in the $\hat{y}$ direction and 15 nodes in the $\hat{z}$ direction. One node at each boundary is associated with the numerical grid, while the next neighbor is the physical boundary. As a result the grid spacing is determined by $n - 2$ grid points, the extra grid points being used for the numerical boundary (where n is the number of grid points in a given direction). The numerical boundary is a requirement of the finite difference methods employed by the code. The grids are taken to be equidistant. The corresponding physical grid scales are $20,000,000\ km$ in x, $4,060,000\ km$ in y, and $2,540,000\ km$ in z. These distances are well above the ion skin depth (ion-inertial limit), $45,200\ km$, allowing for the inertialess treatment of the ions. The time step is taken to be $\Delta t = 0.0001$ for numerical stability (this is at the limit for neglect of the ion inertia).

The stability of the leap-frog method is difficult to gauge in the compressible flow limit.

Table 2.2. Normalization of the plasma parameters for the dusty protosolar nebula. Values based on those found in Table 1.2. Normalizations found in Table 2.1.

		Dust	Ions	Electrons	Neutrals
Number Density	n_k	1	10010	10	$1x10^{11}$
Charge Number	Z_k	10,000	1	1	
Mass	m_k	1.00	$1.67x10^{-11}$	$9.11x10^{-15}$	$1.67x10^{-11}$
Temperature	k_BT_k	$1.73x10^{-19}$	$1.73x10^{-19}$	$1.73x10^{-19}$	$1.73x10^{-19}$
Mass Density	ρ_k	1.00	$1.67x10^{-7}$	$9.11x10^{-24}$	1.67
Pressure	p_k	$1.73x10^{-19}$	$1.74x10^{-15}$	$1.73x10^{-18}$	$1.73x10^{-8}$
Plasma Frequency	ω_{pk}	4.86	11,900	16,100	
Cyclotron Frequency	ω_{ck}	0.457	$2.74x10^6$	$5.03x10^9$	
Neutral Collision Frequency	ν_{kn}	7.46	$1.83x10^6$	$7.82x10^7$	
Debye Length	λ_{Dk}	$9.66x10^{-10}$	$9.66x10^{-10}$	$3.04x10^{-8}$	
Skin Depth	c/ω_{pk}	2.19	0.000892	0.000659	
Magnetization	c/ω_{ck}	23.3	$3.86x10^{-6}$	$2.11x10^{-9}$	
Plasma Parameter	Λ	49300	$493x10^6$	$15.3x10^9$	
Plasma Beta	β_k	$1.74x10^{-19}$	$1.74x10^{-15}$	$1.73x10^{-18}$	
Effective Diffusivity	η	0.0369			
Magnetic Reynolds Number	R_m	2.71			
Dust-Electron Collision Frequency	ν_{de}	$1.37x10^{-13}$			
Ion-Dust Collision Frequency	ν_{id}	$2.16x10^{-5}$			
Electron-Ion Collision Frequency	ν_{ei}	$6.80x10^{-27}$			

Table 2.3. Parameters defining the numerical domain of the simulation. The parameter L defines the physical domain of the problem $n - 2$ gridpoints span this distance (extra grid-points used to determine numerical boundary). The right side of the table presents stability parameters for the Leap-Frog (modified courant number) and DuFort-Frankel schemes. The parameters s is the linear stability parameter and χ indicates the presence of harmonic solutions.

Length	Gridpoints	Spacing	$c = \Delta t / \Delta l$	$s = \Delta t / \Delta l^2$	$\chi = \Delta t^2 / \Delta l^2$
$L_x = 100$	$n_x = 255$	$\Delta x = 0.395$	$c_x = 0.000253$	$s_x = 0.000641$	$\chi_x = 6.40 \times 10^{-8}$
$L_y = 10$	$n_y = 127$	$\Delta y = 0.08$	$c_y = 0.00125$	$s_y = 0.0156$	$\chi_y = 1.56 \times 10^{-6}$
$L_z = 0.65$	$n_z = 15$	$\Delta z = 0.05$	$c_z = 0.002$	$s_z = 0.04$	$\chi_z = 4.00 \times 10^{-6}$
		$\Delta t = 0.0001$			

Linear analysis suggests that, in the incompressible flow limit the leap-frog routine has the following stability restriction (in three dimensions)

$$v_x c_x + v_y c_y + v_z c_z \leq 1 \tag{2.31}$$

where the modified courant numbers ($c = \Delta t / \Delta l$) are defined as shown in Table 2.3. It is safe to say that for non-relativistic flows the leap-frog routine is stable on our grid (note the normalized velocity of 28.2×10^6 m/s). For compressible flows it is customary to modify the courant stability limit through a change in velocity term (Roache, 1985). Here the incompressible flow velocity (v) is replaced with a summation of the flow velocity and stereotypical propagation velocity ($w = |v| + a$; where a could be the sound speed, shock velocity, Alfvén velocity, etc). The modified stability criterion then becomes

$$w_x c_x + w_y c_y + w_z c_z \leq \frac{\Delta x \Delta y \Delta z}{\left(\Delta x^2 + \Delta y^2 + \Delta z^2\right)^{3/2}}. \tag{2.32}$$

Here modified courant numbers have been used ($c = \Delta t / \Delta l$). For our simulation grid the right hand side of the equation is 0.0236. A flow velocity twice the Alfvén velocity should still be numerically tractable for this time step.

The stability of the leap-frog DuFort-Frankel scheme can also be gauged from grid parameters in the linear incompressible regime. The purely diffusive term in this scheme is stable for all positive values of ηs (Fletcher, 1991). When combined with the leap-frog advection term, the previously derived stability constraint on the leap-frog method becomes

the limiting factor (as is the case with our induction equation). Our choice of time step and grid scale is stable for trans-Alfvénic flows. An additional constraint must be considered for the DuFort-Frankel method in terms of the consistency of the method (Roache, 1985). Specifically, the method admits solutions which are harmonic in time. These harmonics can be suppressed if $\eta\chi$ is kept small. A cursory examination of χ indicates that even for large $\eta > 1$ these modes will be suppressed.

2.3 Simulation

The simulations, which are discussed in this thesis, are the first studies of the onset and nonlinear dynamics of magnetic reconnection in a dusty plasma. An equilibrium current sheet configuration was sought so that the dynamics of reconnection dominated over the collisional current sheet dynamics. An equilibrium was achieved through the implementation of a ballistic relaxation technique (Hesse and Birn, 1993) before any reconnective perturbation was applied. This reconnective perturbation was chosen to be of a form consistent with linear reconnective theory. A test particle sub-code is utilized to gauge dust particle heating due to neutral collisions during the reconnective dynamics.

2.3.1 Initial Condition

A Harris like magnetic field configuration (Harris, 1962) is ballistically relaxed to allow for a perturbation to be applied to the current sheet and reconnection to commence. The Harris configuration provides an analytic equilibrium current sheet in the regime of ideal plasma physics. The presence of collisions destabilizes this configuration resulting in a non-equilibrium initial condition. Modifications to the current sheet profiles are made to help minimize the non-equilbrium effects. While these modifications do not allow for a true equilibrium they do allow for a ballistic relaxation technique to be employed in an attempt to find a near-equilibrium configuration. This technique allows the configuration to enter a relaxed state where a perturbation can be applied to the current sheet. A Harris like magnetic field profile allows the study of reconnection in a dusty plasma without knowledge of the exact formation process of the current sheet.

The current sheet configuration described by Harris provides a simple current sheet configuration with which to explore reconnection in a dusty plasma. The kinetic equilib-

rium found by Harris can be extended to a fluid equilibrium. The configuration consists of a one dimensional magnetic field configuration

$$\vec{B} = B_o \tanh\left(\frac{y}{\delta}\right) \hat{x} \tag{2.33}$$

where $B_o = 1.0$ and $\delta = 1.00$ are the asymptotic magnetic field strength and current sheet thickness respectively (in normalized units). An equilibrium between the magnetic force $(\vec{j} \times \vec{B})$ and plasma pressure must exist for this configuration to be stable. Thus the plasma pressure becomes

$$p\left(y\right) = p_o + \frac{B_o^2}{2\mu_o} \cosh^{-2}\left(y/\delta\right) \tag{2.34}$$

where p_o and μ_o are the asymptotic plasma pressure and permeability of free space respectively. In the derivation of the Harris sheet an implicit assumption is made that the current sheet is isothermal. The plasma density is then determined from this assumption

$$\rho\left(y\right) = \frac{p_o}{k_B T} + \frac{B_o^2}{2\mu_o k_B T} \cosh^{-2}\left(y/\delta\right), \tag{2.35}$$

where k_B and T are the Boltzmann constant and plasma temperature respectively. The multi-fluid nature of the DENISIS code requires a more precise description of this configuration.

The magnetic field configuration provided through the Harris derivation may be modified to fit the multi-fluid nature of the DENISIS code. The Harris magnetic configuration is chosen (subsequently the current sheet profile found by Harris). An equilibrium is achieved through a balance between magnetic forces and the total plasma pressure. A complication is introduced through the multi-fluid nature of the total plasma pressure $(p = p_d + p_i + p_e)$. The neutral pressure does not contribute to the total plasma pressure, which by definition includes plasma constituents only. Tight collisional coupling between the ions and neutrals can have an influence on force balance through thermal contact and unbalanced neutral pressure gradients (which are small due to the small neutral beta value). A simplification is made by assuming the electron pressure does not contribute significantly to the pressure balance $(p_e\left(y\right) = p_{eo})$. This is directly attributed to the depleted electron regime which the parameters for the nebula represent. The electric field perpendicular to the current sheet is taken to be zero (see Eqn. 2.16). This implies that the ion
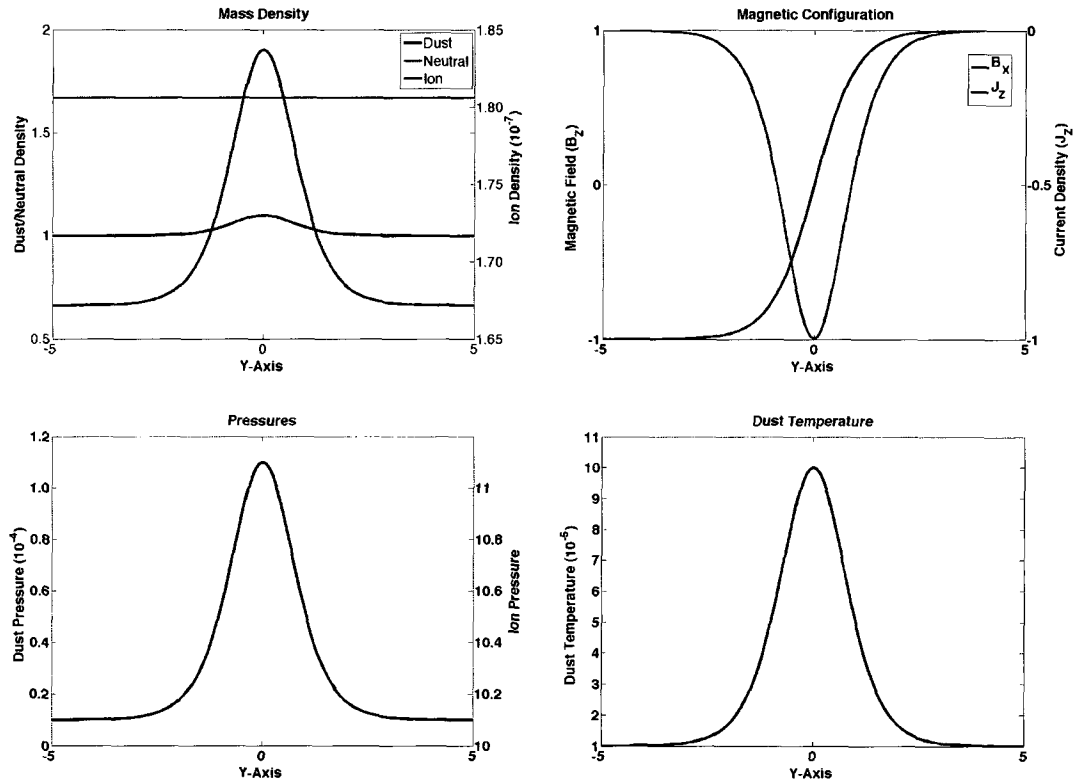
Figure 2.1. Initial density, pressure, temperature and magnetic field profiles. Electron density profile is constant across the simulation domain: $\rho_{eo} = 8.98 \times 10^{-15}$. The dust and ion pressures share similar profiles. Electron and neutral pressures are constant across the simulation domain: $p_{eo} = 0.01$ and $p_{no} = 1.01 \times 10^{9}$. Ion, electron, and neutral temperatures are constant across the simulation domain: $t_{io} = t_{eo} = t_{no} = 0.00101$.

pressure should completely balance the magnetic pressure if the dust is taken to be stationary (only ion contributions to the current density). The initial conditions (Figure 2.1) for the simulation become

$$p_d(y) = \frac{p_{io}}{Z_d} + \frac{A_o B_{xo}^2}{2\mu_o Z_d \cosh^2(y/\delta)} - \frac{n_e}{Z_d}, \tag{2.36}$$

$$p_i(y) = p_{io} + \frac{A_o B_{xo}^2}{2\mu_o \cosh^2(y/\delta)}, \tag{2.37}$$

$$p_e(y) = n_e k_B T_o, \tag{2.38}$$

$$p_n(y) = n_n k_B T_o, \tag{2.39}$$

$$\rho_d(y) = m_d \frac{p_d(y)}{k_B T_o}, \tag{2.40}$$

$$\rho_i(y) = m_i \frac{p_i(y)}{k_B T_o}, \tag{2.41}$$

$$\rho_e(y) = m_e \left(\frac{p_i(y)}{m_i} - \frac{Z_d \rho_d}{m_d} \right), \tag{2.42}$$

$$\rho_n(y) = m_n n_n \tag{2.43}$$

where $A_o = 2$ has been included to insure that the non-equilibrium dynamics are away from the current sheet. The following quantities are noted in simulation units (normalized): $p_{io} = 10.1$, $Z_d = 10000$, $B_{xo} = 1.0$, $n_e = 10$, $k_B T_o = 0.001$, $n_n = 1 \times 10^{11}$, $m_d = 1$, $m_i = 1.67 \times 10^{-11}$, $m_e = 8.98 \times 10^{-15}$, and $m_n = 1.67 \times 10^{-11}$. The densities are larger in the current sheet to prevent its depletion during the ballistic relaxation process. The set of initial conditions, presented here, provides a best guess estimate of the configuration of a current sheet in the protosolar nebula.

The achieved current sheet configuration is not in equilibrium. The pressure profiles have been chosen to approximate a force balance and minimize electric fields perpendicular to the current sheet while providing non-equilibrium motions away from the current sheet. The ballistic relaxation technique attempts to provide a force balance while minimizing the perpendicular electric field and dampening the motions of the plasma away from the current sheet. The temperatures in this configuration are at equilibrium

far from the current sheet. In the current sheet, collisional heating makes a thermal equilibrium difficult. The ballistic relaxation will allow the species time to adjust their temperatures through convection and thermalization. The current sheet configuration will reach a dampened state, characterized by a minimized force norm, through the ballistic relaxation procedure.

2.3.2 Ballistic Relaxation

The system is ballistically relaxed in order to find both a pressure equilibrium and thermally relaxed current sheet. Ballistic relaxation implies an evolution where the system kinetic energy is set to zero once it has reached a maximum. In simple systems the maximum in kinetic energy also corresponds to a minimum in potential energy and thus a minimum in the unbalanced forces in the system. These unbalanced forces in the system are characterized by the force norm. In this simulation the force norm is taken to be the sum of the square of the residual force in the system, attributed to an imbalance between the plasma and magnetic pressures. For the current sheet system, the component of the force perpendicular to the current sheet ($\hat{y}$ direction) is of the most relevance (as is the kinetic energy in that direction). The residual force in the system can be written

$$\vec{F}_{residual} = -\nabla \left(p_d + p_i + p_e \right) + \vec{j} \times \vec{B}. \tag{2.44}$$

The force norm may then be calculated,

$$F_n = \int \vec{F}_{residual} \cdot \vec{F}_{residual} dV. \tag{2.45}$$

A frictional term is added to the dust and neutral equations of motion in order to dampen the effects of the initial non-equilibrium choice of the pressure profiles. The coefficient (α)in the term has the time dependent form,

$$\alpha = \begin{cases} 10\cos\left(\frac{\pi}{2}t\right) + 0.1 & \text{if } t < 1.0 \\ 0.1 & \text{if } 1.0 \leq t < 3.0 \\ 0.0 & \text{if } t \geq 3.0. \end{cases} \tag{2.46}$$

Diagnostic outputs of the kinetic, internal, and magnetic energies are created during this period of ballistic relaxation, along with the force norm. The ballistic relaxation lasts for three scale times in normalized parameters.

2.3.3 Reconnective Mode

Magnetic reconnection across the relaxed current sheet is achieved through a velocity perturbation. The reconnective mode is defined by an inflow and an outflow perturbation. The collisional (and/or resistive) terms in the induction equation are also switched on at this point in the simulation. Throughout reconnection various parameters are tracked in the reconnection region, defined by the initial perturbation. These parameters include fluxes (mass and magnetic) through the surfaces defined by this reconnection region. Various parameter regimes are investigated in order to better characterize reconnection in the protosolar nebula.

Reconnection in the current sheet is achieved through a velocity perturbation. The general structure of the perturbation includes an inflow towards the current sheet (in the $\hat{y}$ direction) and an outflow along the current sheet (in the $\hat{x}$ direction) (Figure 2.2). The current sheet itself flows in the $\hat{z}$ direction. The dust velocity is perturbed and ion velocities are set so as to minimize the formation of new currents. The perturbation was conducted in a Sweet-Parker like fashion where

$$v_{outflow} = v_{Alfven} \tag{2.47}$$

$$L_{inflow}v_{inflow} = L_{thickness}v_{outflow}. \tag{2.48}$$

Here R_m is the magnetic Reynolds number for the plasma and v_{Alfven} is the asymptotic Alfvén velocity. A distinction can be made between the applied reconective mode and reconnection itself through examination of flows in the (unperturbed) $\hat{z}$ direction, and to a lesser extent through equilibration of the inflow and outflow mass fluxes.

In order to characterize reconnection, certain parameters (and fluxes) are calculated in (through) the reconnection region. In these simulations a region defined by the reconnective perturbation was used to track various values (length in x of 20.0 and width in y of 2.0). Analytic models of reconnection often share conservation of mass and magnetic flux into the reconnection region. These quantities act as markers to help describe the state of reconnection. The reconnection rate is given by the maximum of the integral $\int E_{\parallel}ds$ taken along a magnetic field line. For the resistive runs ($\eta \neq 0$) we track

$$\vec{E} = \frac{m_i}{e}\left(\frac{\nabla p_i}{\rho_i}\right) - \frac{1}{c}\left(\vec{v}_i \times \vec{B}\right) + \eta\vec{j}. \tag{2.49}$$
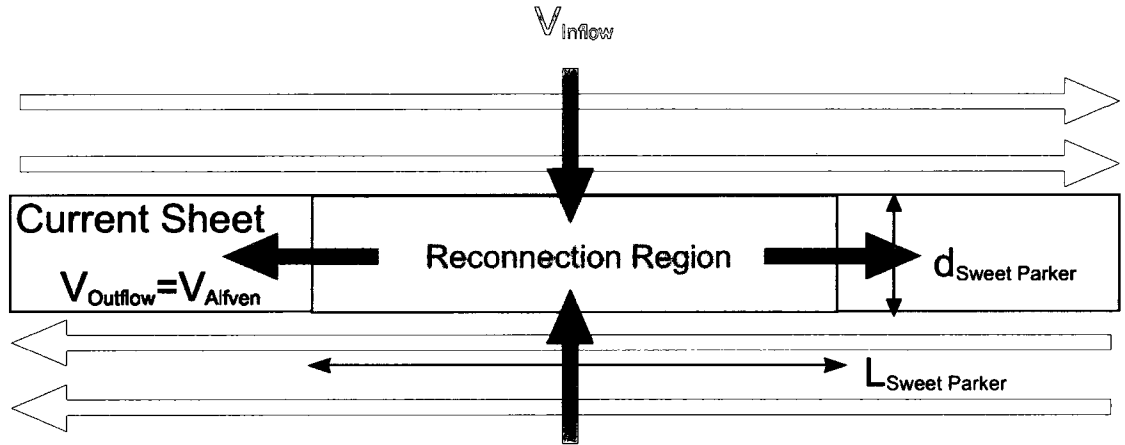
Figure 2.2. A diagram of the initial velocity perturbation applied to the current sheet so as to excite reconnection. The perturbation is shown in the plane but is applied to the whole box. The reconnection region is defined by $d = 1.0$ and $L = 20.0$. Red arrows indicate magnetic field.

For the runs involving collision frequencies the electric field may be written,

$$\vec{E} = \frac{m_i}{e}\left(\frac{\nabla p_i}{\rho_i}\right) - \frac{1}{c}\left(\vec{v}_i \times \vec{B}\right) + \frac{m_i}{e}\left(\nu_{id}\left(\vec{v}_i - \vec{v}_d\right) + \nu_{in}\left(\vec{v}_i - \vec{v}_n\right) + \nu_{ie}\left(\vec{v}_i - \vec{v}_e\right)\right). \tag{2.50}$$

These values are used to compare runs of the simulation. Calculation of the reconnection rate is achieved by integrating $E_\parallel$ along various field lines undergoing reconnection and taking the maximum integral as the reconnection rate. A field line which passes through the maximum of $E_\parallel$ is included in each calculation. Each term in the equations for the electric field scale according to coefficients (with the exception of the advection term, $\vec{v}_i \times \vec{B}$). The ion pressure gradient term has a coefficient that scales as the square of the inverse ion plasma frequency (which results in a small coefficient). The collisional terms have coefficients that scale with the collision frequencies $m_i\nu/e$. These coefficients have values 1.25×10^{-12}, 0.106, and 3.94×10^{-37} for the ion-dust, ion-neutral, and ion-electron collisional terms respectively. The non-ideal dynamics in the system are due to the ion-neutral interactions and ion pressure gradient terms.

2.4 Test-Particle Heating Code

In order to evaluate the heating effects of reconnection on the dust, a model for heating of the individual particles was developed. The DENISIS fluid code does not calculate the individual particle temperatures of the dust. Instead it tracks the temperature of the dust fluid component (through the pressure and density). In order to determine the heating of the particles, the heating mechanisms acting on the particles must be considered. Suitable mechanisms include aerodynamic heating (dust-neutral drag), conduction, and radiative heat transfer. The supersonic velocities of the dust particles coupled with the space environment suggest that drag heating may play an important role. Examination of the nebular parameters in Table 1.2 show a dust Alfvén velocity many orders of magnitude larger than the neutral sound speed. Radiative cooling of the particles is difficult to incorporate into the theory of chondrule formation, given the necessary heating and cooling rates. It is unlikely that it played a large role in chondrule formation as cooling times were on the order of hours to days (radiative heat transfer cools the particles far too quickly to be considered a relevant part of their formation mechanism). Conduction to the background neutral gas is a far more likely situation. This places a constraint on chondrule formation locations in the nebular environment. Particles in the nebular corona and at the surface of the disk itself would surely experience radiative cooling to deep space. Such a particle would be cooled from a temperature of $1500\ K$ to $4\ K$ in the time span of a few seconds (not the hours to days necessary for chondrule formation). From this point forward the notion of magnetic reconnection as a chondrule heating mechanism will be restricted to the interior of the nebular disk itself. Here radiative cooling will be negligible given the large neutral density providing a thermal bath for the dust particles. While magnetic reconnection may also occur in other dusty-plasma environments of the nebula, only the disk interior provides the thermal bath necessary for chondrule formation. It is unlikely that chondrule formation could occur anywhere else in the nebula. The assumptions of aerodynamic drag heating and conductive cooling allow the development of a test particle model to evaluate heating of the dust particles by magnetic reconnection.

At this point it is important for a distinction to be made between fluid temperature and particle temperature. Fluid temperature is the rate of change of the entropy of a system with respect to the total energy (Kubo, 1999; Schrödinger, 1989; Pauli, 1973). That tem-

perature relates the temperature of a fluid to the motions of the individual particles that constitute the fluid. The particle temperature is the physical temperature of the particles themselves. The analogue would be vibrational and rotational states in a molecule. In regards to thermal processing of particles in the protosolar nebula, the particle temperature is the temperature of relevance. Previous works have treated the dust particles as a colloidal suspension. The particles velocity has been treated as a result of friction and gravitational forces. The dusty plasma treatment implies that Coulomb collisions between charged dust particles are possible, even though the particles may never actually physically collide. This added complication requires a test particle simulation to be conducted in order to determine the heating of individual particles from the parameters in the fluid code.

A gas dynamics treatment of the energy transfer to the chondrules requires the determination of the proper flow regime: Continuum gas dynamics, slip flow, or free-molecule flow. Inspection of the Knudsen number (K_n) for the particle (ratio of mean free path of the neutral gas to the scale size of the particle) places K_n between 20 and 20,000,000. This is clearly well within the regime of a free-molecule flow treatment of the problem ($K_n \geq 10$) (Truitt, 1960). The heating of a test dust particle may then be calculated via

$$mc \left(\frac{dT_{dust}}{dt} \right) = \frac{\pi}{2} \alpha r_{dust}^2 \rho_{gas} v^3 - mc C_{cool} (T_{dust} - T_o) \tag{2.51}$$

where $m, c, T_{dust}, \alpha, r_{dust}, \rho_{gas}, v, C_{cool}$, and T_0 are the dust mass, dust specific heat, dust particle temperature, accommodation coefficient, dust radius, neutral gas density, relative velocity, cooling constant, and effective nebular temperature respectively. The first term to the right of the equal sign is the drag heating term (dust-neutral collisional heating). The second term on the right is the conductive cooling term. The values for these parameters are noted in Table 2.4.

Inclusion of test particles in the code is accomplished through book-keeping of the particle locations. The particles are propagated through the simulation box via the dust fluid velocity. An appropriate assumption due to the massive nature of the dust particles. It is unlikely that an individual dust particle will have a velocity significantly greater than the bulk fluid velocity of the dust fluid. Velocity is determined through an average of the 8 grid points that form the vertices of a box containing the particle at its current location

Table 2.4. Parameters for test particle heating simulation. Note that the cooling coefficient C_{cool} is calculated assuming a 1000 $[K]$ temperature drop in 3600 $[s]$, in agreement with the chondrule mineral record.

c	=	695-762	$[\frac{J}{kgK}]$	(Wasson, 1974)
h	=	1.5-2.4	$[\frac{J}{smK}]$	(Wasson, 1974)
α	=	.5		(Wood, 1984)
ρ_{dust}	=	3300	$[\frac{kg}{m^3}]$	(Desch and H. C. Connolly, 2002)
r_{dust}	=	$1-.00001$	$[mm]$	
C_{cool}	=	~ 0.00191		
T_0	=	500	$[K]$	(Hewins and Radomsky, 1990).

(test-particle in cell). As the particles move the previously noted temperature equation is evaluated (Eqn. 2.51). In this fashion the temperatures of the test particles may be evaluated at each time step. The particles are iterated for 10 sub-time steps for each fluid simulation time step. The magnitude of aerodynamic heating may be evaluated directly from the fluid code. This allows identification of heating regions in the reconnection event.

It is important to note that in order to simplify the implementation of the test particle code, values from the fluid code (density, velocity, time, etc.) are multiplied by their normalizations. This allows direct computation of the temperature. The large difference in the ion-neutral and dust-neutral collision frequencies (along with the other collision frequencies being much lower than these) has an important consequence on heating. The ions couple well to the neutrals while the dust is in essence free to move through the neutrals. An essential detail in regards to the effectiveness of the aerodynamic drag heating. The coupling is explored in more detail (with regards to steady state reconnection) in the next section.

The test-particle subcode allows an evaluation of dust particle heating in the protosolar nebula due to aerodynamics effects in the free-molecular flow regime. Particle propagation is accomplished through the assumption of particle motion at fluid bulk flow velocities. Allowing for both a simple update of particle location and calculation of heating. Conductive cooling is included in order to consistently treat the problem of chondrule formation. This cooling is a parameterization of the inferred cooling rates from the mineral

record. The test-particle code allows one to asses the role of magnetic reconnection on dust particle heating and thus its role in chondrule formation.

2.4.1 Reconnection Rate and Chondrule Heating

A relationship between reconnection rate and chondrule heating may now be derived. In this derivation, it shall be assumed that the large ion-neutral collision frequency of the protosolar nebula, couples the ion and neutrals. Thus their velocities may be treated as approximately equivalent ($\vec{v}_n \sim \vec{v}_i$). Ignoring the pressure term, electron velocity, and ion-electron collisional term the electric field (Eqn. 2.50) may be written

$$\vec{E} = -\frac{\vec{v}_i \times \vec{B}}{c} + \frac{m_i}{e} \mathsf{v}_{id} (\vec{v}_i - \vec{v}_d).$$ (2.52)

Here the first term is the advective term and the second is the diffusive term due to ion-dust collisions. The electric field at the X-line is used as a measure of the reconnection rate. However, the X-Line is a stagnation point for the reconnective flow, so the advective term drops out leaving

$$\vec{E} = \frac{m_i}{e} \mathsf{v}_{id} (\vec{v}_i - \vec{v}_d).$$ (2.53)

The well coupled nature of the ions and neutrals allows for the substitutions of their velocities, allowing one to write

$$\vec{v}_n - \vec{v}_d = \frac{e\vec{E}}{m_i \mathsf{v}_{id}}.$$ (2.54)

Allowing the aerodynamic heating of a dust particle to be written as

$$m_d c_d \frac{dT_d}{dt} = \frac{\pi}{2} \alpha r_d^2 \rho_n |\vec{v}_d - \vec{v}_n|^3 = \frac{\pi}{2} \alpha r_d^2 \rho_n \left| \frac{e\vec{E}}{m_i \mathsf{v}_{id}} \right|^3.$$ (2.55)

A relationship between the reconnection rate (X-line electric field) and the particle temperature due to aerodynamic heating can now be written

$$\frac{dT_d}{dt} = \frac{\pi \alpha r_d^2 \rho_n e^3}{2 c_d m_d m_i^3 \mathsf{v}_{id}^3} \left| \vec{E} \right|^3.$$ (2.56)

For values (Table 1.2) representative of the protosolar nebula, and a heating rates around 5000 K/hr, electric fields as low as 1.0×10^{-11} N/C could heat the dust. This analysis neglects the effects of radiative cooling which (if present), could significantly raise the

reconnection rate (electric field) required for chondrule formation. A steady-state has also been assumed for the reconnection process, which may or may not be achievable. Note the difficulty in achieving an 'equilibrium' Harris profile in Section 2.3.1. Clearly these complications warrant the simulations conducted in this work.

The calculation of the reconnection rate, in the code, is handled by calculating the maximum value of the parallel electric field integrated along a field line.

$$Rate = | \int E_{\parallel} ds|_{max} \qquad (2.57)$$

The code outputs the electric and magnetic fields every 200 time steps. A line of points (on the grid) corresponding to $(x,z) = (0,0)$ and $(y,z) = (0,0)$ are chosen as sampling points for the magnetic field. The magnetic field is then normalized and the trajectories along the field lines are back calculated in increments of 0.1. The value of the magnetic field at a given location is based on an average of the 8 neighboring grid-points (a test particle in cell method). Having reached the simulation boundaries the integrals of the parallel electric field may then be calculated along the field lines. Once calculated the maximum integral is taken as the reconnection rate. For technical accuracy no field line with length larger than twice the diagonal length of the simulation box is considered and no integral is allowed to iterate for longer than 1000 steps.

Chapter 3

Results

Simulations of magnetic reconnection in the dusty plasma of the protosolar nebula show supersonic dust outflows over extended regions, capable of heating dust particles to chondrule forming temperatures ($1200 - 1500[K]$). A ballistic relaxation technique is employed to find a suitable pressure profile for a dusty Harris-like current sheet. Magnetic reconnection is explored with comparisons made between collisional and explicit resistive terms. Attention is paid to identifying flow regimes capable of chondrule formation. Test particle simulations show that individual dust particles are heated on timescales and to temperatures relevant to chondrule formation in the protosolar nebula.

3.1 The Current Sheet Configuration

The simulation begins with a Harris-like current sheet configuration. In the depleted electron regime, a Harris-like magnetic field profile is a good choice (Lazerson and Wiechen, 2008). The collisional interaction and multi-fluid nature of the partially ionized dusty plasma of the protosolar nebula prevents this configuration from becoming an equilibrium. The ballistic relaxation technique employed attempts to find an equilibrium by setting the kinetic energy of the system to zero at maximums in the net kinetic energy. Emphasis is placed on minimizing the kinetic energy and force norm (measure of the unbalanced forces in the system). The resulting configuration is a good approximation of a relaxed current sheet. The magnetic configuration is maintained through suppression of the pressure, collision, and resistive terms in the induction equation. The result is a current sheet configuration that closely resembles the Harris sheet.

The initial condition is chosen so as to minimize heating and thermalization effects while attempting to balance magnetic and fluid pressures. A Harris-like magnetic field profile is chosen where ion pressure balances the magnetic pressure. The profiles for the various parameters can be seen in Figure 3.1. The fluid pressure force ($-\nabla p$) is chosen larger than the magnetic pressure force ($\vec{j} \times \vec{B}$). Non-equilibrium forces are thus preconditioned to be away from the current sheet. A pinching of the current sheet which drives the configuration away from a Harris-like solution is prevented. The force imbalance is an advantageous choice for the ballistic relaxation method.
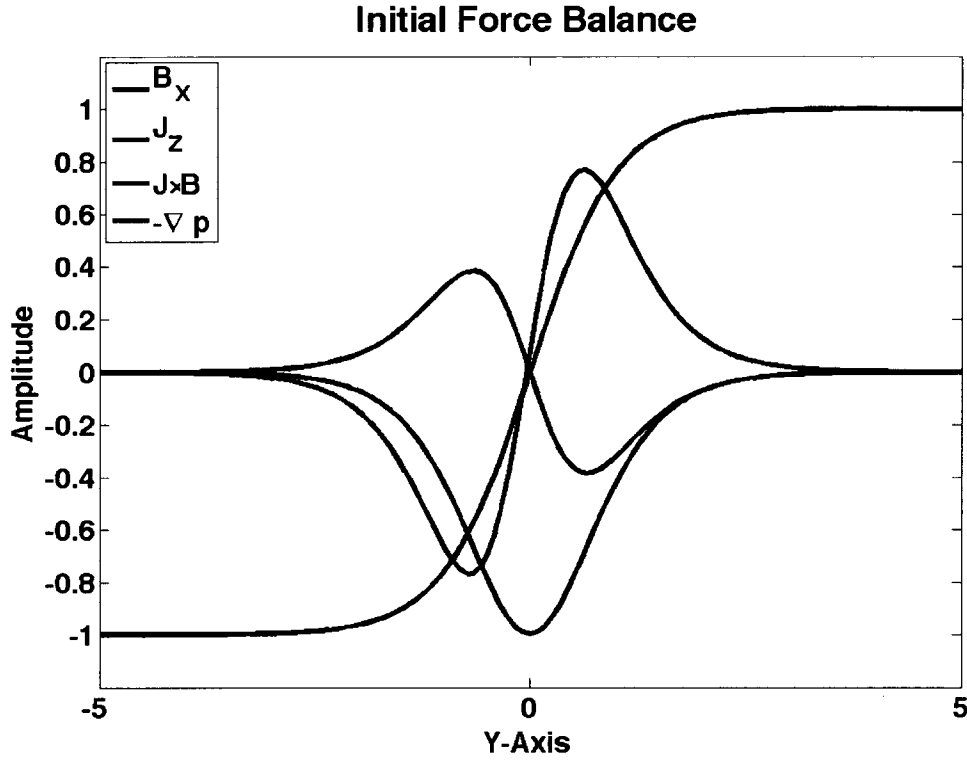
Initial Force Balance

Figure 3.1. Initial force balance for the current sheet before relaxation. Here the large difference between the pressure force $(-\nabla p)$ and the $\vec{j} \times \vec{B}$ force is clearly evident. The magnetic field profile (red) and current density profile (brown) are plotted for reference. Summation of $\vec{j} \times \vec{B}$ and $-\nabla p$ indicate a net force away from the current sheet.

The ballistic relaxation method is implemented with a temporally varying frictional viscosity (Eqn. 2.46). The system is ballistically relaxed by setting all velocities to zero at maximums in the net kinetic energy (the sum of dust and neutral kinetic energies). The multi-fluid nature of the code calculates ion velocities based upon the dust and electron velocities and the net current density. When a ballistic relaxation is conducted the ion velocity is calculated based on the net current (thus it is not entirely correct to assume that all species velocities are set to zero). Figure 3.2 shows the evolution under ballistic relaxation of kinetic energy and the force norm in the $\hat{y}$ direction (along with the magnetic and internal energies). The invariant directions ($\hat{x}$ and $\hat{z}$) are neglected as energies and force norms in these directions are negligible.
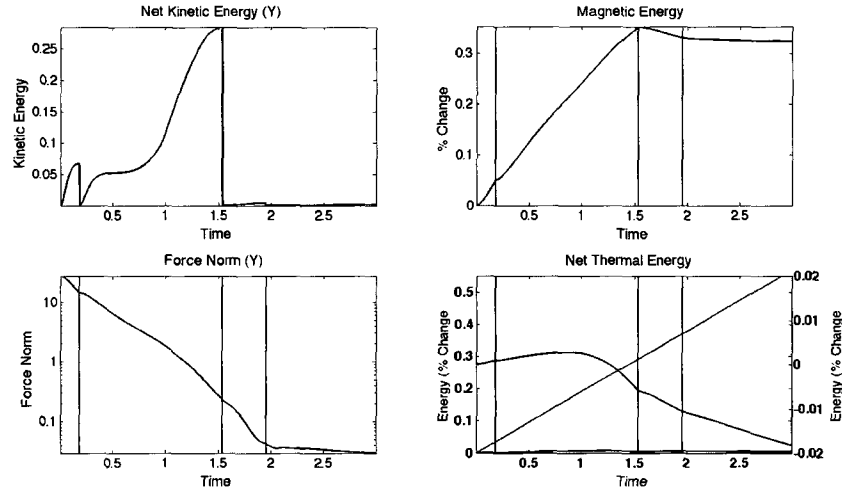
Figure 3.2. Diagnostic plots of the ballistic relaxation. Vertical red lines depict ballistic relaxations. The majority of the kinetic energy is removed from the system within the first two scale times (along with the reduction of the force norm). A less than 0.4% change in magnetic energy indicates preservation of the Harris-like magnetic field profile. The thermal energy plot depicts the ion (red), electron (blue), and neutral (green) energy evolutions associated with the left axis. The thermal energy evolution of the dust (black) is associated with the right axis.

The diagnostic plots shown in Figure 3.2 show the overall evolution of the system throughout the ballistic relaxation. The kinetic energies show 3 distinct structures. The first is a small peak, associated with the imbalance in forces present in the initial condition. After ballistic relaxation the dust kinetic energy shows a slightly smaller peak at around $t = 0.5$. The neutral kinetic energy then begins to quickly rise and results in the almost double-peaked signature present in the kinetic energies (between the first and second relaxation). It is worthwhile to note that the neutral kinetic energy shows a much steeper slope in kinetic energy after $t = 1.0$. The slope can be attributed to the viscosity term having diminished to its asymptotic value. The third peak shows an order of magnitude reduction in the kinetic energies, indicating a relaxed system. The achievement of a relaxed system is corroborated by a significant decrease in the force norm. Within the first two scale times (Alfvén transit times) the force norm has been reduced by four orders of magnitude. The magnetic energy shows very little overall change. This is indicative that the Harris-like

magnetic field profile has been maintained throughout the relaxation. The thermal evolutions show a slight (0.02%) heating of the ions and neutrals with a gradual cooling of the dust ($< 1.0\%$). The thermal behavior of the dust is indicative of a slight decrease in density which can be attributed to the non-equilibrium flows away from the current sheet. The ion and neutrals show a strong coupling due to the large ion-neutral collision frequency. Their gradual (and constant temperature increase) is attributed to the frictional heating in the current sheet. The presence of current sheets in collisional systems results in ohmic heating of both the plasma and neutral gas species. That is to say, heating which can be attributed to the presence of currents. It can now be recognized that through the inclusion of energy equations (containing collisional heating) the force balance achieved by the Harris sheet will only be valid on timescales shorter than the heating timescale. The presence of a current implies a heating source which prevents a true force-free state. A minimum is clearly still achievable. At the end of the ballistic relaxation procedure, the system has achieved a near-equilibrium state in regards to force balance and thermal energy balance.

The ballistic relaxation technique results in force balance between magnetic and plasma pressure forces while allowing the system to come to thermal equilibrium. Figure 3.3 indicates the extent of the changes to the initial profiles. The densities show a slight broadening of the dust and ion profiles, attributed to the nature of our initial force imbalance (away from the current sheet). The magnetic field shows little change. The ion pressure shows a significant reduction in the amplitude of its profile and an slight increase in pressure at the flanks. This is again attributed to the non-equilibrium flows present during the relaxation process. The temperatures of the plasma species show changes in the current sheet region. The dust temperature profile shows heating in the current sheet (directly attributed to the slight rarefaction of the densities and isothermal treatment of the dust). The cooling seen in the current sheet ions can be attributed to the rarefaction of the ions in that region. The neutrals show little change.
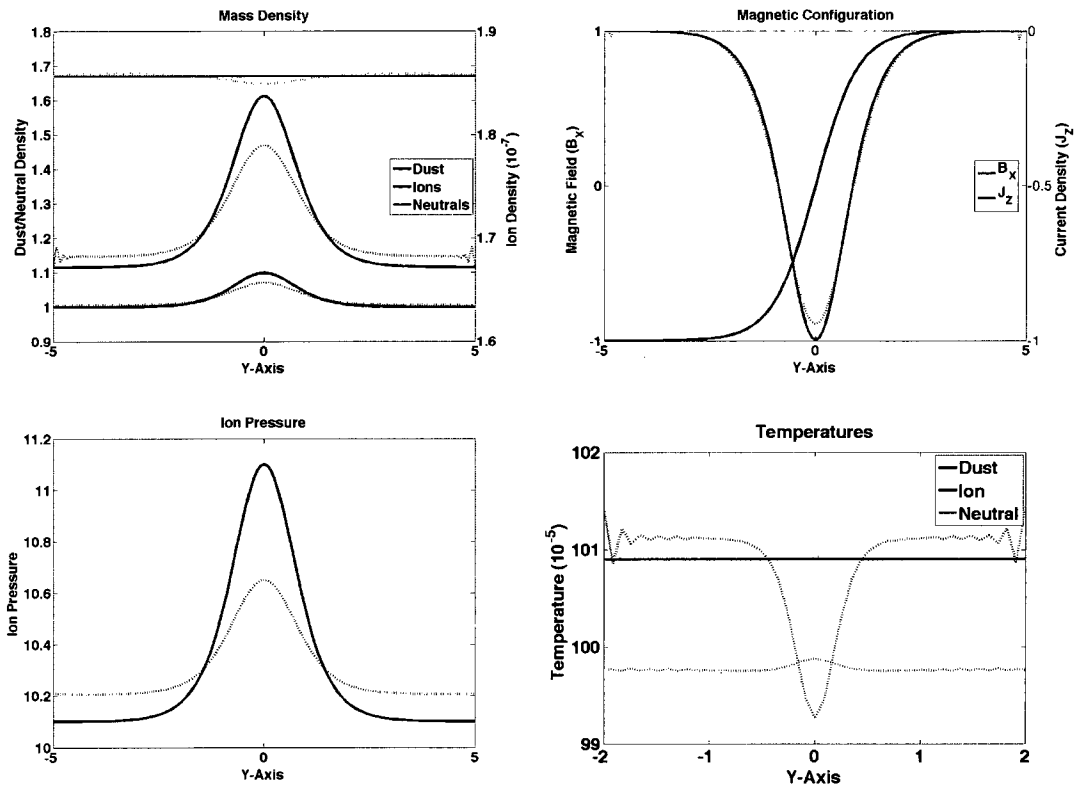
Figure 3.3. Density, pressure, temperature and magnetic field profiles after ballistic relaxation. Values before relaxation are depicted as solid lines. Dashed lines indicate values after relaxation. Most show little change. Densities in the current sheet have decreased due to outward flows. The reduction in ion pressure (with minimum change to the magnetic configuration) is the desired result of the ballistic relaxation process.

The ballistic relaxation technique provides a useful technique by which a near-equilibrium configuration can be found for the dusty Harris-like current sheet. The technique allows for significant reductions in kinetic energies and residual unbalanced forces in the system while allowing a thermal evolution to occur. The resulting configuration may have a velocity perturbation applied which will not be overcome by non-equilibrium forces associated with the initial condition. This allows the study of reconnection to commence.
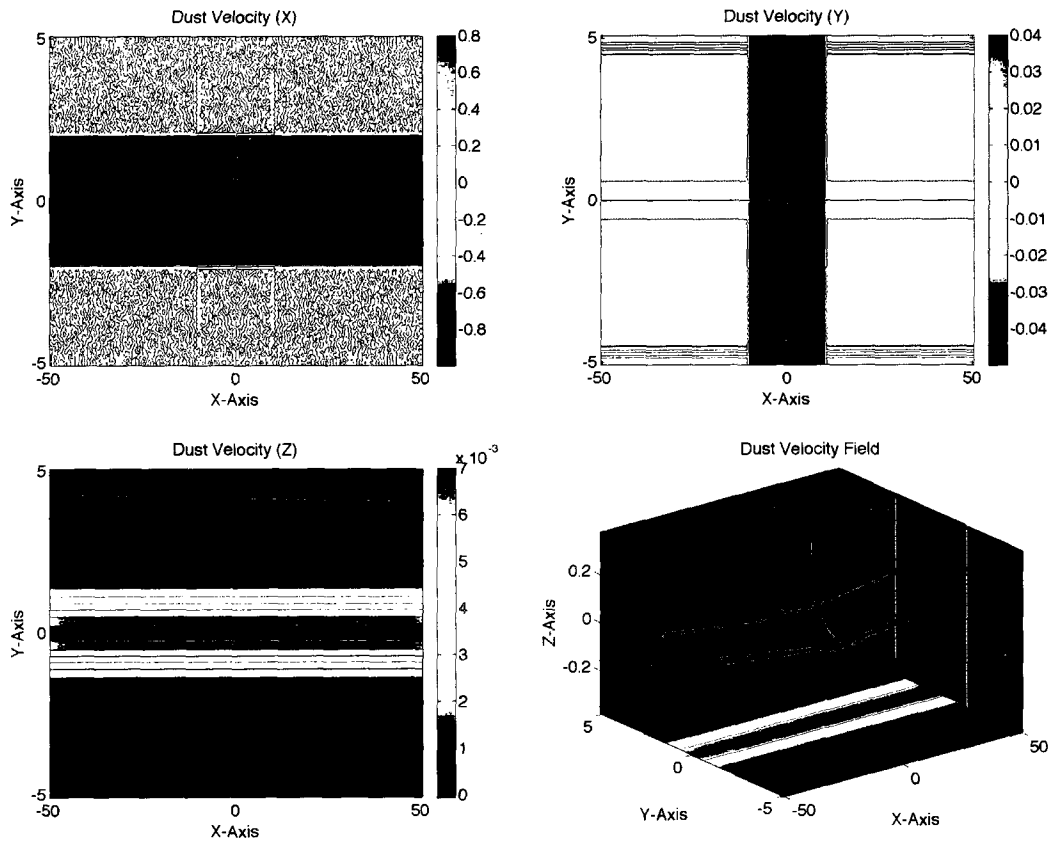
3.2 Magnetic Reconnection: Resistive

Figure 3.4. Dust velocity perturbation. Plots of the components of the dust velocity (v_x, v_y, and v_z) taken in the X-Y cut plane at $z = 0.0$. A streamline plot has been included for clarity. The perturbation is taken to be uniform in the $\hat{z}$ direction.

The process of magnetic reconnection is studied through the application of a velocity perturbation while switching on an explicit resistivity in the induction equation. The velocity perturbation is conducted in a Sweet-Parker like fashion (Figure 3.4). Here an outflow is applied along the current sheet at 80% of the dust Alfvén velocity while a slower 'pinching' inflow is applied to the current sheet. The explicit resistive term is set to $\eta = 0.0369$ which allows comparison between this term and the collisional resistivity (found in the next section). Various quantities are tracked through the surfaces defining the perturbation. The quantities help characterize the state of reconnection, allowing comparisons to

be made with analytic theories. Additionally, these quantities help differentiate between effects associated with the perturbation and those that can be attributed to reconnection. Various quantities are presented in order to gauge the reconnection rate of the system.

The relaxed current sheet is perturbed in a Sweet-Parker like fashion defined by an inflow and outflow region (Figure 3.4). The outflow region is taken to extend in the $\hat{y}$ direction from −1.0 to 1.0. Here the magnitude of the outflow velocity is set equal to 80% of the asymptotic Alfvén velocity (v_x = 0.8 in normalized units). The inflow region extends in the $\hat{x}$ direction from −10.0 to 10.0 pinching the current sheet. The magnitude of the inflow velocity is chosen as v_y = 0.05 so as to minimize compression of the plasma. In the Sweet-Parker model the inflow velocity is chosen as the diffusive velocity (v_{in} = η/l, where l is the scale thickness of the current sheet). The outflow velocity is then chosen from considerations of mass conservation. The choice of inflow velocity made here is similar to the diffusive velocity, however it results in very little compression of the plasma. The large velocities associated with the perturbation are simply chosen to start the reconnective process. Once reconnection occurs, mass and energy transport are examined to characterize reconnection (steadiness of the process).

The perturbed evolution of the reconnecting system can be seen in Figure 3.5. A clear periodicity can be seen in the inflow mass fluxes. The periodic nature of the mass flux is attributed to the stagnation point flow of the perturbation itself. The outflow mass fluxes indicate a smooth transition from perturbation to non-compressive flows. The initial sharp decrease in mass fluxes is associated with momentum transfer between the perturbed plasma species and unperturbed neutrals. There high frequency oscillations are associated with the perturbation and are quickly attenuated. These are associated with the dust neutral collision frequency term (periodicities of ∼ 0.13 scale times). Lower frequency oscillations in the inflow mass fluxes scale well with the ion-neutral collisional term (period of ∼ 3.3 scale times). Explicit calculations of these coefficients can be found in Appendix C. The attenuation of flows in both the inflow and outflow are attributed to momentum transfer with the neutrals (collisional momentum exchange). It is clear that by t = 6.0 the flows have exchanged their momentum with the neutrals and are establishing a rarifying flow. This flow is governed by the dynamics of the reconnecting fields and not the initial perturbation. The inequality in mass fluxes into and out of the reconnection region
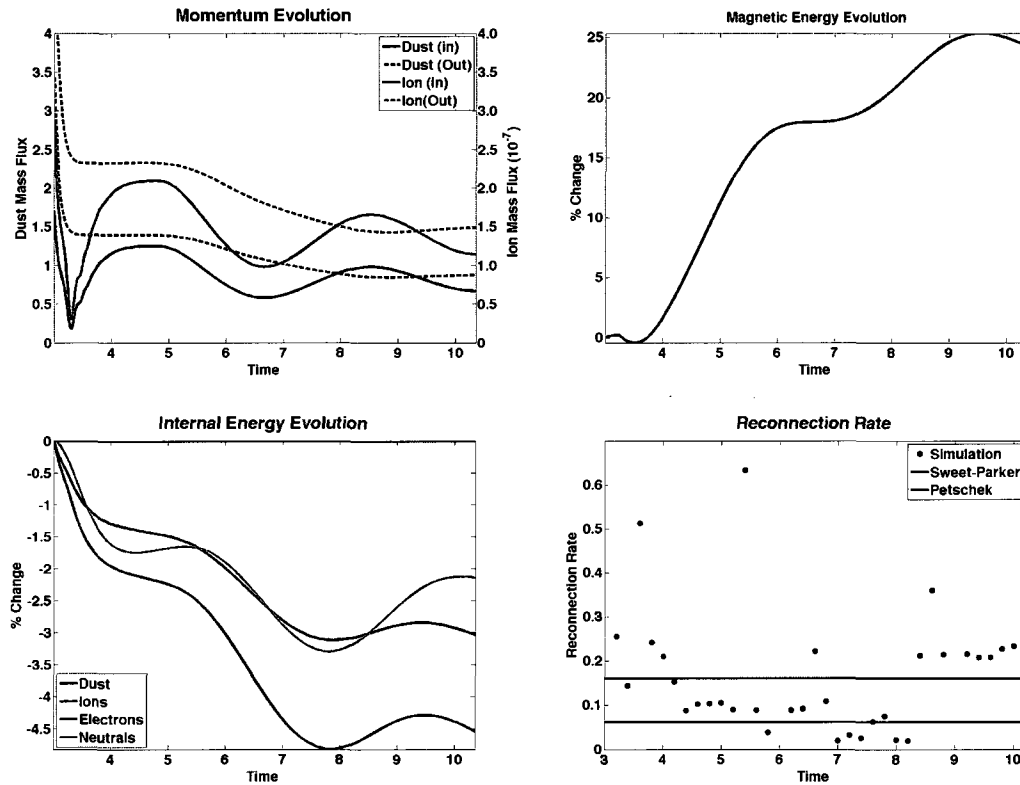
Figure 3.5. Evolution of reconnection for the resistive runs. The net mass fluxes into (at $y = \pm 1.0$) and out of (at $x = \pm 10.0$) the reconnection region for the dust and ions are depicted in the graph on the upper left. Both ions and dust seem to achieve an equilibrium flow which is slightly rarifying ($\dot{m}_{out} > \dot{m}_{in}$) after one scale time (Alfvén transit time). Magnetic energy shows a compression of the field which is consistent with an inflow velocity larger than the diffusive velocity. Internal energy evolutions in this reconnection region indicate only slight changes in internal energy. The net drop in dust, ion and neutral energy is associated with the rarifying flow. This is coroborated by decreases in net mass in the reconnection region (not shown).

is attributed to the compressional treatment of the fluids in the simulation. In addition, assumptions of incompressible flows in analytic models tend to neglect the nature of the current sheet which may have a higher density in the sheet itself than at the flanks. The significant increase in the magnetic energy is associated with compression of the magnetic field (thinning of the current sheet). A steady-state in terms of mass fluxes seems to be achieved in the reconnection region.

The system shows clear signatures of reconnection after the perturbation is applied (Figure 3.6, $t = 9.0$). Examination of the magnetic field profile at the flanks (far from the reconnection region) shows a diffusion of the magnetic field consistent with an explicit diffusive term ($v_{diff} \sim 0.035$). The out of X-Y plane magnetic field (B_z) indicates a twisting of the reconnected field lines. This component of the field has been suppressed in the field line plot for clarity. These signatures are indicators of Hall-like effects (Terasawa, 1983). These are most likely associated with ion-dust decoupling as opposed to the ion-electron decoupling associated with classical reconnection. The dust and ion fluids are clearly beginning to decouple in these regions. Plots of the ion-dust relative velocity shows strong regions of velocity decoupling within 8 scale lengths of the X-line in the outflow region. These dynamics near the X-line are clear indicators of the reconnection process at work and not the initial perturbation. Lower amounts of velocity decoupling can be seen to ~ 23 scale lengths (in agreement with estimates of dust magnetization length scales). The inflow regions shows decoupling between the dust and ions on length scales of ~ 2.5 (in agreement with estimates of the dust skin depth, inertial length scale). The simulations tracks well with our estimates of many plasma and reconnection parameters.

The reconnection rate (Figure 3.5) indicates a rate that varies between the Sweet-Parker and Petschek rates with some excursions, attributed to the granularity of the grid. The initial perturbation has a scale length of $L = 10.0$, which coupled with the asymptotic Alfvén velocity and resistivity, gives a Sweet-Parker reconnection rate of 0.061. The Petschek rate is then calculated as 0.161. The reconnection rates obtained from the simulation tend to fall in the range of these value. Sudden jumps in the reconnection rate can be attributed to the granularity of the grid and the field line integration technique. The initial perturbation results in a large reconnection rate which then decreases to the Petschek rate. The initial decrease in reconnection rate is attributed to the equilibration of plasma and neutral
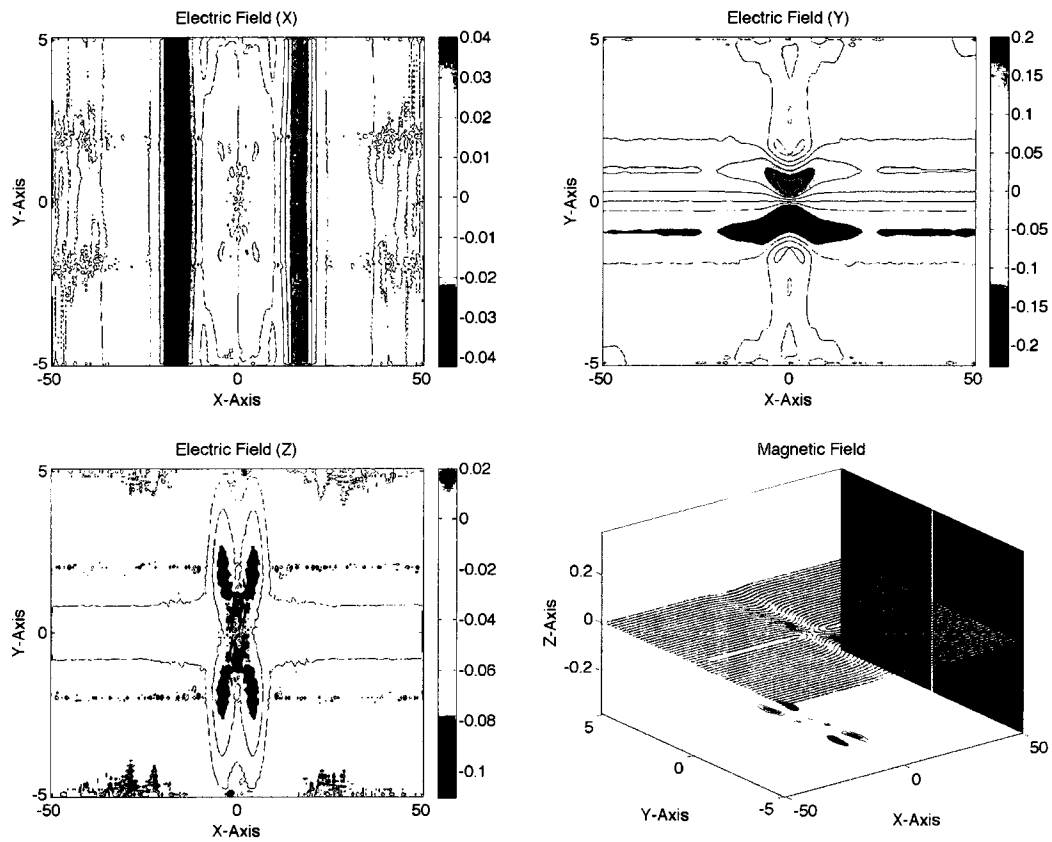
Figure 3.6. Electromagnetic signatures of reconnection for the resistive run ($t = 9.0$). Plots of the components of the electric field (E_x, E_y, and E_z) taken in the X-Y cut plane at $z = 0.0$. The field line plot of the magnetic fields clearly shows a reconnected magnetic field. The walls of the field line plot show contours of magnetic flux through the walls (not normalized to each other, although B_y and B_z indicate similar scaling). Red indicates flux leaving simulations domain. Blue indicates flux into simulation domain. The B_z component has been suppressed in the field lines for clarity.

fluxes. A jump is seen in the reconnection rate between $t = 5$ and $t = 6$. At this time the inflow mass flux is decreasing faster than the outflow flux. There may be a link between flow regime and the reconnection rate. After $t = 8.0$ the flows briefly become compressive, while the reconnection rate jumps again. It should be clear that from $t = 4.0$ onward the system is undergoing reconnection and the effects of the initial perturbation have diminished. The evolving nature of the magnetic reconnection event presented here makes comparison with linear 'steady-state' theories difficult (further discussion is presented in the next chapter).

These simulations can identify possible regions of chondrule formation through examination of the dust-neutral relative flows. The cooling associated with chondrule formation happened on timescales orders of magnitude larger than that of the heating thus allowing us to focus on the heating mechanism. Cooling rates may be inferred from experimental data involving chondrule mineral formation. Heating of the chondrules from dust-netural friction (according to the model in Section 2.4) occurs for dust-neutral velocities as low as 150,000 m/s (0.00003 in normalized simulation units). At $t = 9.0$, dust neutral velocities are still large in the outflow region. These heating regions can be divided into two sections: one within 10 scale lengths and one from 10 to 20 scales lengths. The inner region has dust velocities exceeding the neutral velocities ($\Delta v \sim 0.002$). The outer region has the neutral velocity exceeding the dust velocity ($\Delta v \sim 0.009$). The extent of each region shows a weak scaling with the dust-neutral collisional length scale. The enhancement of the current sheet at the X-line also provides a large dust-neutral velocity ($\Delta v \sim 0.02$). Chondrules in this region will surely be heated, with the possibility of dust evaporation in this region. The connection between reconnection and particle heating is most relevant in the region near the X-line. Approximations can be made that in the X-line region velocities and distances suggest chondrule formation, test particle simulations are required for a true calculation.

Resistive reconnection in a dusty plasma has been shown to produce dust-neutral flows capable of heating dust particles to chondrule formation temperatures. The nature of the reconnection event shows dynamics which indicate many of the assumptions of linear reconnection theories do not apply. Mass fluxes, reconnection rates and pressures indicate a complex picture in which the state of reconnection is constantly evolving despite attempts to perturb the Harris-like configuration in a linear fashion. The multi-fluid nature

of the system is exhibited through Hall-like magnetic field signatures. The reconnection rate varies showing periods of reconnection between the Sweet-Parker and Petschek rates. A test particle simulation is clearly needed to understand the thermal evolution of dust particles and asses the impact of magnetic reconnection on chondrule formation.

3.3 Magnetic Reconnection: Collisional

The multi-fluid nature of this model allows for study of reconnection where explicit collision frequencies are employed in the induction equation (providing the needed non-idealization required for magnetic reconnection). The system is perturbed as in the previous section; with the modification that the explicit resistive term is set to zero and the collisional terms in the induction equation are switched on. Inflow and outflow perturbations are applied to the plasma species. Parameters such as mass flux, internal energy, and reconnection rates are calculated as in the previous section. The magnetic signatures of reconnection are examined. The reconnection rate is compared against linear theories of reconnection. As before, regions of possible chondrule formation are identified through dust-neutral relative velocities. These are the first simulations of magnetic reconnection in a dusty plasma where explicit collisional terms in the induction equation have been considered.

The system is perturbed in the same fashion as the previous section (see Figure 3.4). It is at this point that the collisional terms in the induction equation are switched on. The collision frequencies have an effective resistivity equivalent to that found in the resistive run ($\eta = 0.0369$). Under the assumption of zero electron velocity (and negligible ion-electron collisions) an effective resistitivity can be calculated from the collision frequencies (Eqn. 2.19). The system is then allowed to evolve, allowing reconnection to proceed.

The evolution of the collisional reconnection run can be seen in Figure 3.7. The mass fluxes indicate that the flows reach equilibrium on similar timescales as seen in the resistive run. The equilibration of flows is attributed to momentum exchange between the plasma and neutral fluids. The ion and dust flows through the reconnection region are slightly rarifying and rarely equal (an important assumption made in analytic theories of reconnection). Magnetic energy in the reconnection region is clearly compressed (thinning of the current sheet). The compression is slightly greater than that seen in the resistive
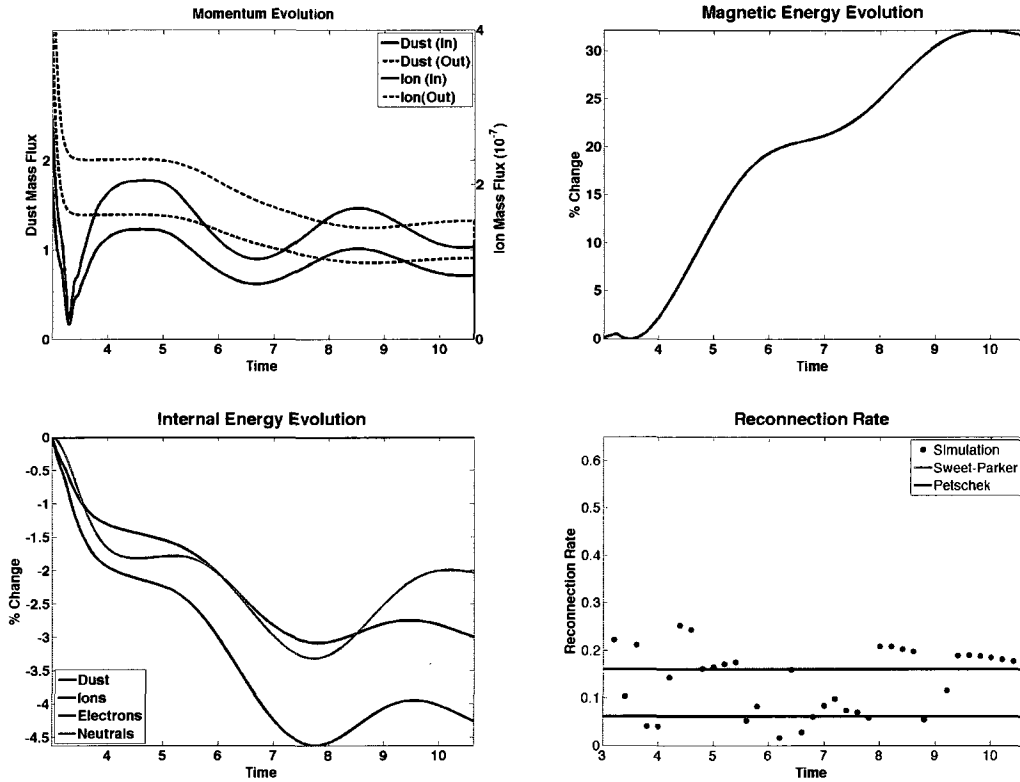
Figure 3.7. Evolution of reconnection for the collisional runs. The net mass fluxes into (at $y = \pm 1.0$) and out of (at $x = \pm 10.0$) the reconnection region for the dust and ions are depicted. Both ions and dust seem to achieve an equilibrium flow which is slightly rarifying ($\dot{m}_{out} > \dot{m}_{in}$) after one scale time (Alfvén transit time). The magnetic energy shows signs of greater compression (indicating less diffusion). Internal energy evolutions in this reconnection region indicate only slight changes in internal energy. The reconnection rate does not posses the large amplitude jumps seen in the resistive run.

runs of the previous section. The enhanced compression of the magnetic field suggests less diffusion of the field (given equal inflow velocities). The internal energy evolution is similar to that as seen in the resistive run. The lower diffusion, despite similar effective resistivities, marks the departure between the resistive and collisional runs.

The magnetic signatures of reconnection for the collisional run at $t = 9.0$ are shown in Figure 3.8. The magnetic field far from the reconnection region shows diffusion consistent with the effective resistivity. Examination of the data indicates that the effective diffusive velocity in the collisional run is $\sim 10\%$ less than that of the resistive run. However, the effective resistivity calculated from the collision frequencies is a function of ion number density which varies across the current sheet. Taking the ion number density profile into account, the effective resistivity drops by $\sim 10\%$ in the current sheet. This explains the slightly lower level of diffusion for the collisional run. It can then be said that the presence of dust in current sheets may lower the effective resistivity of the current sheet through enhancements to the ion number density.

The reconnection rate for the collisional run indicates a larger rate despite similar flow dynamics to that of the resistive run. In general the collisional run shows that the reconnection rate stays higher than the Petschek rate for longer periods of time than the resistive run. The large spikes in the reconnection rate seen in the resistive run are not present. At this time it is difficult to say if this can be attributed to the collisional form of the induction equation or is a function of the field line integration routine. In general, reconnection for both runs includes three regions. The first is an erratic region associated with the perturbation. Both runs then indicate a region of lower reconnection rate. This region is associated with the onset of reconnection as is evident in the enhanced flows in the $\hat{z}$ direction. Then around $t = 8$ the system resumes a 'super-Petschek' rate. Longer runs with greater temporal resolution may be required to resolve this behavior.

The identification of chondrule forming regions is similar to that found in the previous sections for the $\hat{x}$ and $\hat{y}$ components of the dust-neutral relative velocity. A large enhancement in the dust-neutral relative velocity is seen in the $\hat{z}$ direction at the X-line (Figure 3.9). The enhancement is attributed to dust motion in this direction. The enhanced dust velocity can be attributed to the added compression of the magnetic field. It is important to note that the perturbation contained no $\hat{z}$ component. Any dynamics in this direction
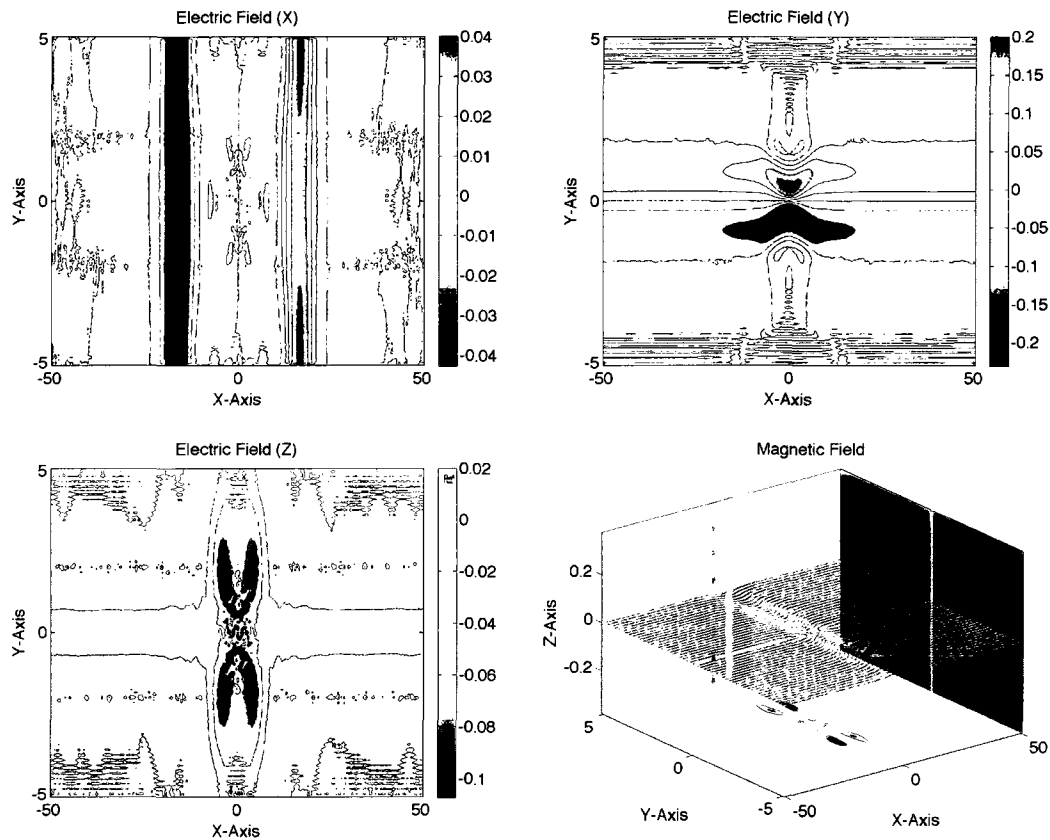
Figure 3.8. Electromagnetic signatures of reconnection for the collisional run ($t = 9.0$). Plots of the components of the electric field (E_x, E_y, and E_z) taken in the X-Y cut plane at $z = 0.0$. The field line plot of the magnetic fields shows a reconnected magnetic field with significant out of plane fields. The walls of the field line plot show contours of magnetic flux through the walls (not normalized to each other). Red indicates flux leaving simulations domain. Blue indicates flux into simulation domain. In comparison with the resistive run (Figure 3.6) the current sheet has undergone similar levels of diffusion. Note that the B_Z component of the magnetic field has been suppressed in the field line plot for clarity.

Figure 3.9. Comparisons between components of the dust-neutral relative velocity for resistive and collisional runs. Resistive runs are on the left and collisional runs on the right. Note that the collisional run shows an enhanced region at the X-line.

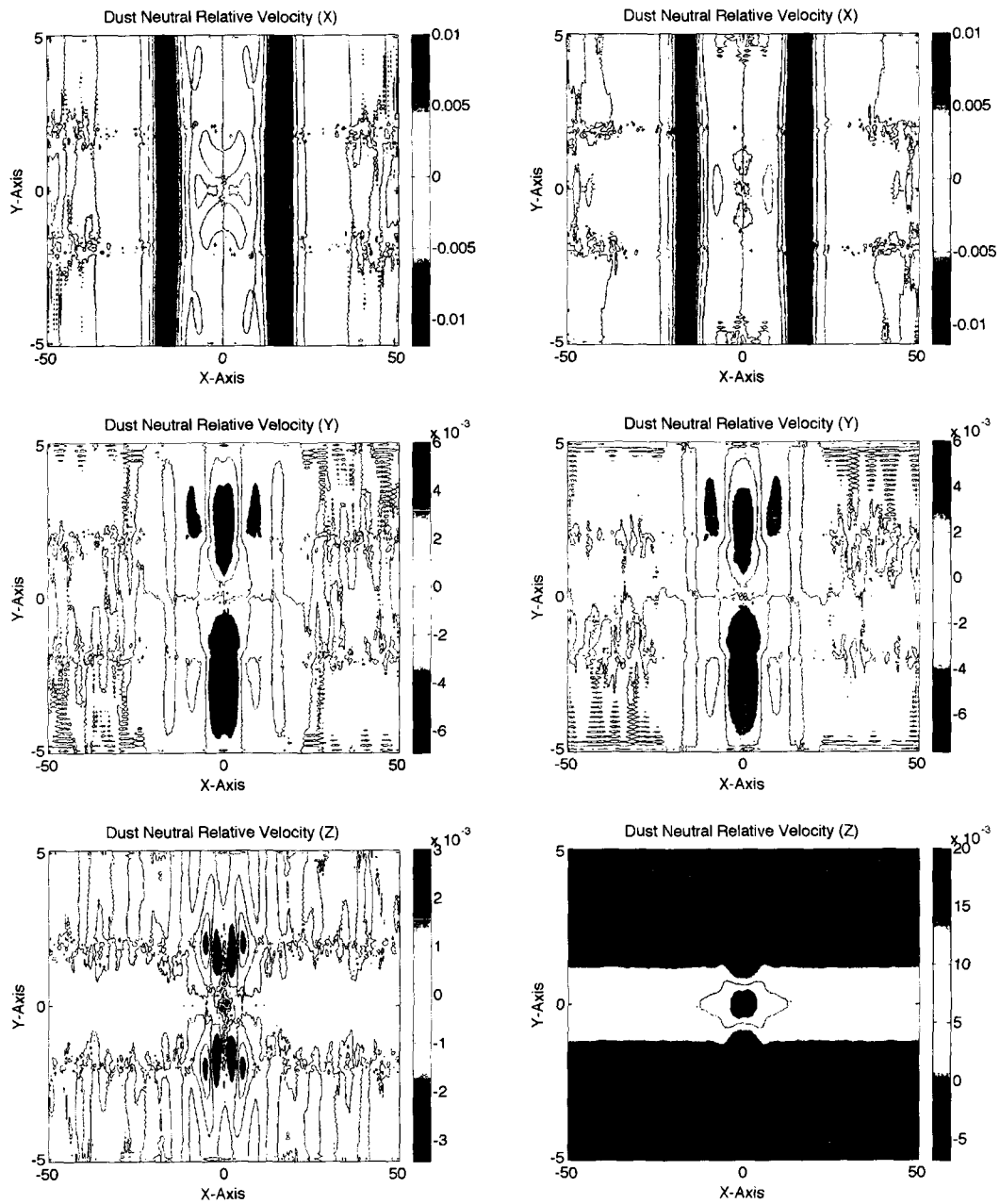can be associated with magnetic reconnection. Thus it is safe to assume that in the reconnection region (near the X-line) particle heating is attributed to reconnection itself and not the perturbation. A test particle treatment of particle heating will be required to better understand the implications of this region on chondrule formation.

The collisional reconnection runs shows similar morphology to that of the resistive run. Key points of difference are a reduced diffusion of the magnetic field and an enhanced region of dust-neutral relative velocity at the X-Line. Similarities between the collisional and resistive run indicate that collisions provide adequate levels of non-ideality for reconnection to proceed. The ion number density dependence of the effective resistivity results in lower diffusion in the current sheet. This suggest that the presence of charged dust may be able to alter behavior of current sheets. Flows capable of heating dust to chondrule forming temperatures are clearly present in both simulations. In the next section, test particle heating is investigated.
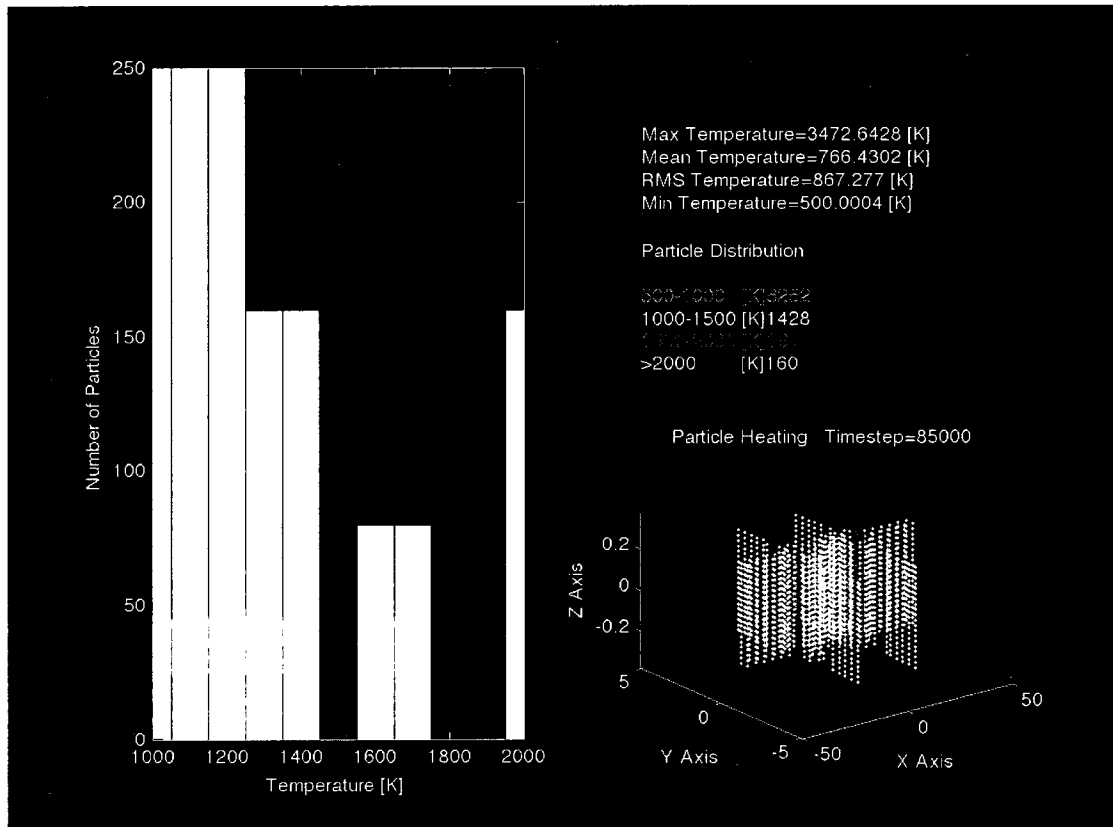
Figure 3.10. Test particle heating code diagnostic output for a collisional run. Statistical data along with particle visualizations are shown. Red and yellow colored particles indicate chondrule forming temperatures have been reached. Particles with temperatures below 1000 [K] have been omitted for clarity.

3.4 Dust Particle Heating

Magnetic reconnection produces outflow velocities on the order of the dust Aflvén velocity ($v = 3 \times 10^6$ m/s), which are capable of heating the dust particles through collisions. Test particle simulations were conducted (Figure 3.10) where the individual temperature and location of test particles were tracked during the reconnection process. Heating in the current sheet is observed due to the anti-parallel flow between dust and neutrals. The presence of such flows is attributed to the large ion-neutral collision frequency and disparate dust length scales (inertial and magnetic) when compared to the ions. Additionally, enhancements of the ion velocities (and thus neutral velocities) at the X-line contributed

to heating in the reconnection region. The effects of the neutral density were evaluated for these runs.

Analytic theories of magnetic reconnection assume a conversion of magnetic energy into thermal and kinetic energy. This suggests that reconnection in a dusty plasma results in a heating of the chondrules via two methods. The first is through local enhancements of neutral gas temperature. Simulations shows localized enhancements of neutral gas temperature around 20%. It is thought that the neutrals provide a warm bath for the dust particles of between $200[K]$ and $500[K]$. Chondrule formation requires peak temperatures between $1200[K]$ and $1700[K]$. A 20% enhancement in neutral temperatures is not sufficient. The second method by which the dust may be heated is through aerodynamic drag.

Theories of reconnection predict outflows on the order of the Alfvén velocity. Simulations conducted here agree with this assessment. As the dust and neutrals develop large relative velocities, aerodynamic heating of the dust occurs. The dust-neutral collision frequency in the protosolar nebula is approximately $v_{dn} = 0.004[s^{-1}]$ (an upper estimate, the actual value may be much lower). The value of the dust-neutral collision frequency implies that the dust and neutrals will equilibrate their velocities on timescales of around 5 minutes. Simulations show regions of extended dust-neutral heating (near the X-line) which would take the dust around 20-30 minutes to transit. Reconnection is responsible for strong accelerations of the dust over extended regions which can result in aerodynamic heating of the dust. The heating duration experienced by chondrules is thought to be of the order of $10 - 20$ minutes. Assuming reconnection produces dust-neutral relative velocities on the order of the Alfvén velocity ($28.2 \times 10^6 [m/s]$) the dust may experience heating of the order $2000 - 5000[K/hr]$. The rate of heating required for chondrule formation falls within this range. The cooling process is known (from experimental data involving chondrule mineral formation) to be much slower on the order of hours to days. This cooling is associated with conduction to a thermal bath as opposed to radiative cooling (which would occur much too quickly). Therefore, it is likely that magnetic reconnection inside the disk of the protosolar nebula results in heating of the dust particles. Reconnection may be occurring elsewhere in the nebula but only the disk provides the necessary thermal environment to explain their formation.

The test particle simulations conducted here use a test particle-in-cell approximation.

Implementation of this test-particle code is straightforward. The test-particle code tracks the location of a given particle. Relevant values for the the particle are extracted from the fluid simulation by averaging the 8 grid points forming a box around the particle. Particles are propagated using the dust fluid velocity. Each particle is iterated for 10 sub-steps for each fluid simulation time step. The test particle code does not begin iteration until $t = 4.0$. This is done in an attempt to avoid any effects due to the initial perturbation (note that only the plasma was perturbed, not the neutral fluid). The 8000 particles used in the simulation were spaced so that they were uniformly spaced in each direction (although not between direction, $\Delta x \neq \Delta y \neq \Delta z$). They were spaced so as to occupying 3/4 of the extent of each axis. This equates to a box centered at the origin which has a volume 40% of the simulation domain. In contrast the reconnection region occupies 8% of the simulation domain (approximately 850 test particles initially reside in the reconnection region).

The resistive and collisional runs were evaluated for various cooling rates. A conductive model was assumed where the particles transfer their heat to a thermal bath (possibly the neutral background) at 500 $[K]$. This is in good agreement with experiments involving the formation of chondrules. As an initial estimate, it was assumed that the cooling time for the particles from 1500 $[K]$ to 500 $[K]$ was one day. This did not provide enough cooling and the particles quickly overheated. Runs were then conducted with cooling timescales of 1 $[hr]$ and 2 $[hrs]$. These runs indicate requisite heating of the dust to explain chondrule formation.

The simulations conducted with cooling timescales of one day do provide some insight into the heating of dust particles (Figure 3.11). In both resistive and collisional runs the particles show signs of strong heating in the inflow region. The heating in the inflow region is noteworthy as both these plots were taken toward the end of the simulation run. It was seen that perviously cool particles were heated. This cannot be attributed to the initial perturbation as the particles would have been heated from the beginning of the simulation. Additionally, these regions saw a sudden increase in dust-neutral velocities not associated with perturbation. The dust-neutral collision frequency in normalized units is 7.46, indicating that the dust and neutrals should equilibrate velocities on the order of $\Delta t = .134$ (or 240 $[s]$). Given the initial inflow velocity of $v = 0.05$ in normalized units, we would expect to see the dust and neutrals to equilibrate their flows on length scales of $L =$
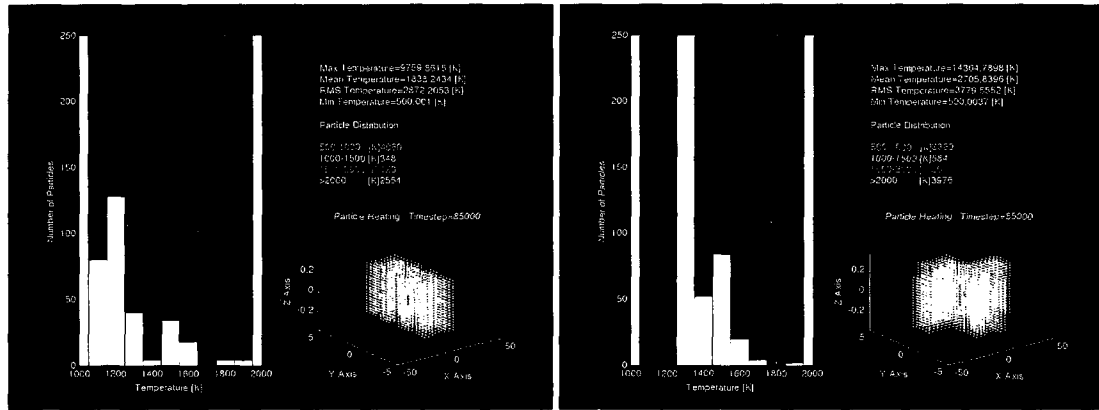
Figure 3.11. Test particle visualization for cooling rates of one day. Resistive (left) and collisional (right) runs both show overheating of the dust. The collisional run shows signs of heating in the outflow region, the resistive does not.

0.007 for localized sources of acceleration (which is below the grid scale). The explanation for the inflow region heating is attributed to the choice of collision frequency (explained in the next paragraph). The outflow regions show drastic differences in heating between collisional and resistive runs (which are seen across the cooling rates). The collisional runs show signs of heating in the outflow direction (in the reconnection region) while the resistive runs do not. It can now be said that the while the choice of resistive model does not have a large impact on the diffusive property of reconnection it does have large implications for the calculation of species velocities and heating properties.

The inflow regions show unexpectedly strong signs of heating. The explanation for this can be seen in figure 3.9 of the previous section. The flows in the $\hat{y}$ direction indicate that the neutrals are reaching higher inflow velocities (in the reconnection region, approaching the X-line) than that of the dust. These flows are on the order of 10% in the initial inflow velocity ($v_{in} = 0.05$). Here the neutrals are coupled to the ions and dust through the collision frequencies. From our reconnection diagnostics it was clear that the momentum exchange between plasma and neutral species occurred on timescales relevant to these collisional processes. The difference between the velocities can be attributed to pressure forces. As the dust (along with the ions) is pulled into the reconnection region through the imbalance between magnetic and plasma pressures (due to reconnection) the neutrals

are accelerated. However, the suppression of the neutral pressure force (coupled with the assumption of uniform neutral pressure across the current sheet) provides no deceleration mechanism for the neutrals. The neutrals are attempting to achieve a free laminar flow (possibly stagnation point flow) , while the dust must interact with the ion pressure, dust pressure, and magnetic pressure forces which are driving it. Inclusion of the neutral pressure profile would require knowledge of the formation process of the current sheet and is beyond the scope of this work. It is expected that inclusion of a neutral pressure force in the neutral equation of motion will lower the dust-neutral relative velocity in this region.
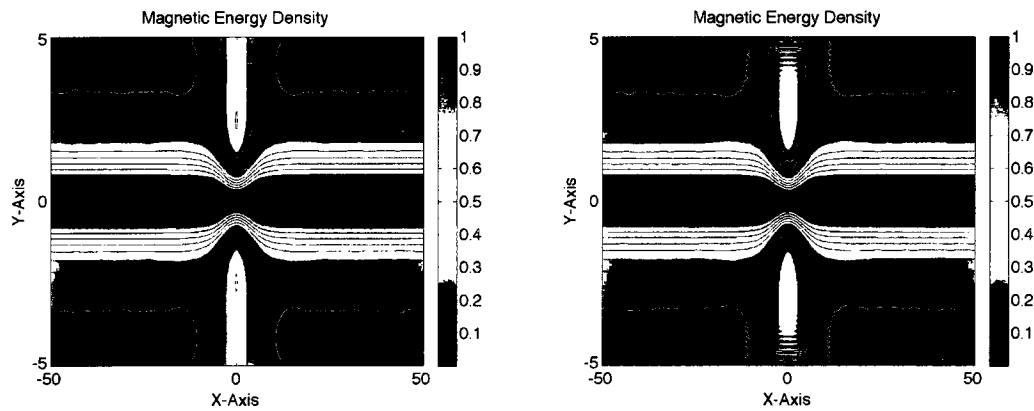
Figure 3.12. Comparison of magnetic energy between resistive (left) and collisional (right) runs ($t = 9.0$). Note the similar asymptotic magnetic field structure between the runs. The collisional run shows signs of oscillation, attributed to the lack of an explicit diffusive term. We also note the presence of grid scale oscillations present in the inflow boundary for the collisional run.

The reconnection region in the outflow direction indicates drastic differences between collisional and resistive runs. Here the resistive runs show no signs of significant heating, while heating is clearly occurring in the collisional runs. The plots of dust-neutral flow in the $\hat{z}$ direction clearly attribute this to stronger flows in the current sheet for the collisional runs (Figure 3.9 of the previous section). It should be noted that the velocities indicate that the neutrals are flowing in the negative $\hat{z}$ direction. As the only parameter that has changed between these runs is the form of resistivity, the differences in flow characteristic must be attributed to differences in magnetic field structure (magnetic energy). Figure 3.12 indicates that the magnetic energy in the reconnection region exhibits more drastic fea-

tures. Enhanced gradients of the magnetic field can result in greater ion flow in the current sheet. The strong coupling between ions and neutrals thus results in dust-neutral relative flows. The association of this heating with velocities in the $\hat{z}$ direction is a clear indication that heating of these particles is due to reconnection and not the initial perturbation.

Simulations were conducted with cooling rates of 1 [hr] and 2 [hr] which produced dust particle temperature profiles capable of chondrule formation. The regions of heating were equivalent to those mentioned in the previous example. Temporal evolutions for each run can be seen in figure 3.13. It is clear in each example that particles can be heated on time scales relevant to chondrule formation (~ 30 [min]). In these plots the particles were binned by peak temperature in order to place emphasis on particles which were heated to relevant temperatures and did not experience temperatures which would be too strong to explain chondrule formation. In each example most of the particles experience heating at around 180 [min] into the simulation (this equates to $t = 6$ in normalized units) reaching peak temperatures at around 210 [min] ($t = 7$ in normalized units). This equates to periods when the inflow mass flux is at a local minimum. The striations of the data are a topological artifact of the particle numbering scheme. Particles heated early on cannot be solely attributed to the reconnective process. This is not a great constraint as the majority of particles experience heating well after the perturbation has been applied. This again enforces the notion that these particles are being heated by reconnection dynamics and not those of the initial perturbation. What is interesting to note is that the majority of particles in each simulation are heated to chondrule forming temperatures at around the same time. The diagnostic outputs of particles temperatures seem to localize this to the inflow regions.

Two other heating groups can be extracted from the graphical depiction in Figure 3.13. First is a group that appears to heat shortly after the test particle code is turned on. These particles heat in a short timespan and then cool off on the order of the cooling timescale for the relevant run. These particles are most likely a hysteresis effect (system memory of the initial perturbation, unequilibrated flows) as a result of the initial perturbation (as already mentioned). The second group is a group that appears to being heating toward the end of the simulation (present only in the 2hr runs). These occur as the simulation is again entering into a domain where the inflow mass flux (in the reconnection region) is again entering a local minimum. The extended regions of 'warm' particles seen in the two hour
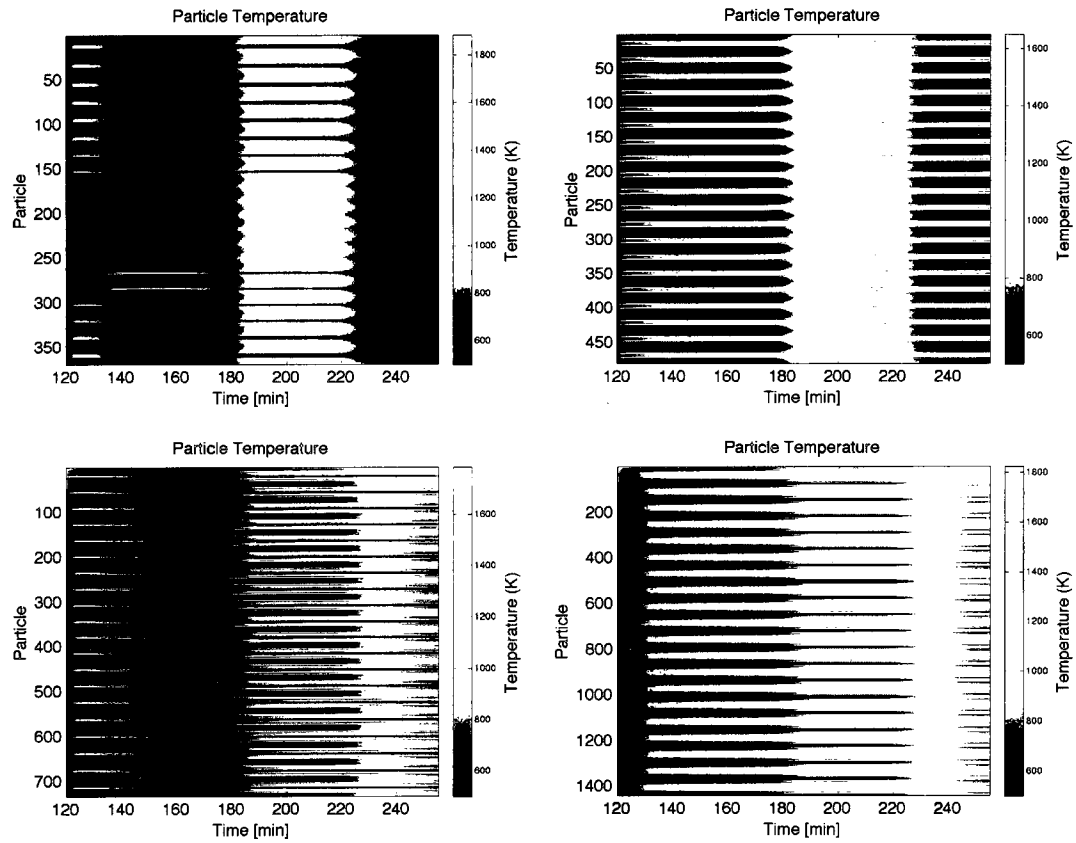
Figure 3.13. Test particle thermal evolutions for one and two hour cooling rates. The one hour cooling rates are on top the two hour rates are on the bottom. The resistive runs are on the left the collisional runs on the right. Indicated are the thermal evolutions for particles reaching peak temperatures over 1200 [K] but less than 1900 [K]. Striation are a topological effect as not all particles heat in the same place at the same time. The y axis is simply an index for each particle.

cooling collisional run (lower right) are indicative of the heating in the outflow region.

It has been shown that magnetic reconnection can produce a thermal history for particles, similar to that found for chondrule, through a test particle simulation. Differences between collisional runs and resistive in the outflow regions are noted. Heating in the inflow region is correlated with oscillations in the inflow plasma mass fluxes. As the dust inflow velocity decreases the neutrals overtake the dust. It is clear that this can be attributed to the perturbation. It is worth noting that the author has studied the form of the perturbation itself and found that despite choice of perturbation the mass flux profiles exhibited here are stereotypical of this type of reconnective mode. In light of this, these simulations should help forward magnetic reconnection in a dusty plasma as a chondrule heating mechanism.

Chapter 4

Discussion and Summary

Three major goals were met through these simulations. First, a dusty multi-fluid current sheet configuration was achieved through a ballistic relaxation technique. The relaxed current sheet configuration allowed for the first self-consistent three dimensional simulations of magnetic reconnection in a dusty plasma. Second, simulations of magnetic reconnection examined both resistive and collisional forms of the induction equation. Finally, the notion of chondrule formation via magnetic reconnection in a dusty plasma was investigated. Here high dust-neutral relative velocities give rise to aerodynamic heating during magnetic reconnection, as evaluated through a test particle (particle in cell) simulation.

Simulations conducted with the DENISIS code show that reconnection in a dusty plasma can produce strong dust-neutral relative velocities. In the context of the protosolar nebula, these flows produce collisional heating of the dust particles that are in agreement with accepted heating rates and peak temperatures associated with chondrule formation. Magnetic reconnection has thus been shown to be a relevant mechanism for chondrule formation. A discussion of these results fall into three categories: the current sheet, magnetic reconnection in a dusty plasma, and heating of dust particles by neutral collisions.

4.1 The Current Sheet Configuration

A ballistic relaxation technique was employed to help determine the equipartition of pressure forces between the fluids and allow thermal relaxation of the current sheet configuration. A Harris-like magnetic field profile was chosen as an initial condition as it provided a good abstraction to current sheets that may be found in the protosolar nebula. The form of the equations integrated by the DENISIS equation coupled with their collisional nature made a true analytic equilibrium inaccessible. The ballistic relaxation technique employed allowed the current sheet to achieve an approximate force balance (indicated by a significant reduction in the force norm). The system was also able to thermally relax. The collisional nature of the system results in a constant heating in the current sheet (similar to ohmic heating found in MHD simulations). The heating prevents a true equilibrium from being achieved. Still a relaxed configuration is achieved which allows the application of a reconnective perturbation.

The Harris-like magnetic field configuration is based on relevant parameters for the protosolar nebula and chondrule formation. The normalized magnetic field (relevant to chondrule formation) results in a large plasma pressure normalization. Coupled with the normalized number density, the normalized temperature becomes very large. These large values present a difficulty, as the assumed temperature for the nebula was relatively low by comparison. The decision was made to choose pressures which would allow both force balance between the magnetic field and plasma species while also providing a near thermal equilibrium for all species. The resulting large neutral pressure was treated through a neglect of the neutral pressure force in the neutral momentum equation. The neglect of the neutral pressure force (while not trivial) can be justified through the large ion-neutral collision frequency (in essence coupling the two fluids) and low neutral beta (ratio of neutral pressure to magnetic pressure). Here it is argued that heating is attributed to particle flow characteristics through the neutrals and not directly to neutral temperature increases. Neutral pressure forces will not be significant unless much larger neutral temperatures are assumed. More sophisticated simulations should be conducted in the future to address the issue of neutral dynamics. The ballistic relaxation technique provided a means to sort out the near-equilibrium configuration necessary to apply a reconnective perturbation.

In the context of the protosolar nebula, current sheet formation is attributed to turbulent effects in the nebula itself. These non-linear effects includes an array of shear-flow (magnetorotational and Kelvin-Helmholtz) and gravitational (Rayleigh-Taylor) instabilities. A Harris-like kinetic description of a current sheet would predict thicknesses on the order of a few Debye lengths. While this may place a minimum limit on current sheet thicknesses, it is expected that typical current sheets would be much thicker in the nebula. The protosolar nebula has scale sizes on the orders of 100's to 1000's of Astronomical Units (approximately 150 million kilometers per Au). The current sheet thickness in the simulation was on the order of 2 million kilometers. Simulations of the entire nebula would be necessary to begin to estimate 'realistic' scale thicknesses for current sheet formation. To date these are lacking. Still, the simulations conducted here are within the range of acceptable scale sizes for the protosolar nebula.

4.2 Magnetic Reconnection

The first three dimensional multi-fluid simulations of magnetic reconnection in a dusty plasma were conducted. These simulations focused on achieving a reconnecting magnetic field through a perturbation to the velocities. This limits discussion to steady-state reconnective models and places no emphasis on the destabilization of the current sheet configuration. Examinations of the both the resistive and collisional forms of the induction equation were preformed. For similar resistivities different behaviors were observed. The resistive runs behaved in a diffusive nature, similar to what has been seen in the majority of MHD and eMHD simulations. Here the resistivity acts as a diffusivity allowing both reconnection and diffusion of the current sheet. The collisional run also indicated signs of reconnection with similar diffusive behavior. It is important to note that despite assumptions of constant collision frequencies, the effective diffusivity showed signs of variation. The variation in diffusivity was attributed to its dependence on the ion number density (which varies across the current sheet). Heating of the neutrals was small and localized to enhancements in the current sheet. It is unlikely that chondrule formation can be explained by local enhancements to neutral temperatures. Large dust-neutral relative velocities do offer an accepted form of chondrule heating through aerodynamic drag forces. Regions of dust-neutral relative flows as high as $564\ km/s$ are indicated by the simulations in regions near the X-line. These flows are large enough to produce the required aerodynamic drag heating for chondrule formation. The presence of these strong flows coupled with the high Kneudsen number motived test particle heating studies.

4.3 Chondrule Formation

Magnetic reconnection in the dusty plasma of the protosolar nebula is capable of forming chondrules through acceleration of the various fluid components in the reconnection region. Simulations of magnetic reconnection in a dusty plasma do not indicate a sufficient amount of fluid heating in order to explain chondrule formation. It is unlikely that an enhancement of neutral gas temperature could heat precursor dust to its melting point to form chondrules. High velocity outflows and enhanced regions of the current sheet indicate that heating of dust particles can occur through aerodynamic drag between dust particles and neutrals. These regions are located in near the X-line and heating flows are

often associated with the unperturbed direction ($\hat{z}$). This lends credibility to the notion that reconnection and not the initial perturbation is responsible for chondrule formation. Test particle simulations confirm this hypothesis.

A question also remains regarding the amount of bulk material processed by magnetic reconnection in the protosolar nebula. The answer to this question is coupled to the question of current sheet formation in the protosolar nebula. Clearly the timescales on which chondrules form are much smaller than that of nebular evolution. Even a process localized to small regions of the nebula could process a significant amount of the material in the nebula over these long timescales (billions of years). Simulations of the global dynamics of the protosolar nebula must be conducted to better understand the formation process of current sheets. This will constrain the location of reconnection sites and the scale lengths of such events.

4.4 Concluding Remarks

The first self-consistent simulations of magnetic reconnection in a dusty plasma and the first self-consistent model of chondrule heating through magnetic reconnection have been presented. The following was indicated by the simulations:

- Magnetic reconnection in a dusty plasma does not sufficiently heat the neutral fluid

- Magnetic reconnection accelerates the dust to Alfvénic velocities.

- The accelerated dust is aerodynamically heated to chondrule forming temperatures in and near the reconnection region.

- Heating of the dust particles occurs on timescales relevant to chondrule formation.

- Multiple heating events are seen for individual particles.

Magnetic reconnection in the dusty protosolar nebula will result in heating of the particles through acceleration and thus explain chondrule formation.

This investigation examined reconnection through an idealized model of the reconnection event in a protosolar nebula. Stereotypical parameters were chosen for the nebula and reconnection event. These parameters were a combination of reasonable parameters

for the protosolar nebula and numerically tractable values for the DENISIS code. A Harris-like current sheet configuration provided an initial condition which allowed the study of reconnection without a-priori knowledge of the current sheet formation mechanism. It was assumed a great number of instabilities present in the nebula could be responsible for current sheet formation. A test-particle model of dust heating gauged reconnection as a chondrule forming mechanism. A conductive form of cooling, appropriate to chondrule formation data, was employed. This was done as a detailed thermal model of the nebula has yet to be presented (global approximation do exist). It is assumed that in order for reconnection to produce chondrules, the event must occur in a thermal bath where radiative heat transfer is negligible (inside the nebular disk). These assumptions allowed for an investigation to be conducted into magnetic reconnection in a dusty plasma as a chondrule formation mechanism.

The simulations presented here were conducted within the framework of various assumptions, some attributed to the nature of dusty plasmas and others concessions to the numerical tractability of the code. The assumption of inertialess ion and electron species is mitigated through careful choice of spatial and temporal scales. Care was taken to keep these scale lengths relevant to process under investigation. Neglect of the neutral pressure force was a concession made for numerical tractability. The low neutral beta (neutral pressure to magnetic pressure ratio) suggests that inclusion of this force may not significantly change the results. The Harris-like magnetic field configuration was an idealization made in an attempt to generalize the problem. A detailed model of current sheet formation in the protosolar nebula would be needed to better parameterize the initial condition. At this time those details are lacking. The reconnective perturbation chosen was also open to various possibilities. The choice of a velocity perturbation limited discussion to the reconnecting state (a boundary value problem). At this point the system had little knowledge of the initial perturbation (corroborated through inspection of inflow and outflow mass fluxes). Cooling rates were assumed which fit the petrochemical evidence of chondrule formation but are difficult to reconcile with our assumptions of nebular thermal balance. Recent laboratory attempts to better understand dusty plasma bulk thermal properties suggest that the answer to this question may be more complicated than a gas-dynamic approach may suggest (Williams and Thomas, 2006, 2007). These simulations must be viewed from

within the framework of the assumptions which have been made.

The assumptions present in this work suggest future work which will relax some assumptions and better characterize the dusty plasma processes present in the protosolar nebula. Studies of reconnection must investigate the role that length scales play in the reconnective event. Using a similar model to the one present here (Harris-like) the current sheet thickness can be varied so that the magnetization length scales may be investigated. Investigation into the ion inertial length scales will require a code capable of handling the ion inertia (currently in development under the name nMHDust). Similarly, current sheet formation mechanisms should be investigated to better parameterize the length scales appropriate to the protosolar nebula. More advanced collisional models can also be examined. It is well known that ion-dust collisions are enhanced (beyond the classical coulomb rate) in laboratory dusty plasmas. A more detailed analysis of the thermal environment present in the nebula should be considered (possibly allowing for the inclusion of neutral pressure forces). Test-particle heating models could also examine dust mass spectrums and possible dust destruction through heating. Dusty plasmas provide a rich field of research and the results presented here will hopefully encourage future works.

Appendix A

Calculation of the mobilities

The DENISIS code (Schröer et al., 1998) calculates the electron and ion velocities through their mobilities. The calculation is outlined in the paper by Schröer et. al. and is reproduced here. It is argued that the electron and ion velocities can be related through their respective mobilities (μ) (Mitchner and C. H. Kruger, 1973). Calculations are conducted with respect to the coordinates defined by the magnetic field (parrallel to $\vec{B}$, in the Hall direction $\vec{E} \times \vec{B}$, and the Pederson $\perp$ direction)

$$v_{i\|} = \frac{\mu_{i\|}}{\mu_{e\|}} v_{e\|}, \quad v_{iH} = \frac{\mu_{iH}}{\mu_{eH}} v_{eH}, \quad \text{and} \quad v_{i\perp} = \frac{\mu_{i\perp}}{\mu_{e\perp}} v_{e\perp}.$$

The current due to the inertialess species (ions and electrons) may be denoted

$$\vec{w} = \vec{j} + Z_d e n_d \vec{v}_d = e n_i \vec{v}_i - e n_e \vec{v}_e,$$

where $\vec{j}, Z_d, e, n_k,$ and v_k denote total current, dust charge number, electron charge, species number density and specieis velocity respectively. From Mitchner and Kruger the mobilities may be written

$$\mu_{k\|} = \frac{q_k}{m_k v_k}, \quad \mu_{kH} = \frac{q_k}{m_k} \frac{\omega_{ck}}{(v_k^2 + \omega_{ck}^2)}, \quad \text{and} \quad \mu_{k\perp} = \frac{q_k}{m_k} \frac{v_k}{(v_k^2 + \omega_{ck}^2)}$$

where k references each species ($k = i, e$). Here $q_k, m_k, \omega_{ck},$ and v_k correspond to the species charge, species mass, species cyclotron frequency, and net species collision frequency respectively. We note that $v_i = v_{ie} + v_{in} + v_{id}$ and $v_e = v_{ei} + v_{en} + v_{ed}$ where $\rho_\alpha v_{\alpha\beta} = \rho_\beta v_{\beta\alpha}$. Table 1.2 gives the following values for reference

$$
\begin{aligned}
q_i &= 1.60 \times 10^{-19} [\text{C}] & q_e &= 1.60 \times 10^{-19} [\text{C}] \\
m_i &= 1.67 \times 10^{-27} [\text{kg}] & m_e &= 9.11 \times 10^{-31} [\text{kg}] \\
\omega_{ci} &= 9590 [\text{rad/s}] & \omega_{ce} &= 17.6 \times 10^6 [\text{rad/s}] \\
v_{ie} &= 2.06 \times 10^{-36} [\text{Hz}] & v_{ei} &= 3.78 \times 10^{-30} [\text{Hz}] \\
v_{id} &= 1.20 \times 10^{-8} [\text{Hz}] & v_{ed} &= 8.33 \times 10^{-4} [\text{Hz}] \\
v_{in} &= 1020 [\text{Hz}] & v_{en} &= 43,500 [\text{Hz}]
\end{aligned}
$$

The mobilities may now be calculated (note a change is made from [rad/s] to [Hz] for the cyclotron frequencies). All mobilities in units of [C s/kg]. For the ions

$$\mu_{i\|} = \frac{e}{m_i v_{ie}} = 93,900,$$

$$\mu_{iH} = \frac{e}{m_i} \frac{\omega_{ci}}{\left(v_i^2 + \omega_{ci}^2\right)} = 9880,$$

and

$$\mu_{i\perp} = \frac{e}{m_i} \frac{v_{ie}}{\left(v_{ie}^2 + \omega_{ci}^2\right)} = 1050.$$

For the electrons

$$\mu_{e\parallel} = \frac{e}{m_e v_{ei}} = 4.04 \times 10^6,$$

$$\mu_{eH} = \frac{e}{m_e} \frac{\omega_{ce}}{\left(v_{ei}^2 + \omega_{ce}^2\right)} = 9990,$$

and

$$\mu_{e\perp} = \frac{e}{m_e} \frac{v_{ei}}{\left(v_{ei}^2 + \omega_{ce}^2\right)} = 24.7.$$

This gives the following relationships between ion and electron velocity in the various directions.

$$v_{i\parallel} = 0.0232 v_{e\parallel}, \quad v_{iH} = 0.989 v_{eH}, \quad \text{and} \quad v_{i\perp} = 42.5 v_{e\perp}.$$

The electron currents become ($n_e = 1 \, [m^{-3}]$)

$$j_{e\parallel} = e n_e v_{e\parallel} = e v_{e\parallel}, \quad j_{eH} = e n_e v_{eH} = e v_{eH}, \quad \text{and} \quad j_{e\perp} = e n_e v_{e\perp} = e v_{e\perp}.$$

The ion currents become ($n_i = 1001 \, [m^{-3}]$)

$$j_{i\parallel} = e n_i v_{i\parallel} = 23.2 e v_{e\parallel}, \quad j_{iH} = e n_i v_{iH} = 990 e v_{eH}, \quad \text{and} \quad j_{i\perp} = e n_i v_{i\perp} = 42500 e v_{e\perp}.$$

These current equations may now be equated to find

$$j_{i\parallel} = 23.2 j_{e\parallel}, \quad j_{iH} = 990 j_{eH}, \quad \text{and} \quad j_{i\perp} = 42500 j_{e\perp}.$$

It should be clear that in the parallel, perpendicular and Hall ($\vec{E} \times \vec{B}$) directions the ion contribution is at least two orders of magnitude more than that of the electrons. Thus the neglect of and electron velocity (and electron contribution to the total current) is justified for the parameter regime given by table 1.2. The ion velocity may then be determined by

$$\vec{v}_i = \frac{\vec{w}}{n_i e}.$$

.

Appendix B

Ohm's Law

The DENISIS code neglects any effect due to ion inertia. It is argued that this is equivalent to the assumption made regarding the neglect of electron inertia in MHD. To evaluate this statement and better gauge the scaling of the various terms in Ohm's law, the ion inertial effects must be included in the derivation of the electric field. The derivation begins with the inertial ion equation of motion

$$\frac{\partial \rho_i \vec{v}_i}{\partial t} = -\nabla p_i + e n_i \left(\vec{E} + \vec{v}_i \times \vec{B} \right) - \rho_i \nu_{in} \left(\vec{v}_i - \vec{v}_n \right) - \rho_i \nu_{id} \left(\vec{v}_i - \vec{v}_d \right) - \rho_i \nu_{ie} \left(\vec{v}_i - \vec{v}_e \right). \tag{B.1}$$

The ion inertial equation of motion can now be rewritten in terms of the Lorentz transformation from the electric field in the rest frame $(\vec{E})$ to the co-moving frame $(\vec{E}')$

$$\vec{E}' = \vec{E} + \vec{v}_i \times \vec{B} = \frac{m_i}{e n_i} \frac{\partial n_i \vec{v}_i}{\partial t} + \frac{m_i}{e n_i} \nabla \cdot (n_i \vec{v}_i \vec{v}_i) + \frac{\nabla p_i}{e n_i} + \frac{\nu_{in}}{e} (\vec{v}_i - \vec{v}_n) + \frac{\nu_{id}}{e} (\vec{v}_i - \vec{v}_d) + \frac{\nu_{ie}}{e} (\vec{v}_i - \vec{v}_e). \tag{B.2}$$

We may now substitute the definition of current into this eqaution

$$\vec{j} = e n_i \vec{v}_i - Z_d e n_d \vec{v}_d - e n_e \vec{v}_e \tag{B.3}$$

which in the depleted electron regime ($n_e \sim 1, \nu_{ie} \sim 0, \vec{v}_e \sim 0$) may be written

$$\vec{j} = Z_d e n_d \left(\vec{v}_i - \vec{v}_d \right) = \frac{\nabla \times \vec{B}}{\mu_0}. \tag{B.4}$$

Note that the approximation that $Z_d n_d \sim n_i$ has been used. In the depleted electron regime, Ohm's law may then be written

$$\vec{E}' = \vec{E} + \vec{v}_d \times \vec{B} = \frac{m_i}{e^2 n_i} \left[\frac{\partial \vec{j}}{\partial t} + \nabla \cdot \left(\vec{j} \vec{v}_d + \vec{v}_d \vec{j} \right) \right] + \frac{m_i}{e^3 n_i} \nabla \cdot \left(\frac{\vec{j} \vec{j}}{n_i} \right) - \frac{\vec{j} \times \vec{B}}{e n_i} \tag{B.5}$$

$$+ \quad \frac{m_i Z_d}{e n_i} \left[\frac{\partial n_d \vec{v}_d}{\partial t} + \nabla \cdot (n_d \vec{v}_d \vec{v}_d) \right] + \frac{\nabla p_i}{e n_i} + \frac{m_i}{e^2 n_i} (\nu_{in} + \nu_{id}) \vec{j} - \frac{m_i}{e} \nu_{in} (\vec{v}_d - \vec{v}_n).$$

Each term in this equation scales with respect to the advective term $(\vec{v}_d \times \vec{B})$. The first term in the equation on the left is the ion inertial term ($\left[\partial \vec{j} / \partial t + \nabla \cdot \left(\vec{j} \vec{v}_d + \vec{v}_d \vec{j} \right) \right]$). Comparing the coefficient of this term with that of the advective term gives

$$\frac{m_i B_0}{e^2 n_i \mu_0 L_0 T_0} \approx V_0 B_0. \tag{B.6}$$

Table B.1. Scaling laws for the terms in Ohm's Law. Each term in Ohm's Law (Eqn. B.5) scales according to various plasma parameters. Here we note the following values: Ion Plasma Frequency (ω_{pi}), Dust Plasma Frequency (ω_{pd}), and Ion Gyroradius $(R_{gi} = \sqrt{m_i k_b T_i}/eB_0)$.

	Term	Scaling
Ion Inertia	$\partial \vec{j}/\partial t + \nabla \cdot \left(\vec{j}\vec{v}_d + \vec{v}_d\vec{j}\right)$	$L_{ion-inertia} \approx \frac{c}{\omega_{pi}}$
j^2 Term	$\nabla \cdot \left(\vec{j}\vec{j}/n_i\right)$	$L_{jj} \approx \left(\frac{c^3}{\omega_{pi}^2 \omega_{pd}}\right)^{1/3}$
Hall Term	$\vec{j} \times \vec{B}/en_i$	$L_{Hall} \approx \frac{c}{\omega_{pd}}$
Dust Inertia Term	$\partial n_d \vec{v}_d/\partial t + \nabla \cdot (n_d \vec{v}_d \vec{v}_d)$	$L_{dust-intertia} \approx R_{gi}$
Ion-stress Term	$\nabla p_i/en_i$	$L_{Ion-stress} \approx \frac{c}{\omega_{pd}}$
Collisional Resistivity Term	$(\nu_{in} + \nu_{id})\vec{j}$	$L_{coll-res} \approx \frac{c}{\omega_{pi}}$
Dust-neutral term	$\nu_{in}(\vec{v}_d - \vec{v}_n)$	$L_{dust-neutral} = R_{gi}$

The following approximations were used: $\nabla \approx 1/L_0$, $|\vec{j}| \approx B_0/(\mu_0 L_0)$, and $\partial/\partial t \approx 1/T_0$, where B_0, L_0, and V_0 are the stereotypical magnetic field, length scale, and velocity respectively. It becomes clear that this term becomes important as length scales approach the ion inertial length scale

$$L_{ion-inertia} \approx c\left(\frac{m_i \varepsilon_0}{n_i e^2}\right)^{1/2} = \frac{c}{\omega_{pi}} \tag{B.7}$$

where ω_{pi} is the ion plasma frequency. Similar constraints can be developed for each term in Ohm's law (Eqn. B.5), and are listed in Table B.1.

The ion skin depth (c/ω_{pi}), dust skin depth (c/ω_{pd}), and ion gyroradius (R_{gi}) give insight to the relevant length scales at play in the protosolar nebula. In normalized (simulation) units these values are $c/\omega_{pd} = 2.19$, $c/\omega_{pi} = 0.00089$, and $R_{gi} = 3.64 \times 10^{-7}$. Given our grid scaling and the neglect of ion inertia in the DENISIS code, only the Hall and ion-stress terms are relevant. The collisional-resistivity term is also relevant given the large value of the ion-neutral collision frequency. These terms become relevant on length scales smaller than the dust inertial length scale. Given our current sheet thickness $(\delta = 1.0)$ is of the order of the dust inertial length scale, the effects of these terms will be present.

This analysis has been conducted in terms of the relevant length scales but time scales may also be examined. A similar analysis to that conducted above may be carried out.

This time each equation is solved in terms of a time-scale. The results may also be achieved by simply dividing the relevant length scale by the stereotypical Alvén velocity. The ion inertia and collisional resistivity term become relevant on timescales smaller than the ion gyro-period. The same can be said of the j^2 term. The Hall and ion-stress terms become relevant on timescales smaller than the dust gyro-period. The dust inertia and dust-neutral term become relevant on timescales smaller than the product of the ion gyro-period and the square root of the plasma beta. Both temporal and spatial methodologies produce equivalent results when applied to a given set of parameters.

Appendix C

Calculation of coefficient terms

The set of equations integrated by the DENISIS code include various coefficients. These coefficients exist for both derivative and source terms. Explicit values for these coefficients are presented below for the momentum, induction, and energy equations. The continuity equations contain no such terms.

C.1 Momentum Equations

The coefficients for the momentum equations are show in Table C.1. It should be clear that the dust neutral collisional term dominates with the ion-neutral term being an order of magnitude less. The electron neutral collisional term is five orders of magnitude less than that of the dust-neutral term, validating its neglect in the code. The neglect of electron-neutral collisions is achieved through explicitly setting the electron neutral collision frequency to zero. The choice of electron-neutral collision frequency also addresses a problem associated with the low electron mobility regime. Explicitly setting the electron velocity to zero turns the electron neutral term into a pseudo viscosity in both momentum equations. The explicit choice of a zero electron-neutral collision frequency avoids this issue.

Table C.1. Calculation of the coefficient terms for the momentum equations. The dust and neutral momentum equations contain the same coefficients so only one must be explicitly shown.

Equation

$$\frac{\partial(\rho_d \vec{v}_d)}{\partial t} = -\nabla \cdot (\rho_d \vec{v}_d \vec{v}_d) - \nabla \left(p_e + p_i + p_d\right) + \frac{1}{4\pi} \left(\nabla \times \vec{B}\right) \times \vec{B}$$

$$-\nu_{dn}\rho_d \left(\vec{v}_d - \vec{v}_n\right) - \nu_{in}\rho_i \left(\vec{v}_i - \vec{v}_n\right) - \nu_{en}\rho_e \left(\vec{v}_e - \vec{v}_n\right)$$

Nebular Values

$$\nu_{dn}\rho_d = \left(0.00415\,[s^{-1}]\right)\left(1 \times 10^{-17}\,[kg/m^3]\right) = 4.15 \times 10^{-20} \left[\frac{kg}{m^3 s}\right]$$

$$\nu_{in}\rho_i = \left(1020\,[s^{-1}]\right)\left(1.67 \times 10^{-24}\,[kg/m^3]\right) = 1.70 \times 10^{-21} \left[\frac{kg}{m^3 s}\right]$$

$$\nu_{en}\rho_e = \left(43500\,[s^{-1}]\right)\left(9.11 \times 10^{-31}\,[kg/m^3]\right) = 3.96 \times 10^{-26} \left[\frac{kg}{m^3 s}\right]$$

Simulation (Normalized) Values

$$\nu_{dn}\rho_d = (7.46)(1.0) = 7.46$$

$$\nu_{in}\rho_i = \left(1.83 \times 10^6\right)\left(1.67 \times 10^{-7}\right) = 0.306$$

$$\nu_{en}\rho_e = (0.0)\left(9.11 \times 10^{-14}\right) = 0.0$$

C.2 Induction Equation

The coefficients for the induction equation are shown in Table C.2. The ion-neutral collisional term is clearly the most important followed by the ion-dust collisional term (six orders of magnitude smaller). The neglect of the ion-electron collision frequency is again motivated by its low value coupled with the perviously mentioned spurious effects of explicitly setting the electron velocity to zero.

Table C.2. Calculation of the coefficient terms for the induction equation. Neglect of the ion-electron collisions is clearly justified by its low value.

Equation

$$\frac{\partial \vec{B}}{\partial t} = -\frac{m_i c}{e} \nabla \times \left(\frac{\nabla p_i}{\rho_i} \right) + \nabla \times \left(\vec{v}_i \times \vec{B} \right) - \frac{m_i c}{e} \nabla \times \left[\nu_{id} \left(\vec{v}_i - \vec{v}_d \right) + \nu_{in} \left(\vec{v}_i - \vec{v}_n \right) + \nu_{ie} \left(\vec{v}_i - \vec{v}_e \right) \right]$$

Nebular Values

$$\frac{m_i c}{e} \nu_{id} = \frac{\left(1.67 \times 10^{-27} [kg] \right) \left(2.998 \times 10^8 [m/s] \right)}{\left(1.602 \times 10^{-19} [C] \right)} \left(1.2 \times 10^{-8} \left[s^{-1} \right] \right) = 3.59 \times 10^{-8} \left[\frac{kg \cdot m}{C \cdot s^2} \right]$$

$$\frac{m_i c}{e} \nu_{in} = \frac{\left(1.67 \times 10^{-27} [kg] \right) \left(2.998 \times 10^8 [m/s] \right)}{\left(1.602 \times 10^{-19} [C] \right)} \left(1020 \left[s^{-1} \right] \right) = 3190 \left[\frac{kg \cdot m}{C \cdot s^2} \right]$$

$$\frac{m_i c}{e} \nu_{ie} = \frac{\left(1.67 \times 10^{-27} [kg] \right) \left(2.998 \times 10^8 [m/s] \right)}{\left(1.602 \times 10^{-19} [C] \right)} \left(3.78 \times 10^{-30} \left[s^{-1} \right] \right) = 1.18 \times 10^{-29} \left[\frac{kg \cdot m}{C \cdot s^2} \right]$$

Simulation (Normalized) Values

$$\frac{m_i \nu_{id}}{e} = \left(1.67 \times 10^{-11} \right) \left(2.16 \times 10^{-5} \right) / \left(2.88 \times 10^{-4} \right) = 1.25 \times 10^{-12}$$

$$\frac{m_i \nu_{in}}{e} = \left(1.67 \times 10^{-11} \right) \left(1.83 \times 10^6 \right) / \left(2.88 \times 10^{-4} \right) = 0.106$$

$$\frac{m_i \nu_{ie}}{e} = \left(1.67 \times 10^{-11} \right) \left(0.0 \right) / \left(2.88 \times 10^{-4} \right) = 0.0$$

C.3 Dust Energy Equation

The coefficients for the dust energy equation are shown in Table C.3. It becomes evident that the dust energy source terms are dominated by the dust-neutral thermalization term. The spurious effects of zero electron velocity are of little impact, given the small coefficient for the dust-electron collisional heating term.

Table C.3. Calculation of the coefficient terms for the dust energy equation. The polytropic indicies have been chosen such that $\gamma_d = \gamma_i = \gamma_e = \gamma_n = 5/3$ in order to simplify the terms.

Equation

$$\frac{\partial p_d}{\partial t} = -\nabla \cdot \left(p_d \vec{v}_d\right) - \frac{2}{3} p_d \nabla \cdot \vec{v}_d$$

$$+ \frac{2}{3} \frac{m_d}{m_d + m_i} \rho_i v_{id} \left(\vec{v}_d - \vec{v}_i\right)^2 + \frac{2}{3} \frac{m_n}{m_d + m_n} \rho_d v_{dn} \left(\vec{v}_d - \vec{v}_n\right)^2 + \frac{2}{3} \frac{m_e}{m_d + m_e} \rho_d v_{de} \left(\vec{v}_d - \vec{v}_e\right)^2$$

$$- 2 \frac{\rho_i v_{id}}{m_d + m_i} \left(k_B T_d - k_B T_i\right) - 2 \frac{\rho_d v_{dn}}{m_d + m_n} \left(k_B T_d - k_B T_n\right) - 2 \frac{\rho_d v_{de}}{m_d + m_e} \left(k_B T_d - k_B T_e\right)$$

Nebular Values

$$\frac{2}{3} \frac{m_d}{m_d + m_i} \rho_i v_{id} \; = \; \frac{2}{3} \frac{(1.67 \times 10^{-27} [kg])}{(1.0 \times 10^{-16} [kg])} \left(1.67 \times 10^{-24} \, [kg/m^3]\right) \left(1.20 \times 10^{-8} \, [s^{-1}]\right) \; = \; 2.23 \times 10^{-43} \left[\frac{kg}{m^3 s}\right]$$

$$\frac{2}{3} \frac{m_n}{m_d + m_n} \rho_d v_{dn} \; = \; \frac{2}{3} \frac{(1.67 \times 10^{-27} [kg])}{(1.0 \times 10^{-16} [kg])} \left(1.00 \times 10^{-17} \, [kg/m^3]\right) \left(0.00415 \, [s^{-1}]\right) \; = \; 4.62 \times 10^{-31} \left[\frac{kg}{m^3 s}\right]$$

$$\frac{2}{3} \frac{m_e}{m_d + m_e} \rho_d v_{de} \; = \; \frac{2}{3} \frac{(9.11 \times 10^{-31} [kg])}{(1.0 \times 10^{-16} [kg])} \left(1.00 \times 10^{-17} \, [kg/m^3]\right) \left(7.59 \times 10^{-17} \, [s^{-1}]\right) \; = \; 4.61 \times 10^{-48} \left[\frac{kg}{m^3 s}\right]$$

$$2 \frac{\rho_i v_{id}}{m_d + m_i} \; = \; 2 \frac{\left(1.67 \times 10^{-24} [kg/m^3]\right)\left(1.20 \times 10^{-8} [s^{-1}]\right)}{\left(1.00 \times 10^{-16} [kg]\right)} \; = \; 4.01 \times 10^{-16} \left[\frac{1}{m^3 s}\right]$$

$$2 \frac{\rho_d v_{dn}}{m_d + m_n} \; = \; 2 \frac{\left(1.00 \times 10^{-17} [kg/m^3]\right)\left(0.00415 [s^{-1}]\right)}{\left(1.00 \times 10^{-16} [kg]\right)} \; = \; 8.30 \times 10^{-4} \left[\frac{1}{m^3 s}\right]$$

$$2 \frac{\rho_d v_{de}}{m_d + m_e} \; = \; 2 \frac{\left(1.00 \times 10^{-17} [kg/m^3]\right)\left(7.59 \times 10^{-17} [s^{-1}]\right)}{\left(1.00 \times 10^{-16} [kg]\right)} \; = \; 1.57 \times 10^{-17} \left[\frac{1}{m^3 s}\right]$$

Simulation (Normalized) Values

$$\frac{2}{3} \frac{m_d}{m_d + m_i} \rho_i v_{id} \; = \; \frac{2}{3} \frac{(1.67 \times 10^{-11})}{(1.00)} \left(1.67 \times 10^{-7}\right) \left(2.16 \times 10^{-5}\right) \; = \; 4.02 \times 10^{-23}$$

$$\frac{2}{3} \frac{m_n}{m_d + m_n} \rho_d v_{dn} \; = \; \frac{2}{3} \frac{(1.67 \times 10^{-11})}{(1.00)} (1.00)(7.46) \; = \; 8.31 \times 10^{-11}$$

$$\frac{2}{3} \frac{m_e}{m_d + m_e} \rho_d v_{de} \; = \; \frac{2}{3} \frac{(9.11 \times 10^{-24})}{(1.00)} (1.00) \left(1.37 \times 10^{-13}\right) \; = \; 8.32 \times 10^{-37}$$

$$2 \frac{\rho_i v_{id}}{m_d + m_i} \; = \; 2 \frac{\left(1.67 \times 10^{-7}\right)\left(2.16 \times 10^{-5}\right)}{(1.00)} \; = \; 7.21 \times 10^{-12}$$

$$2 \frac{\rho_d v_{dn}}{m_d + m_n} \; = \; 2 \frac{(1.00)(7.46)}{(1.00)} \; = \; 14.9$$

$$2 \frac{\rho_i v_{de}}{m_d + m_e} \; = \; 2 \frac{(1.00)\left(1.37 \times 10^{-13}\right)}{(1.00)} \; = \; 2.74 \times 10^{-13}$$

C.4 Ion Energy Equation

The coefficients for the ion energy equation are shown in Table C.4. It is clear that ion-neutral thermalization terms dominate the ion energy equations. This implies that the ion and neutral pressures are well coupled. The ion-neutral collisional heating term is the only significant source of heating in the ion energy equation. Careful choice of the time step is required in order to properly resolve these thermal phenomena.

Table C.4. Calculation of the coefficient terms for the ion energy equation. The polytropic indicies have been chosen such that $\gamma_d = \gamma_i = \gamma_e = \gamma_n = 5/3$ in order to simplify the terms.

Equation

$$\frac{\partial p_i}{\partial t} = -\nabla \cdot (p_i \vec{v}_i) - \frac{2}{3} p_i \nabla \cdot \vec{v}_i + \frac{2}{3} \frac{m_n}{m_i+m_n} \rho_i \nu_{in} (\vec{v}_i - \vec{v}_n)^2 + \frac{2}{3} \frac{m_d}{m_d+m_i} \rho_i \nu_{id} (\vec{v}_i - \vec{v}_d)^2 + \frac{2}{3} \frac{m_e}{m_i+m_e} \rho_i \nu_{ie} (\vec{v}_i - \vec{v}_e)^2$$

$$-2 \frac{\rho_i \nu_{in}}{m_i+m_n} (k_B T_i - k_B T_n) - 2 \frac{\rho_i \nu_{id}}{m_d+m_i} (k_B T_i - k_B T_d) - 2 \frac{\rho_i \nu_{ie}}{m_i+m_e} (k_B T_i - k_B T_e)$$

Nebular Values

$$\frac{2}{3} \frac{m_i}{m_i+m_n} \rho_i \nu_{in} = \frac{2}{3} \frac{(1.67 \times 10^{-27} [kg])}{(3.34 \times 10^{-27} [kg])} (1.67 \times 10^{-24} [kg/m^3]) (1020 [s^{-1}]) = 5.68 \times 10^{-22} \left[\frac{kg}{m^3 s}\right]$$

$$\frac{2}{3} \frac{m_d}{m_d+m_i} \rho_i \nu_{id} = \frac{2}{3} \frac{(1.00 \times 10^{-16} [kg])}{(1.00 \times 10^{-16} [kg])} (1.67 \times 10^{-24} [kg/m^3]) (1.20 \times 10^{-8} [s^{-1}]) = 1.34 \times 10^{-32} \left[\frac{kg}{m^3 s}\right]$$

$$\frac{2}{3} \frac{m_e}{m_i+m_e} \rho_i \nu_{ie} = \frac{2}{3} \frac{(9.11 \times 10^{-31} [kg])}{(1.67 \times 10^{-27} [kg])} (1.67 \times 10^{-24} [kg/m^3]) (2.06 \times 10^{-36} [s^{-1}]) = 1.23 \times 10^{-63} \left[\frac{kg}{m^3 s}\right]$$

$$2 \frac{\rho_i \nu_{in}}{m_i+m_n} = 2 \frac{(1.67 \times 10^{-24} [kg/m^3])(1020 [s^{-1}])}{(3.34 \times 10^{-27} [kg])} = 1.02 \times 10^6 \left[\frac{1}{m^3 s}\right]$$

$$2 \frac{\rho_i \nu_{id}}{m_d+m_i} = 2 \frac{(1.67 \times 10^{-24} [kg/m^3])(1.20 \times 10^{-8} [s^{-1}])}{(1.00 \times 10^{-16} [kg])} = 4.01 \times 10^{-16} \left[\frac{1}{m^3 s}\right]$$

$$2 \frac{\rho_i \nu_{ie}}{m_i+m_e} = 2 \frac{(1.67 \times 10^{-24} [kg/m^3])(2.06 \times 10^{-36} [s^{-1}])}{(1.67 \times 10^{-27} [kg])} = 4.12 \times 10^{-33} \left[\frac{1}{m^3 s}\right]$$

Simulation (Normalized) Values

$$\frac{2}{3} \frac{m_i}{m_i+m_n} \rho_i \nu_{in} = \frac{2}{3} \frac{(1.67 \times 10^{-11})}{(3.34 \times 10^{-11})} (1.67 \times 10^{-7}) (1.83 \times 10^6) = 0.102$$

$$\frac{2}{3} \frac{m_d}{m_d+m_i} \rho_i \nu_{id} = \frac{2}{3} \frac{(1.00)}{(1.00)} (1.67 \times 10^{-7}) (2.16 \times 10^{-5}) = 2.40 \times 10^{-12}$$

$$\frac{2}{3} \frac{m_e}{m_i+m_e} \rho_i \nu_{ie} = \frac{2}{3} \frac{(9.11 \times 10^{-15})}{(1.67 \times 10^{-11})} (1.67 \times 10^{-7}) (0.00) = 0.00$$

$$2 \frac{\rho_i \nu_{in}}{m_i+m_n} = 2 \frac{(1.67 \times 10^{-7})(1.83 \times 10^6)}{(3.34 \times 10^{-11})} = 1.83 \times 10^{10}$$

$$2 \frac{\rho_i \nu_{id}}{m_d+m_i} = 2 \frac{(1.67 \times 10^{-7})(2.16 \times 10^{-5})}{(1.00)} = 7.21 \times 10^{-12}$$

$$2 \frac{\rho_i \nu_{ie}}{m_i+m_e} = 2 \frac{(1.67 \times 10^{-7})(0.00)}{(1.67 \times 10^{-11})} = 0.00$$

C.5 Neutral Energy Equation

The coefficients for the neutral energy equation are shown in Table C.5. As was the case with the ion energy equation, the ion-neutral thermalization term dominates the neutral energy equation. However, the neutral-dust collisional heating is an order of magnitude larger than that of the ion-neutral collisional heating. Neglect of the electrons through the assumption of vanishing electron-neutral collision frequency is clearly justified in the case of the collisional heating terms. In the case of the thermalization terms it is less clear that the electron-neutral interaction should be neglected. In effect, the electron temperature should be well coupled to the ion-neutral system. The depleted electron regime implies a negligible contribution of the electrons to the overall dynamics of the system. The electron-neutral interaction may then be safely ignored.

The strong coupling between the ions and neutrals suggest that the ion and neutral fluids be combined into a single energy equation. If the sum of the two energy equations is taken and the net ion-neutral pressure is written $p_{in} = p_i + p_n$, it may be written

$$
\frac{\partial p_{in}}{\partial t} = -\nabla \cdot (p_{in}\vec{v}_n) - (\gamma - 1)p_{in}\nabla \cdot \vec{v}_n + (\gamma - 1)\frac{m_d\rho_d}{m_d + m_n}(v_{dn} + v_{di})(\vec{v}_d - \vec{v}_n)^2 \quad \text{(C.1)}
$$
$$
- 2\frac{\rho_d(v_{dn} + v_{di})}{m_d + m_n}(k_BT_n - k_BT_d),
$$

$$
\frac{\partial p_d}{\partial t} = -\nabla \cdot (p_d\vec{v}_d) - (\gamma - 1)p_d\nabla \cdot \vec{v}_d + (\gamma - 1)\frac{m_n\rho_d}{m_d + m_n}(v_{dn} + v_{di})(\vec{v}_d - \vec{v}_n)^2 \quad \text{(C.2)}
$$
$$
- 2\frac{\rho_d(v_{dn} + v_{di})}{m_d + m_n}(k_BT_d - k_BT_n),
$$

Table C.5. Calculation of the coefficient terms for the neutral energy equation. The polytropic indicies have been chosen such that $\gamma_d = \gamma_i = \gamma_e = \gamma_n = 5/3$ in order to simplify the terms.

Equation

$$\frac{\partial p_n}{\partial t} = -\nabla \cdot \left(p_n \vec{v}_n\right) - \frac{2}{3}p_n \nabla \cdot \vec{v}_n$$

$$+\frac{2}{3}\frac{m_i}{m_i+m_n}\rho_i v_{in}\left(\vec{v}_i - \vec{v}_n\right)^2 + \frac{2}{3}\frac{m_d}{m_d+m_n}\rho_d v_{dn}\left(\vec{v}_d - \vec{v}_n\right)^2 + \frac{2}{3}\frac{m_e}{m_n+m_e}\rho_e v_{en}\left(\vec{v}_e - \vec{v}_n\right)^2$$

$$-2\frac{\rho_i v_{in}}{m_i+m_n}\left(k_B T_n - k_B T_i\right) - 2\frac{\rho_d v_{dn}}{m_d+m_n}\left(k_B T_n - k_B T_d\right) - 2\frac{\rho_e v_{en}}{m_n+m_e}\left(k_B T_n - k_B T_e\right)$$

Nebular Values

$\frac{2}{3}\frac{m_i}{m_i+m_n}\rho_i v_{in}$	$=$	$\frac{2}{3}\frac{(1.67\times10^{-27}[kg])}{(3.34\times10^{-27}[kg])}\left(1.67\times10^{-24}\,[kg/m^3]\right)\left(1020\,[s^{-1}]\right)$	$=$	$5.68\times10^{-22}\left[\frac{kg}{m^3 s}\right]$
$\frac{2}{3}\frac{m_d}{m_d+m_n}\rho_d v_{dn}$	$=$	$\frac{2}{3}\frac{(1.00\times10^{-16}[kg])}{(1.00\times10^{-16}[kg])}\left(1.00\times10^{-17}\,[kg/m^3]\right)\left(0.00415\,[s^{-1}]\right)$	$=$	$2.77\times10^{-20}\left[\frac{kg}{m^3 s}\right]$
$\frac{2}{3}\frac{m_e}{m_n+m_e}\rho_e v_{en}$	$=$	$\frac{2}{3}\frac{(9.11\times10^{-31}[kg])}{(1.67\times10^{-27}[kg])}\left(9.11\times10^{-31}\,[kg/m^3]\right)\left(43500\,[s^{-1}]\right)$	$=$	$1.42\times10^{-29}\left[\frac{kg}{m^3 s}\right]$
$2\frac{\rho_i v_{in}}{m_i+m_n}$	$=$	$2\frac{(1.67\times10^{-24}[kg/m^3])(1020[s^{-1}])}{(3.34\times10^{-27}[kg])}$	$=$	$1.02\times10^{6}\left[\frac{1}{m^3 s}\right]$
$2\frac{\rho_d v_{dn}}{m_d+m_n}$	$=$	$2\frac{(1.00\times10^{-17}[kg/m^3])(0.00415[s^{-1}])}{(1.00\times10^{-16}[kg])}$	$=$	$8.03\times10^{-4}\left[\frac{1}{m^3 s}\right]$
$2\frac{\rho_e v_{en}}{m_n+m_e}$	$=$	$2\frac{(9.11\times10^{-31}[kg/m^3])(43500[s^{-1}])}{(1.67\times10^{-27}[kg])}$	$=$	$47.5\left[\frac{1}{m^3 s}\right]$

Simulation (Normalized) Values

$\frac{2}{3}\frac{m_i}{m_i+m_n}\rho_i v_{in}$	$=$	$\frac{2}{3}\frac{(1.67\times10^{-11})}{(3.34\times10^{-11})}\left(1.67\times10^{-7}\right)\left(1.83\times10^{6}\right)$	$=$	0.102
$\frac{2}{3}\frac{m_d}{m_d+m_n}\rho_d v_{dn}$	$=$	$\frac{2}{3}\frac{(1.00)}{(1.00)}(1.00)(7.46)$	$=$	4.98
$\frac{2}{3}\frac{m_e}{m_n+m_e}\rho_e v_{en}$	$=$	$\frac{2}{3}\frac{(9.11\times10^{-15})}{(1.67\times10^{-11})}\left(9.11\times10^{-24}\right)(0.00)$	$=$	0.00
$2\frac{\rho_i v_{in}}{m_i+m_n}$	$=$	$2\frac{(1.67\times10^{-7})(1.83\times10^{6})}{(3.34\times10^{-11})}$	$=$	1.83×10^{10}
$2\frac{\rho_d v_{dn}}{m_d+m_n}$	$=$	$2\frac{(1.00)(7.46)}{(1.00)}$	$=$	14.9
$2\frac{\rho_e v_{en}}{m_e+m_n}$	$=$	$2\frac{(9.11\times10^{-24})(0.00)}{(1.67\times10^{-11})}$	$=$	0.00

Bibliography

Alfvén, H., 1954. On the Origin of the Solar System. Oxford Clarendon Press, Oxford.

Allegre, C. J., Manhes, G., Gopel, C., 1995. The age of the earth. Geochimica et Cosmochimica Acta 59 (8), 1445–1456.

Balbus, S. A., Hawley, J. F., 1991. A powerful local shear instability in weakly magnetized disks. i. linear analysis. The Astrophysical Journal 376, 214–222.

Barkan, A., D'Angelo, N., Merlino, R. L., Dec. 1994. Charging of dust grains in a plasma. Physical Review Letters 73, 3093–3096.

Barnes, M. S., Keller, J. H., Forster, J. C., O'Neill, J. A., Coultas, D. K., Jan. 1992. Transport of dust particles in glow-discharge plasmas. Physical Review Letters 68, 313–316.

Bell, K. R., Lin, D. N. C., Jun. 1994. Using fu orionis outbursts to constrain self-regulated protostellar disk models. The Astrophysical Journal 427, 987–1004.

Bell, K. R., Lin, D. N. C., 1995. The fu orionis outburst as a thermal accretion event: Observational constraints for protostellar disk models. The Astrophysical Journal 444, 376–395.

Benkadda, S., Gabbai, P., Tsytovich, V., Verga, A., 1996. Nonlinearities and instabilities of dissipative drift waves in dusty plasmas. Phys. Rev. E 53 (3), 2717–2725.

Birk, G. T., Kopp, A., Lesch, H., 2001. Magnetisation of partially ionised dusty disks. Journal of Plasma Physics 66 (3), 213–222.

Birk, G. T., Wiechen, H. M., 2001. Resistive tearing mode instabilities in partially ionized dusty plasmas. ISSS 6, 222–225.

Birk, G. T., Wiechen, H. M., 2002. Shear flow instabilities in magnetized partially ionized dense dusty plasmas. Physics of Plasmas 9 (3), 964–970.

Birk, G. T., Wiechen, H. M., Kopp, A., Lesch, H., 2003. The magnetization of protoplanetary discs. Mon. Not. R. Astron. Soc. 339, 455–459.

Birn, J., Galsgaard, K., Hesse, M., Hoshino, M., Huba, J., Lapenta, G., Pritchett, P. L., Schindler, K., Yin, L., Büchner, J., NeuKirch, T., Priest, E. R., Mar. 2005. Forced magnetic reconnection. Geophysical Research Letters 32, 6105–+.

Birn, J., Hesse, M., Mar. 2001. Geospace environment modeling (gem) magnetic reconnection challenge: Resistive tearing, anisotropic pressure and hall effects. Journal of Geophysical Research 106, 3737–3750.

Biskamp, D., Nov. 2000. Magnetic Reconnection in Plasmas. Magnetic reconnection in plasmas, Cambridge, UK: Cambridge University Press, 2000 xiv, 387 p. Cambridge monographs on plasma physics, vol. 3, ISBN 0521582881.

Boss, A. P., 1988. High temperatures in the early solar nebula. Science 241, 565–567.

Boss, A. P., 1996. A concise guide to condrule formation models. Condrules and the Protoplanetary Disk, 257–263.

Boss, A. P., 1998. Temperatures in protoplanetary disks. Annual Review of Earth and Planetary Sciences 26, 53–80.

Brownlee, D. E., Bates, B., Beauchamp, R. H., 1983. Meteor ablation spherules as chondrule analogs. In: King, E. A. (Ed.), Chondrules and their Origins. pp. 10–25.

Butler, 1972. Natural remanent magnetization and thermomagnetic properties of the allende meteorite. Earth and Planetary Science Letters 17, 120–128.

Calvet, N., Gullbring, E., Dec. 1998. The structure and emission of the accretion shock in t tauri stars. The Astrophysical Journal 509, 802–818.

Cameron, A. G., 1995. The first ten million years in the solar nebula. Meteoritics and Planetary Science 30, 133–161.

Cameron, A. G., Fegley, M. B., 1982. Nucleation and condensation in the primitive solar nebula. ICARUS 52, 1–13.

Carroll, B. W., Ostlie, D. A., 1996. Introduction to Modern Astrophysics. Addison Wesley, New York.

Cassen, P., Dec. 1994. Utilitarian models of the solar nebula. Icarus 112, 405–429.

Chen, F. F., 1965. Electric probes. In: Huddlestone, R. H., Leonard, S. L. (Eds.), Plasma Diagnostic Techniques. pp. 113–+.

Chen, F. F., Jun. 1995. Industrial applications of low-temperature plasma physics. Physics of Plasmas 2, 2164–2175.

de Angelis, U., May 1992. The physics of dusty plasmas. Phyica Scripta 45, 465–474.

Desch, S. J., H. C. Connolly, J., 2002. A model of the thermal processing of particles in solar nebula shocks: Application to the cooling rate of chondrules. Meteroitics and Planetary Science 37, 183–207.

Dodd, R. T., 1981. Meteorites - A petrologic-chemical synthesis. Cambridge University Press.

Eisenhour, D. D., January 1994. Electromagnetic heating in the early solar nebula and the formation of chondrules. Ph.D. thesis, AA(Arizona State Univ.).

Eisenhour, D. D., Buseck, P. R., Sep. 1995. Chondrule formation by radiative heating: A numerical model. Icarus 117, 197–211.

Fireman, E. L., Defelice, J., Norton, E., Aug. 1970. Ages of the allende meteorite. Geochimica et Cosmochimica Acta 34, 873–881.

Fletcher, C. A. J., 1991. Computational Techniques for Fluid Dynamics: Volume 1 Fundamental and General Techniques. Springer, New York.

Forbes, T., Priest, E. R., Sep. 1984. Numerical simulation of reconnection in an emerging magnetic flux region. Solar Physics 94, 315–340.

Gooding, J. L., Keil, K., Mar. 1981. Relative abundances of chondrule primary textural types in ordinary chondrites and their bearing on conditions of chondrule formation. Meteoritics 16, 17–43.

Greene, T., 2001. Protostars: 'stellar embryology' takes a step forward with the first detailed look at the youngest sun-like stars. American Scientist 89, 316–324.

H. C. Connolly, J., Love, S. G., 1998. The formation of chondrules: Petrologic tests of the shock wave model. Science 280, 62–67.

Harris, E. G., 1962. On a plasma sheath separating regions of oppositely directed magnetic field. Il Nuovo Cimento 23 (1), 115–121.

Hartman, L., Kenyon, S. J., 1985. On the nature of fu orionis objects. The Astrophysical Journal 299, 462–478.

Hawley, J. F., Balbus, S. A., 1991. A powerful local shear instability in weakly ionized disks ii. nonlinear evolution. The Astrophysical Journal 276, 223–233.

Hawley, J. F., Stone, J. M., 1998. Nonlinear evolution of the magnetorotational instability in ion-neutral disks. The Astrophysical Journal 510, 758–771.

Herbig, G. H., Nov. 1977. Eruptive phenomena in early stellar evolution. The Astrophysical Journal 217, 693–715.

Hesse, M., Birn, J., 1993. Three-dimensional magnetotail equilibria by numerical relaxation techniques. Journal of Geophysical Research 98 (A3), 3973–3982.

Hewins, R. H., Jones, R. H., Scott, E. R., 1996. Chondrules and the Protoplanetary Disk. Cambridge University Press, New York, NY.

Hewins, R. H., Radomsky, P. M., Dec. 1990. Temperature conditions for chondrule formation. Meteoritics 25, 309–318.

Hood, L. L., Horányi, M., Oct. 1991. Gas dynamic heating of chondrule precursor grains in the solar nebula. Icarus 93, 259–269.

Hood, L. L., Horányi, M., Nov. 1993. The nebular shock wave model for chondrule formation - one-dimensional calculations. Icarus 106, 179–+.

Horányi, M., Morfill, G. E., Goertz, C. K., Levy, E. H., Mar. 1995. Chondrule formation in lightning discharges. Icarus 114, 174–185.

Hunter, C., Sep. 1962. The instability of the collapse of a self-gravitating gas cloud. The Astrophysical Journal 136, 594–+.

Jones, R. H., Scott, E. R., 1989. Petrology and thermal history of type ia chondrules in the semarkona (ll3.0) chondrite. In: Ryder, G., Sharpton, V. L. (Eds.), Lunar and Planetary Science Conference. Vol. 19 of Lunar and Planetary Science Conference. pp. 523–536.

Joung, M. K., Low, M. M., Ebel, D. S., 2004. Chondrule formation and protoplanetary disk heating by current sheets in nonideal magnetohydrodynamic turbulence. The Astrophysical Journal 606, 532–541.

Jovanović, D., Shukla, P. K., Morfill, G. E., Apr. 2005. Magnetic reconnection on the ion-skin-depth scale in the dusty magnetotail of a comet. Physics of Plasmas 12 (4).

Kieffer, S. W., Aug. 1975. Droplet chondrules. Science 189, 333–340.

King, E. A., 1983. Reduction, partial evaporation, and spattering - possible chemical and physical processes in fluid drop chondrule formation. In: King, E. A. (Ed.), Chondrules and their Origins. pp. 180–187.

Kubo, R., 1999. Statistical Mechanics. North-Holland Personal Library, New York.

Kulsrud, R. M., Jun. 2001. Magnetic reconnection: Sweet-parker versus petschek. Earth, Planets, and Space 53, 417–422.

Lada, C. J., 1985. Cold outflows, energetic winds, and enigmatic jets around young stellar objects. Ann. Rev. of Astr. and Astrophys. 23, 267–317.

Larson, R. B., Aug. 1983. Angular momentum and protostellar disks. Revista Mexicana de Astronomia y Astrofisica, vol. 7 7, 219–+.

Lazerson, S. A., Wiechen, H. M., 2008. Three-dimensional simulations of magnetic reconnection in a dusty plasma. Journal of Plasma Physics 74 (4), 493–513.

Levy, E. H., Araki, S., 1989. Magnetic reconnection flares in the photoplanetary nebula and the possible origin of meteorite chondrules. Icarus 81 (1), 74–91.

Levy, E. H., Sonnet, C. P., 1978. Meteorite magnetism and early solar system magnetic fields. Protostars and Planets: Studies of Star Formation and of the Origin of the Solar System.

Liffman, K., 1992. The formation of chondrules via ablation. Icarus 100, 608–620.

Love, S. G., Keil, K., Scott, E. R., 1994. Formation of chondrules by electrical discharge heating. Lunar and Planetary Inst., Papers Presented to the Conference on Chondrules and the Protoplanetary Disk, 21–22.

Mendis, D. A., Rosenberg, M., 1994. Cosmic dusty plasmas. Ann. Rev. of Astr. and Astrophys. 32, 419–463.

Merrill, G. P., Aug. 1920. On chondrules and chondritic structure in meteorites. Proceedings of the National Academy of Science 6, 449–472.

Minster, J. F., Allegre, C. J., Mar. 1979. /rb-87/-/sr-87/ chronology of h chondrites - constraint and speculations on the early evolution of their parent body. Earth and Planetary Science Letters 42, 333–347.

Mitchner, B. M., C. H. Kruger, J., 1973. Partially Ionized Gases. Wiley, New York.

Morfill, G. E., 1983. Some cosmochemical consequences of a turbulent protoplanetary cloud. Icarus 53, 41–54.

Morfill, G. E., Spruit, H., Levy, E. H., 1993. Physical processes and conditions associated with the formation of protoplanetary disks. In: Levy, E. H., Lunine, J. I. (Eds.), Protostars and Planets III. pp. 939–978.

Moriarty-Schieven, G. H., Snell, R. L., Strom, S. E., Schloerb, F. P., Strom, K. M., Grasdalen, G. L., Aug. 1987. High-resolution images of the l1551 bipolar outflow - evidence for an expanding, accelerated shell. The Astrophysical Journal 319, 742–753.

NASA, Watson, A., 1995. The dynamic hh30 disk and jet.

Otto, A., Dec. 1991. Three-dimensional magnetohydrodynamic simulations of processes at the earth's magnetopause. Geophysical and Astrophysical Fluid Dynamics 62, 69–82.

Otto, A., Mar. 2001. Geospace environment modeling (gem) magnetic reconnection challenge: Mhd and hall mhd-constant and current dependent resistivity models. Journal of Geophysical Research 106, 3751–3758.

Parker, E. N., Dec. 1957. Sweet's mechanism for merging magnetic fields in conducting fluids. Journal of Geophysical Research 62, 509–520.

Parker, E. N., Jul. 1963. The solar-flare phenomenon and the theory of reconnection and annihiliation of magnetic fields. The Astrophysical Journal 8, 177–+.

Pauli, W., 1973. Statistical Mechanics. Dover, New York.

Petschek, H. E., 1964. Magnetic field annihilation. In: Hess, W. N. (Ed.), The Physics of Solar Flares. pp. 425–+.

Pety, J., Gueth, F., Guilloteau, S., Dutrey, A., Nov. 2006. Plateau de bure interferometer observations of the disk and outflow of hh 30. Astronomy and Astrophysics 458, 841–854.

Press, W. H., Teukolsky, S. A., Vetterling, W. T., Flannery, B. P., 2002. Numerical Recipes in C: The Art of Scientific Computing. Cambridge University Press, New York, NY.

Priest, E. R., Forbes, T., 2000. Magnetic Reconnection: MHD theory and applications. Cambridge University Press, New York, NY.

Roache, P. J., 1985. Computational Fluid Dyanmics. Hermosa Publishers, Albuquerque, NM.

Roussel-Dupré, R., Colman, J. J., Symbalisty, E., Sentman, D., Pasko, V. P., Jun. 2008. Physical processes related to discharges in planetary atmospheres. Space Science Reviews, 93–+.

Rubin, A. E., Sep. 1984. Coarse-grained chondrule rims in type 3 chondrites. Geochimica et Cosmochimica Acta 48, 1779–1789.

Safier, P. N., May 1993. Centrifugally driven winds from protostellar disks. i - wind model and thermal structure. The Astrophysical Journal 408, 115–159.

Scholer, M., Otto, A., Apr. 1991. Magnetotail reconnection - current diversion and field-aligned currents. Geophysical Research Letters 18, 733–736.

Schrödinger, E., 1989. Statistical Thermodynamics. Dover, New York.

Schröer, A., Birk, G. T., Kopp, A., 1998. Denisis - a three-dimensional partially ionized dusty magnetoplasma code. Computer Physics Communications 112, 7–22.

Scott, E. R., Taylor, G. J., Nov. 1983. Chondrules and other components in c, o, and e chondrites similarities in their properties and origins. In: Boynton, W. V., Schubert, G. (Eds.), Proc. of the 14th Lunar and Planetary Sci. Conf. Vol. 14 of Lunar and Planetary Science Conference. pp. B275–B286.

Sears, D. W., 2004. The Origin of Chondrules and Chondrites. Cambridge Planetary Science, Cambridge.

Sears, D. W., Dodd, R. T., 1988. Overview and classification of meteorites. Meteorites and the Early Solar System.

Sears, D. W., Jie, L., Benoit, P. H., Dehar, J. M., Lofgren, G. E., May 1992. A compositional classification scheme for meteoritic chondrules. Nature 357, 207–210.

Shukla, P. K., Mamun, A. A., 2002. Introduction to Dusty Plasma Physics. Institute of Physics Publishing, Bristol.

Shukla, P. K., Mendis, D. A., Desai, T. (Eds.), 1997. Advances in dusty plasmas.

Skinner, W. R., 1990. Bipolar outflows and a new model of the early solar system. part ii: The origins of chondrules, isotopic anomalies, and chemical fractionations. Abstracts of the Lunar and Planetary Science Conference 21, 1168–1169.

Sonnet, C. P., Aug. 1979. On the origin of chondrules. Geophysical Research Letters 6, 677–680.

Suguira, N., Lanoix, M., Strangway, D. W., 1979. Magnetic fields of the solar nebula as recorded in chondrules from the allende meteorite. Phys. of the Earth and Planetary Interiors 20, 342–349.

Sweet, P. A., 1958a. The neutral point theory of solar flares. In: Lehnert, B. (Ed.), Electromagnetic Phenomena in Cosmical Physics. Vol. 6 of IAU Symposium. pp. 123–+.

Sweet, P. A., 1958b. The production of high energy particles in solar flares. Nuovo Cimento 8, 188–196.

Taylor, G. J., Scott, E. R., Keil, K., 1983. Cosmic setting for chondrule formation. Chondrules and their Origins, 262–278.

Terasawa, T., 1983. Hall current effect on tearing mode instability. Geophysical Research Letters 10 (6), 475–478.

Truitt, R. W., 1960. Fundamentals of Aerodynamic Heating. The Ronald Press Co., New York.

Turner, G., Feb. 1981. Argon-argon age measurements and calculations of temperatures resulting from asteroidal break-up. Royal Society of London Proceedings Series A 374, 281–298.

Unruh, D. M., Tatsumoto, D. M., 1980. A uniform u-pb age for l chondrites and a method for correcting for terrestrial pb contamination. LPI Contributions 412.

Urey, H. C., Nov. 1956. Diamonds, meteorites, and the origin of the solar system. The Astrophysical Journal 124, 623–+.

Verheest, F., 2001. Waves in Dusty Space Plasmas. Springer.

von Tschermak, G., 1964. The microscopic properties of meteorites. Washington, Smithsonian Institution: U. S. Govt. Print. Off.] 1964.

Wasson, J. T., 1974. Meteorites: Classification and Properties. Springer-Verlag, New York.

Wasson, J. T., Mar. 1993. Constraints on chondrule origins. Meteoritics 28, 14–28.

Whipple, F. L., Jul. 1966. Chondrules: Suggestion concerning the origin. Science 153, 54–56.

Wiechen, H. M., Birk, G. T., Kopp, A., Lesch, H., 2002. Self-magnetization of protoplanetary accretion disk matter. Physics of Plasmas 9 (10), 4285–4292.

Williams, J. D., Thomas, E., 2006. Initial measurement of the kinetic dust temperature of a weakly coupled dusty plasma. Physics of Plasmas 13 (6), 063509–063509–6.

Williams, J. D., Thomas, E., 2007. Measurement of the kinetic dust temperature of a weakly coupled dusty plasma. Physics of Plasmas 14 (6), 063702–063702–8.

Wood, J. A., Jul. 1962. Metamorphism in chondrites. gca 26, 739–742.

Wood, J. A., 1984. On the formation of meteoritic chondrules by aerodynamic drag heating in the solar nebula. Earth and Planetary Science Letters 70, 11–26.